Giant magnetoresistance of magnetic multilayers

Giant Magnetoresistance of Magnetic Multilayers

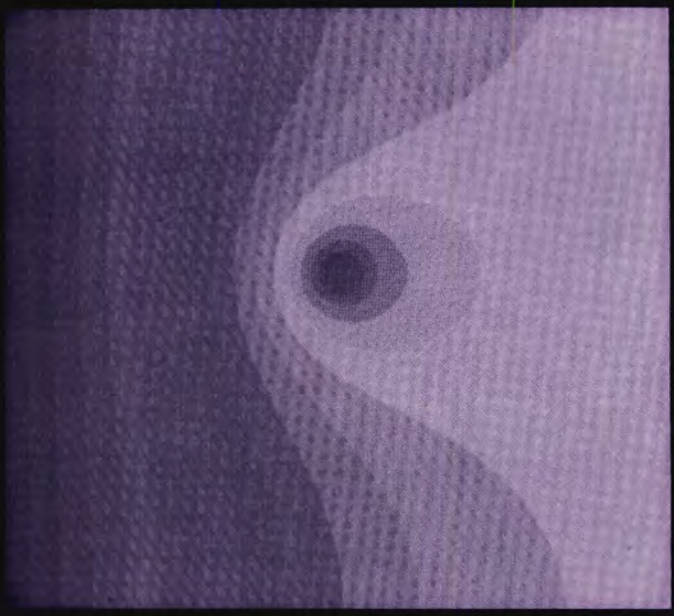

S. K. J. Lenczowski

Cover: Distribution of equipotential lines in the bottom electrode of a pillar structure used to measure the perpendicular giant magnetoresistance effect.

Giant Magnetoresistance of Magnetic Multilayers

S. K. J. Lenczowski

Giant Magnetoresistance of Magnetic Multilayers

PROEFSCHRIFT

ter verkrijging van de graad van doctor aan de Technische Universiteit Eindhoven, op gezag van de Rector Magnificus, prof. dr. J. H. van Lint, voor een commissie aangewezen door het College van Dekanen in het openbaar te verdedigen op dinsdag 26 september 1995 om 14.00 uur

door

Stanisław Karel Józef Lenczowski

geboren te Schiedam

Dit proefschrift is goedgekeurd door de promotoren

prof. dr. ir. W. J. M. de Jonge
en
prof. dr. H. van Houten.

Copromotor: dr. M. A. M. Gijs.

CIP-GEGEVENS KONINKLIJKE BIBLIOTHEEK, DEN HAAG

Lenczowski, Stanisław Karel Józef

Giant magnetoresistance of magnetic multilayers /
Stanisław Karel Józef Lenczowski. - Eindhoven :
Eindhoven University of Technology
Thesis Technische Universiteit Eindhoven. -
With bibliogr., ref. - With summary in Dutch.
ISBN 90-386-0426-2
Subject headings: magnetoresistance / multilayers /
microfabrication.

The work described in this thesis has been performed in the framework of a cooperative research program of the Solid State Division (group Cooperative Phenomena) of the Physics Department at the Eindhoven University of Technology and the group Experimental and Theoretical Physics at Philips Research Laboratories, both situated in Eindhoven, The Netherlands. Most of the research has been carried out at Philips Research Laboratories. Part of the research has also been supported by the European Community Science Project ESPRIT3: Basic Research, "Study of Magnetic Multilayers for Magnetoresistive Sensors".

Contents

Chapter 1

Introduction

When the so-called giant magnetoresistance effect was discovered back in 1988 at the Université Paris-Sud [1], it meant the beginning of an enormous amount of scientific research. The electrical resistivity of an antiferromagnetically coupled Fe/Cr superlattice was found to decrease by a factor of two when exposed to a large enough magnetic field. Such a large magnetoresistance effect in magnetic multilayers had never been observed before and could certainly not be explained by any known mechanism at that moment. However, the effect was not only very interesting from an academic point of view, also the application potential for magnetic sensors and recording was soon acknowledged. Due to the push in research by both universities and industrial laboratories, our understanding of the giant magnetoresistance effect and related phenomena such as, for instance, the magnetic interlayer coupling of magnetic layers over nonmagnetic spacers, has greatly increased. This was made possible by the simultaneous development of advanced preparation and measuring methods, since these new phenomena can only be observed when the individual layer thicknesses in the multilayer are in the order of a few nanometers. This means that one has to be able to control the structure of the layers themselves, as well as of the interfaces between them, at almost an atomic level.

The giant magnetoresistance effect was first observed in antiferromagnetically (AF) coupled magnetic multilayers. The magnetization vectors of the magnetic layers in such an AF-coupled sample can be oriented parallel under the influence of a sufficiently large magnetic field. As will be seen later, this switching from an antiparallel to a parallel alignment is one of the basic ingredients in order to observe the giant magnetoresistance effect. Nowadays, various structures can be engineered to achieve a magnetic-field driven transition between a parallel and an antiparallel state. In prototypical spin-valve devices for low-field sensors, for instance, the so-called exchange biasing effect is used [2], but also several other methods have already been proposed in the literature [3–10].

The origin of the giant magnetoresistance effect in practical structures is now basically understood in terms of spin-dependent scattering of the conduction electrons. Back in the seventies, the phenomenon of spin-dependent conduction was extensively studied in ferromagnetic alloys [11]. For the ferromagnetic $3d$ transition metals the d band is shifted in energy, so that it becomes asymmetric for

spin-up and spin-down electrons. This essentially explains the magnetism observed in those materials. Moreover, it also causes the density of states at the Fermi level to be different for both spin directions. As a consequence, the resistivities of conduction electrons with opposite spin orientation can be different. By introducing an effective spin-asymmetry parameter, α, representing the ratio of spin-down over spin-up resistivity, a fairly good description of the conductance behavior of those diluted ferromagnets could be obtained.

Applying the model of two differently conducting spin channels to the case of a magnetically ordered superlattice, one can understand the giant magnetoresistance effect in the following way. When the magnetizations of the magnetic layers are aligned antiparallel, conduction electrons in both spin channels will be alternately spin-up and spin-down electrons. Consequently, the total resistance of each spin channel will be equal. In the parallel situation, however, electrons of one channel, say spin-up, always have a low resistivity, while those with opposite spin direction exhibit a high resistance in each layer. When the spin-asymmetry parameter is large, the low-resistive channel dominates and lowers the resistance substantially.

The spin-dependent scattering processes in magnetic multilayers can, in principle, occur both within the bulk of the magnetic layers as well as at the interfaces between the layers. The question which of the two scattering sources contributes the most to the giant magnetoresistance effect has been the issue of debate. From many recent studies in the literature and part of this thesis, however, one must conclude that the spin-dependence of the interface scattering is the main cause for the large magnetoresistance values observed in magnetic multilayers. This conclusion may partly explain the large variety in experimentally measured magnetoresistance values for nominally identical samples grown under different conditions. The spin-asymmetry parameter for the scattering processes at interfaces may depend strongly on its precise structure, inherently being different for various deposition methods.

Most experiments on the giant magnetoresistance effect so far, have been performed with the current flowing along the planes of the multilayer, commonly called the current-in-plane (CIP) geometry. In the CIP geometry it is expected that the giant magnetoresistance effect will vanish when the individual layer thicknesses become much larger that the mean free path, λ, of the conduction electrons. This is not necessarily the case, however, in the current-perpendicular-to-plane (CPP) geometry, where the current is directed perpendicularly through the layer planes. In the CPP geometry a new phenomenon of spin accumulation at the interfaces occurs. This spin accumulation is balanced by spin-flip diffusion processes, for which the spin-flip diffusion length, l_{sf}, is the relevant length scale. If l_{sf} is much larger than the mean free path of the electrons, it turns out that l_{sf} becomes the only relevant length scale in the CPP geometry [12]. This situation indeed applies to the case of several real multilayer systems, where l_{sf} may exceed λ by more than an order of magnitude, especially at low temperature. This

implies that the giant magnetoresistance effect in the CPP geometry persists up to larger individual layer thicknesses than in the CIP geometry.

From an application point of view, the CPP geometry is rather advantageous. All theories on the giant magnetoresistance effect developed thus far, predict a considerably higher magnetoresistance value for the CPP geometry than for the CIP geometry. Essentially, this can be attributed to a more effective exploitation of the multilayer structure, since the electrons have to cross *all* the interfaces of the sample. To prove the larger CPP magnetoresistance experimentally, however, appeared to be rather difficult. This is mainly due to the very low perpendicular resistance of the multilayer compared to the resistance of the contact leads. To overcome this problem, Pratt and coworkers [13] used crossed superconducting contact leads of Nb, which defines an effective "pillar" area in the order of 1 mm^2. The resistance, in the order of $10^{-7}\,\Omega$, was subsequently measured with a sensitive SQUID-based system. Their measurements, limited to low temperatures, indeed showed an enhanced CPP magnetoresistance effect compared to the CIP magnetoresistance. A second way to measure the CPP resistance is to decrease the pillar size in order to raise the resistance to a measurable range. This method needs rather advanced microfabrication techniques and a more complicated measuring structure, but it offers the possibility to study the temperature dependence of the CPP magnetoresistance.

Both the CIP and CPP magnetoresistance decrease as one raises the temperature. The reason for this is twofold. On the one hand, an effective mixing of the two spin-currents is induced by thermally activated electron-magnon scattering. On the other hand, the relevant length scales shorten, λ for the CIP and l_{sf} for the CPP geometry as discussed above. To get a better insight in these effects, studies on the temperature dependence of the magnetoresistance are very desirable. Eventually, this may help to improve the magnetoresistance values at higher temperatures, which can be interesting for future applications, since a good performance at room temperature or even higher is required.

More recently, it was demonstrated that wires of ferromagnetic materials [14] or even multilayers [15, 16] with an extremely large height-to-width ratio could be obtained by means of electrodeposition in nanopores of about 100 nm width. These pores were made by nuclear track etching in approximately 4 μm thick membranes. If one can make good electrical contacts to those multilayer wires, CPP magnetoresistance measurements can be performed at any temperature without the complications mentioned above. So, as an alternative deposition method, electrodeposition of multilayers was also investigated in the present work, although up to now only CIP structures exhibiting a giant magnetoresistance effect have been realized. Electroplating CPP structures in nanopores in a controlled way with individual layer thicknesses sufficiently small to obtain AF coupling and hence large magnetoresistance values, still proves to be troublesome.

The organization of this thesis is as follows. In chapter 2 the experimental techniques which are most frequently used throughout this thesis will be in-

troduced. The chapter is divided into two parts. Firstly, deposition methods for the growth of magnetic multilayers are briefly mentioned, followed by a description of the microfabrication process to structure the multilayers into small pillars. Secondly, a few typical analysis techniques used to characterize the samples structurally, magnetically, and electrically are discussed. Chapter 3 deals with theoretical aspects concerning the giant magnetoresistance effect. We have focussed on those models which have been used to deduce important parameters, such as, for example, the spin-asymmetry parameter describing the spin dependence of the scattering processes. In chapter 4, CIP magnetoresistance experiments are presented. With these experiments we have tried to determine the spin dependence of both the scattering processes occurring at the interfaces and within the bulk of the magnetic layers. Furthermore, first magnetoresistance results of electrodeposited Co/Cu multilayers are described. The CPP magnetoresistance experiments are discussed in chapter 5. The first two sections of this chapter address the complications that arise when performing resistance measurements on small pillar-like structures, such as a spurious spreading resistance and nonuniform current-distribution effects. The last two sections of chapter 5 contain the CPP magnetoresistance results of Fe/Cr and, in a more elaborate study containing the temperature dependence, of Co/Cu multilayers.

Here, we have given a brief introduction on the giant magnetoresistance effect in magnetic multilayers. More specific introductions to several issues addressed in this thesis can be found at the beginning of each section. Most of the work presented in chapters 4 and 5 has been or will be published in the literature in essentially the same form. Therefore, some small parts may seem somewhat redundant, but it offers the possibility to read the separate sections rather independently of each other.

Chapter 2

Experimental

2.1 Sample Fabrication Techniques and Microstructuring

2.1.1 Sputter deposition

The sputter deposition process is performed in a high-vacuum chamber, where highly energetic particles hit a target material from which atoms are released from the surface and condense on a substrate into a thin film. In our case, the bombarding particles are inert Ar-ions to prevent chemical reactions at the surfaces of the target or substrate. The background pressure of the system prior to the actual deposition of the film (or multilayer) is usually in the order of 10^{-7} Torr. A typical operating Ar-pressure, which is held constant during a deposition run, is 5×10^{-3} Torr. With these values and typical growth rates of a few Å per second, the impurity level of, for instance, oxygen that is incorporated in actual grown films proved to be less than 1%. For a more detailed description of the sputtering process and the present equipment, the reader is referred to Ref. 17.

Before each deposition run the sputtering rates of the targets are determined independently. These rates depend on the applied power and the condition of the targets themselves. Therefore, single films of the target materials are grown and their thicknesses (typically about 500 Å) are measured by low-angle X-ray diffraction experiments. This procedure gives a thickness accuracy of better than 5%. This so-called satellite run is usually done at a slightly larger background pressure of $\approx 2 \times 10^{-6}$ Torr in order to be able to complete one run in one day.

One of the major advantages of sputter deposition is the fact that in principle almost every material can be grown, either by dc-sputtering (metals) or rf-sputtering (insulators). This is because the target material is released from the solid phase due to a mechanical bombardment instead of some sort of heating process, where the melting temperature of the materials to be deposited can cause practical problems. Another advantage is the flexibility of the system. Targets can be interchanged every day, since the vacuum required for operation can be achieved relatively fast. A disadvantage on the other hand, is an enhanced interdiffusion and surface roughness of the interfaces between subsequent layers when compared to other vapor deposition methods such as molecular beam epi-

taxy. This is due to an, in principle, unwanted bombardment of the substrate by reflected Ar atoms. This uncontrolled process of substrate bombardment makes it hard to obtain well reproducible results between different sputtering runs, which means that additional characterization must be carefully performed when comparing results.

2.1.2 Molecular beam epitaxy

The principle of molecular beam epitaxy (MBE) is that a target material is passed into the vapor phase after which it condenses on a substrate. The most important differences from the sputtering process described earlier, are that the target material is evaporated by a thermal process and the system is operated at ultra-high vacuum conditions (10^{-10}-10^{-11} Torr). Due to these special operating conditions real epitaxial growth can be realized, which means that the crystal axes of the substrate and those of the condensing film are intimately related. The term molecular in this sense is an inheritance from the early days of this technique, when in semiconductor technology at first GaAs molecules were evaporated.

In the MBE machine available at the Philips Research Laboratories (VG Semicon V80M) [17], the heating of the target material occurs by three different methods. One is the so-called Knudsen cell, in which a crucible containing the metal to be evaporated is heated up electrically. A second way of heating is provided by e-guns, where highly energetic electrons bombard the target. The third method in the present equipment is heating the target by passing a large current through it. The target material in this case consists of very thin wires (filaments). An alternative way is to wind the wire of the material to be deposited around a separate heating wire. Other important facilities in the deposition chamber are a reflection high-energy electron diffractometer (RHEED), which is used to monitor the growth and crystallinity of the multilayers, and several quartz crystal monitors to register the growth rates during deposition.

Due to the very small deposition rates, the sample production of the MBE machine is rather low. However, presently it is possible to grow wedge-shaped samples, in which the thickness of one or more layers can be gradually varied within one single sample by employing a moving shutter. With local probing techniques, such as the magneto-optical Kerr effect (MOKE) with a spot size of several microns in diameter [17, 18], the effect of thickness variations on the magnetic properties can then be studied in a single structure. Typical growth rates of 0.2 Å/s are used and wedge slopes are in the order of a few Å per mm. The wedge technique has proved to be extremely useful in revealing very subtle details in the thickness dependence of coupling, anisotropy, and magnetization. Up to now, unfortunately, it has not been possible to locally measure the electrical resistance of such wedge-shaped samples, but one still has the possibility to structure them afterwards into electrically measurable structures [19].

2.1.3 Electrodeposition

Electrodeposition is an alternative deposition method for the (ultra)high-vacuum based techniques mentioned in the preceding sections. The experimental setup is relatively simple and, consequently, the costs involved are less by orders of magnitude. This makes electrodeposition an attractive candidate for producing thin films and multilayers. Moreover, recent work showed that it is also possible to electrochemically grow small wires of magnetic materials [14], or even magnetic multilayers [15, 16] into nanopores in pre-etched membranes. This could provide an attractive route to the fabrication of structures for measuring the giant magnetoresistance effect in the perpendicular direction. Up to now, however, good quality multilayers with individual layer thicknesses in the order of 20 Å or less, exhibiting large magnetoresistance effects and antiferromagnetic coupling, could not be made in a reproducible way.

In section 4.1 we will extensively describe our first attempts to grow Co/Cu multilayers on Si substrates coated with either Au or Cu. The main idea is to use the so-called single bath method, where the aqueous electrolyte contains both Co^{2+} and Cu^{2+} ions. This prevents spurious contamination of the layers when transporting the sample through air between two separate baths. The ion concentration of the more noble metal Cu is much smaller than that of Co. At the equilibrium potential of the reaction $Co^{2+} + 2e^- \rightleftharpoons Co$ only Cu^{2+} is reduced and a Cu layer will be deposited. At more negative potentials, both Cu^{2+} and Co^{2+} are reduced, but the reduction rate of Co^{2+} is much greater than that of Cu^{2+} due to the large difference in concentration. So, at a relatively large negative potential, a Co layer can be deposited with only a small amount of Cu impurities. By switching the potential between these two values, one can grow a multilayer stacking of, in our case, Co/Cu. All this can be done in a simple teflon cell with the substrate serving as the cathode. For the anode we used a relatively large Pt plate. As a reference electrode a saturated calomel electrode was used, placed just above the substrate. To switch the potential and to keep track of the current passed through the cathode, we used a commercially available potentiostat. The exact experimental procedure is described in detail in section 4.1.2.

2.1.4 Microstructuring

To perform resistance measurements on thin films or multilayers with the current flowing perpendicularly to the film plane is not straightforward at all, as mentioned in the introduction. This is due to the very small perpendicular resistance relative to the sheet resistance of the contact leads. To raise the perpendicular film resistance up into a measurable range, very small pillars with lateral dimensions at most in the order of the film thickness must be fabricated. Here we will describe such a structuring process in MBE evaporated and high-vacuum sputtered Co/Cu multilayers. For convenience, the description of the process will be

divided into four parts: **a)** the actual definition of the pillars, **b)** separation of the various pillars into isolated structures, **c)** patterning of the contact leads to be able to perform a four-point resistance measurement, and **d)** the etching of optional trenches as an adjustment to geometry effects which disturb the eventual current flow in the pillar. This last point is extensively described in sections 5.1 and 5.2.

a. definition of the pillars

Figure 2.1(a) shows schematically the multilayer stacking as it leaves the MBE chamber or the sputter clock. The cap layer of Au, also evaporated in the same run together with the multilayer, serves as a protection for the actual multilayer and, even more important, will be part of the upper contact electrodes later on in the fabrication process. For the lithographic patterning of the multilayer we deposit next a Mo layer of $0.2\,\mu$m, an Al_2O_3 layer of $0.4\,\mu$m, and finally a Mo layer of $0.2\,\mu$m again. This last Mo layer is used to create a mask in the Al_2O_3 layer, which itself is employed to create the actual pillar. The bottom Mo layer is later to be used as an adhesion promoter.

To make the desired pillar structure in the upper Mo layer we used conventional lithography and wet etching. A photoresistive layer (HPR-204 photoresist) is spun onto the Mo layer and exposed to ultraviolet light through an appropriate mask. The photoresist is then developed in an alkaline solution. The free surface of the Mo is subsequently wet etched using nitric acid (HNO_3 dissolved in phosphoric acid H_3PO_4 to control the etching rate). Afterwards the still present photoresist is removed with acetone. The resulting structure at this stage is shown in Fig. 2.1(b). The Mo mask is now used to transform the structure into the Al_2O_3 layer using plasma etching in CHF_3/Ar, which is depicted in Fig. 2.1(c).

Now the Al_2O_3 mask can be employed to define the pillar in the multilayer by means of a HCl plasma. To stop this etching process at the right time, i.e. when one has reached the Cu bottom electrode, appeared to be one of the most critical steps in the entire structuring process, since the etching rate of Cu is much larger than that of the multilayer material. To tackle this problem we used reference samples, grown simultaneously with the real multilayer on SiO_2 substrates without the Cu bottom electrode. This reference sample is placed under a laser beam and the reflected intensity is monitored during the plasma etching. When the multilayer stacking is etched through, the intensity of the reflected laser beam changes due to the different reflectivity of the SiO_2 substrate. Normally, we choose the number of repeats for the reference sample somewhat less. During the etching process, as the pillar is formed, reflected ions from the pillar edge cause the etching rate at those edges to increase with respect to the rest of the multilayer and the reference sample. The thinner reference sample serves as a compensation for this, preventing the Cu bottom electrode to be completely etched away down to the substrate at the position of the pillar edges. To complete

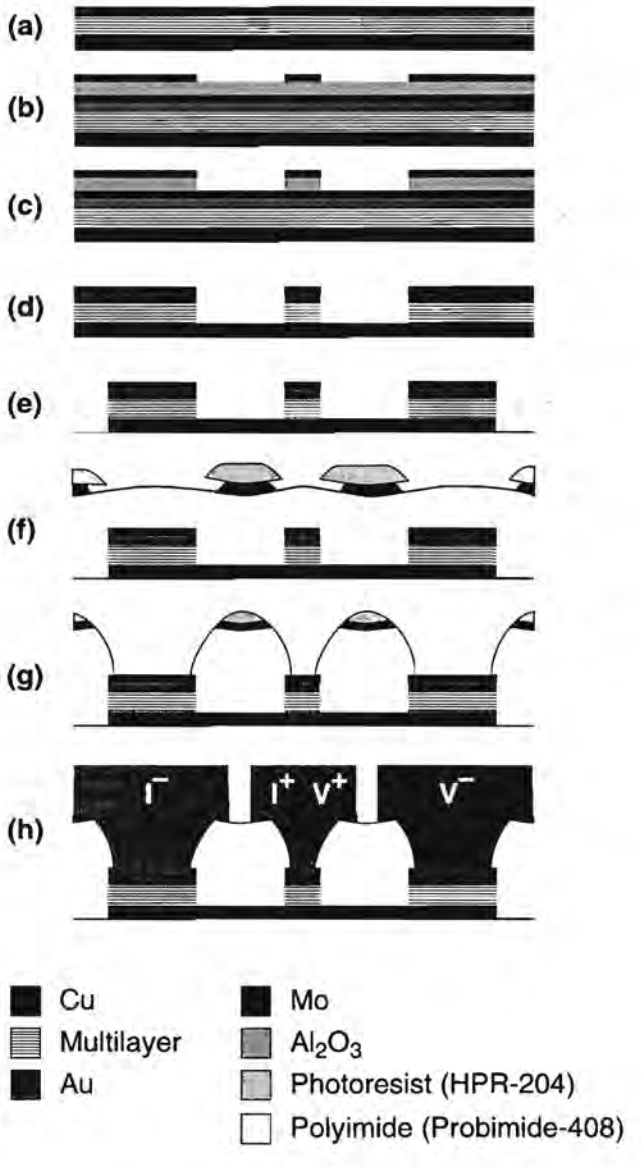

Figure 2.1. *The microstructuring process for Co/Cu multilayers at several stages. See text for a detailed explanation of the various subfigures. The pictures are schematic representations which means that, for clarity, the vertical dimensions have been blown up with respect to the horizontal ones.*

the part of creating the pillar structure in the multilayer, the remaining Al_2O_3 layer is removed with a CHF_3/Ar plasma. The resulting structure at this stage is schematically drawn in Fig. 2.1(d).

b. separating the various pillar structures

After the pillars themselves have been defined, we must separate the various structures on the total wafer (typically a few hundred) to be able to measure them independently. For this we spin again a photoresistive layer (HPR-204) on the sample which is developed in the usual way. The multilayer film is subsequently wet etched down to the substrate in a $FeCl_3$ solution, after which the remaining photoresistive layer is removed in acetone. This removing appeared to be a very tricky step indeed, since in many cases the total multilayer film was released from the substrate. This is probably due to internal stress that has been built up at this stage of the microstructuring process, caused by repeated heating and cooling of the sample. For those samples in which the various pillar structures were successfully separated, a schematic drawing is depicted in Fig. 2.1(e). The pillar in the center is the actual structure of which the resistance is to be measured. The outer two structures serve as parts of the contact leads which enables us to make electrical contact to the bottom part of the real pillar, which is described next. One remark can be made at this point. Although throughout this thesis we talk about "pillars", one should note that the height/width ratio of our smallest structures does not exceed 0.1.

c. creating the contact leads

On top of the structure as sketched in Fig. 2.1(e) we spin an insulating layer of polyimide (Probimide-408) with a thickness of 1.9 μm. The thin Mo layer now acts as an adhesion promoter as already indicated above. Another 0.2 μm Mo layer is deposited on the polyimide layer, in which holes are etched precisely above the three pillars using the standard technique with a HPR-204 photoresist. The Mo layer is slightly underetched causing the photoresistive layer to hang over to a certain extent. The slopes of the photoresist are smoothened out by an additional heat treatment prior to the etching of the Mo layer just after developing the photoresist. The resulting pattern is transferred into the polyimide by reactive ion etching in an O_2 plasma. This etching step is stopped on the Mo layer on top of the pillar structure [see Fig. 2.1(f)]. These flat slopes in the polyimide are extremely important, since they are crucial for a proper contact of the Au leads later to be deposited into the holes in the polyimide layer. Another point to note is that the photoresistive layer must be sufficiently thick, i.e. the Mo layer on top of the polyimide has to remain covered.

The next step is the removal of the Mo layer on top of the pillars, after which the still remaining photoresist is dissolved. Now the sample is mounted into a

high vacuum sputter machine in which a Au layer of 1.9 μm is deposited on top of the sample. Just before the Au sputtering the free Au surface is *in situ* cleaned by an Ar sputter etch to reduce the Au-Au contact resistance possibly caused by the inclusion of dust or etching residuals. The Mo layer on top of the polyimide acts as an adhesion promoter for the Au layer. The Au is structured in an I_2/KI solution with a mask of, again, the photoresist HPR-204 with a thin Mo adhesion layer. This photoresistive layer is then removed, after which the free Mo layers are dissolved. In principle, the structure schematically drawn in Fig. 2.1(g) is now ready to be measured.

d. optional trenches

In sections 5.1 and 5.2 we discuss in more detail some of the problems that occur when measuring the perpendicular resistance of the multilayer pillars with the geometry as obtained with the microstructuring process described above. One of those complications is the spreading of the current into the contact leads. This practically radial spreading in top and bottom electrodes in the direction of the voltage probes causes an additional voltage drop that can easily be in the order of the perpendicular voltage drop over the pillar. The effect is most pronounced in relatively highly resistive contact electrodes such as Cr in the case of Fe/Cr multilayers, but is in principle also present in the Co/Cu multilayers described here.

To eliminate the spreading of the current into the voltage leads, a trench can be made through the total sample down to the substrate, which physically separates the current and voltage probes. This is shown in Fig. 2.1(h). The trench was etched with a Nd:YAG laser (532 nm). A critical point in this step is that one has to stop before the actual pillar is reached. Therefore, the trench does never extend to the edge of the pillar, but is effective enough to reduce the spurious spreading resistance to an acceptable level as will be discussed in section 5.1.

In one structuring process, i.e. at one wafer, typically a few hundred samples are produced with various pillar diameters ranging from about 2 μm to 10 μm. When the pillars are ready to be measured, the substrate is cleaved into pieces containing four structures which are mounted onto IC-holders and subsequently wire bonded. For this we used thin Au or Al wires which are ultrasonically bonded to the contact leads. Here we have described the microfabrication process of Co/Cu multilayers. In the case of Fe/Cr multilayers deposited on SiO_2 substrates, the microstructuring process, except for some specific differences in the various etching rates, is in essence identical.

2.2 Analysis Techniques

2.2.1 X-ray diffraction

X-ray diffraction (XRD) is a standard technique to obtain structural information about a sample. An advantage of this technique is that it is a nondestructive method. It is based on the interference of X-rays which are reflected at periodic structures present in the sample. These periodic structures in multilayers can be the multilayer period, D_{ML}, and also the distances between various lattice planes in the different materials. Normally one uses the so-called θ-2θ-mode, in which the X-rays are directed towards the sample surface at an angle θ with respect to the film plane. The intensity of the reflected beam is then measured by a detector positioned at an angle 2θ. The X-ray source, in all diffraction experiments presented in this thesis a Cu-$K\alpha$ tube with a wavelength $\lambda = 1.5419\,\text{Å}$ (Philips PW 1710), is fixed in space.

The position of the maxima in the intensity of the detected diffraction profile is determined by Bragg's law, which states that $2\,d\,\sin(\theta_n) = n\,\lambda$ with d a single period along the film normal and n an integer. The width of these peaks is inversely proportional to the perpendicular coherence length, which is the length over which the periodicity is maintained. For a perfectly grown multilayer this would mean the total film thickness, but in practice it is only a few hundred Å corresponding to less than ten multilayer periods (individual layer thicknesses are often 10 Å or larger). Segmüller and Blakeslee [20] calculated the resulting diffraction pattern in the case of a multilayer consisting of two materials A and B with individual atomic lattice-plane distances d_{A} and d_{B}, respectively, corresponding to n_{A} and n_{B} atomic planes per multilayer period. Using a kinematical model they found that there are, in principle, two sets of peaks centered around the positions at which the Bragg maxima would have occurred in case of single films of material A or B. The angular extent of these sets of peaks is determined by d_{A} and d_{B}, respectively. Again, the width of the peaks is a measure of the perpendicular coherence length. When the multilayer period is short or $d_{\mathrm{A}} \approx d_{\mathrm{B}}$ the two sets merge into one for which the relation $2\,D_{\mathrm{ML}}\,\sin(\theta_k) = k\,\lambda$ holds with $k = (n_{\mathrm{A}} + n_{\mathrm{B}}) \pm l$ and l an integer. So, in this situation, the central peak ($l = 0$) is at the position of a first order reflection at some kind of a fictive mean lattice with a perpendicular atomic plane distance approximately equal to $\frac{1}{2}(d_{\mathrm{A}} + d_{\mathrm{B}})$.

As an example, a typical XRD scan of a 55×[Co(1.5 nm)+Cu(4.5 nm)] multilayer is depicted in Fig. 2.2(a). The multilayer period can now be calculated from a least-square fit of the positions of the intensity maxima to the relation $2\,D_{\mathrm{ML}}\,\sin(\theta_k) = k\,\lambda$. The position of the main peak at about, in this case, 50.85° gives important information about the texture of the multilayer. For a fcc (100)-oriented Co/Cu multilayer, as is the case here, the position of the central point of the set of satellite peaks is indeed expected to be at $2\theta \approx 51°$, whereas for the fcc (111) crystallographic orientation, for instance, this would be at $2\theta \approx 43°$. In

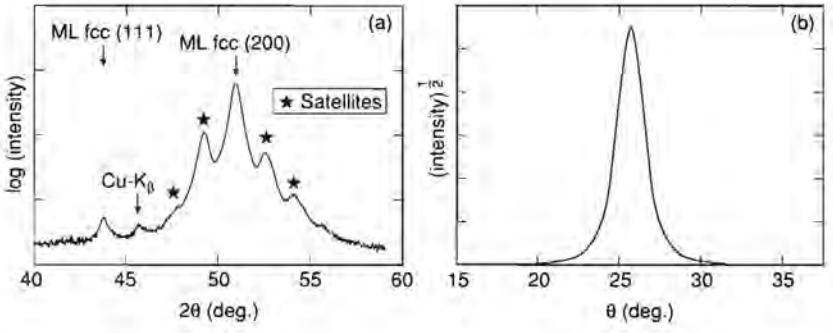

Figure 2.2. *Typical X-ray diffraction measurements of a Co/Cu multilayer consisting of 55 repeats of [Co(1.5 nm)+Cu(4.5 nm)]. (a) "Normal" θ-2θ scan. (b) Rocking curve about the main (200) peak at $2\theta \approx 50.85°$.*

practice, most multilayers grown are polycrystalline and the texture of the crystallites displays a spread around a mean orientation, which is usually the film normal. This spread in texture with respect to the film normal can be measured in a so-called rocking curve. In such a diffraction measurement the sample and detector are first placed into a position where the Bragg relation holds according to a "normal" θ-2θ scan. Then the sample is rotated keeping the angle of the detector fixed at 2θ. Slightly disoriented crystallites are now placed into positions where they satisfy the Bragg relation. So, the width of such a rocking curve gives information on the angular distribution of the crystallite orientations and serves in that sense as another useful quality criterion. Figure 2.2(b) shows the rocking curve about the main (200) peak of the multilayer of Fig. 2.2(a).

2.2.2 Magnetization measurements

To characterize samples magnetically, magnetization measurements have been performed using a vibrating sample magnetometer (VSM) or a superconducting quantum interference device (SQUID). With both techniques it is possible to record a so-called M-H-loop (or hysteresis loop). From these loops information on magnetic properties such as the saturation magnetization, M_s, the remanence, M_r, and the coercive field, H_c, can be obtained as well as on the magnetic anisotropy and coupling strengths between magnetic layers or planes. All these quantities are characteristic for a specific sample and are related to its precise structure.

The principle of the VSM is that a vibrating magnetic sample causes an

induced current in detection coils placed around the sample. In our setup, an electromagnet supplies a static magnetic field up to a maximum value of about $\mu_0 H = 1.6\,\mathrm{T}$. The sample is attached to a long rod which extends well below the sample as to minimize the contribution from the sample holder to the magnetic signal. The sample holder is brought into vibration by the conus of a loudspeaker operating at 80 Hz and with a constant amplitude. The apparatus is specially designed to measure two orthogonal components of the magnetization vector in one single run; mostly, the detection coils are positioned in such a way that the component of the magnetization along the magnetic field and the one along the direction of the sample holder can be detected. With the present equipment, magnetic moments as small as about $\frac{1}{2}\,\mu\mathrm{A\,m^2}$ can be measured, which corresponds to approximately 50 Å of Co on a commonly used $4 \times 12\,\mathrm{mm^2}$ sample area. A SQUID commonly exceeds this sensitivity by four orders of magnitude, but for our purpose we usually do not need these high sensitivities. For a very general description of the VSM we can refer to the work of Foner [21], whereas our specific VSM is discussed in more detail by Bernards and Schrauwen [22].

2.2.3 Magnetoresistance measurements

Most of the resistance measurements described in this thesis are performed using a four-point ac resistance bridge (LR-400) operating at a low frequency of 13 Hz. With this system, resistances ranging from 100 mΩ to 200 kΩ within an accuracy of about 0.1% can be measured. For an adequate measurement of the resistivity of the sample, the specific positions of the contact electrodes have to be carefully examined as well as the precise shape of the sample. Throughout this thesis complications associated with this are referred to as current-distribution effects (see, for instance, sections 5.1 and 5.2 for a detailed discussion of our CPP pillar geometry). An elegant way of measuring the resistivity, ρ, of a thin film (or, actually, the sheet resistance, $R^{\square} \equiv \rho/d$, where d denotes the thickness of the sample) is by means of the so-called Van der Pauw geometry [23]. In this geometry the four contact electrodes are placed on the four corners of a sample of arbitrary shape (see Fig. 2.3) and both the resistances $R_{12,34}$ and $R_{13,24}$ are measured. $R_{12,34}$ is defined as the voltage drop between the contacts three and four when a unit current is flowing from contact one to contact two. $R_{13,24}$ has an analogous definition. Van der Pauw showed that the sheet resistance of the sample is now given by

$$R^{\square} \equiv \rho/d = \frac{\pi}{\ln(2)} \, \frac{R_{12,34} + R_{13,24}}{2} \, f, \tag{2.1}$$

with f satisfying the relation

$$\frac{R_{12,34} - R_{13,24}}{R_{12,34} + R_{13,24}} = \frac{f}{\ln(2)} \, \cosh^{-1}\left[\frac{\exp(\ln 2/f)}{2}\right]. \tag{2.2}$$

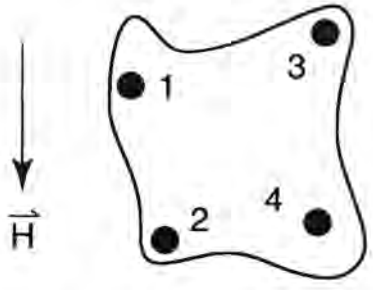

Figure 2.3. *Van der Pauw geometry.*

The resistivity obtained this way is an average in case the resistivity in the plane of the film is not isotropic. This can be the case, for instance, when a magnetic sample exhibiting an anisotropic magnetoresistance effect is exposed to a magnetic field. The anisotropic magnetoresistance effect means that the resistivity depends on the angle between the current and the magnetization of the sample. When the magnetic field direction is fixed, say, along the sample edge from contact 1 to contact 2, the (field dependent) in-plane resistivity becomes anisotropic. This measuring geometry can then still be used to determine the anisotropic magnetoresistance (MR) *ratio*, roughly defined as $\Delta\rho/\rho_0$ where $\Delta\rho$ is the difference in resistivity at magnetic fields sufficiently large to saturate the magnetic sample and the resistivity at zero magnetic field, ρ_0. Even more, one can discriminate between the anisotropic magnetoresistance and the giant magnetoresistance ratio, since the latter does not depend on the relative orientation of the current and the magnetic field. When in this thesis the Van der Pauw geometry is employed, we use the average $\frac{1}{2}\left(\mathrm{MR}_{12,34} + \mathrm{MR}_{13,24}\right)$ as a measure for the giant magnetoresistance ratio.

In our experimental setup we can measure the resistance from liquid helium temperature to about 350 K in magnetic fields up to $\mu_0 H \approx 2.2\,\mathrm{T}$. The sample holder can be rotated, which makes it possible to perform measurements with the magnetic field along the plane of the film and perpendicular to the film plane (or any angle in between).

Chapter 3

Theory of Magnetoresistance

This chapter presents the most important ingredients for understanding the giant magnetoresistance effect in magnetic multilayers. We do not aim to give a full and complete survey of all theories that have been proposed in the literature. Extensive reviews on most of the theoretical aspects concerning the giant magnetoresistance effect can be found elsewhere [24, 25]. Instead, we choose to follow mainly one approach as a guideline to explain the effect and to highlight some of the differences between the current-in-plane (CIP) and the current-perpendicular-to-plane (CPP) geometry. This approach is based on the Boltzmann equation for conduction and is perhaps the most transparent description. At the end of this chapter, we summarize two other models, based on the Kubo and Landauer-Büttiker formalisms, as far as they are useful to describe the experimental results of chapters 4 and 5.

3.1 The Boltzmann Approach in the Current-In-Plane Geometry

As a way of introduction, we will start off with a brief description of the principles of electronic conduction in thin films within the semi-classical picture originally developed by Fuchs [26] and later worked out by Sondheimer [27]. This theory, which is based on the Boltzmann transport equation, already gives a fairly good insight in the most important features of the thickness dependence of the resistivity of thin films. Moreover, it can rather easily be generalized to our case of interest, i.e. thin magnetic multilayers. This was first proposed by Camley and Barnaś [28, 29] back in 1989, and later worked out further by numerous authors with specific improvements and extensions [30–35]. All these models are built on Fuchs-Sondheimer type of equations, which are taken to be spin dependent to be able to explain the giant magnetoresistance effect. The differences are basically the various boundary conditions that are assumed at the outer edges of the total multilayer sample or at the interfaces between the constituent layers. At the present time, many multilayer systems exhibiting the giant magnetoresistance effect have been parametrized within the framework of these theories and a good phenomenological description of the CIP magnetoresistance data has been obtained.

Consider the case of free electrons. When a constant electric field, $\boldsymbol{E}$, is applied, the Fermi sphere will be displaced in $\boldsymbol{k}$-space at a constant rate in the direction of the electric field. This only holds as long as scattering of the conduction electrons is absent. Introducing scattering phenomenologically by a relaxation time, τ, the displacement of the Fermi sphere in the steady state is given by $\Delta\boldsymbol{k} = e\,\boldsymbol{E}\,\tau/\hbar$ with e the charge of an electron. The electrical current density for a system with n electrons per unit volume is then proportional to this displacement according to

$$\boldsymbol{j} = \frac{n\,e\,\hbar\,\Delta\boldsymbol{k}}{m} = \frac{n\,e^2\,\tau}{m}\,\boldsymbol{E} = \sigma\,\boldsymbol{E}, \tag{3.1}$$

where σ is the electrical conductivity. Equation (3.1) is just Ohm's law for conduction.

A more microscopical theory of the conduction in metals is based on the Boltzmann transport equation. Here, a classical distribution function for the electron gas, $f(\boldsymbol{r},\boldsymbol{v})$, is defined depending on the particle's position in space, $\boldsymbol{r}$, and its velocity, $\boldsymbol{v}$. The Boltzmann transport equation is now derived from the argument that the distribution is conserved if we follow a volume element, $(d\boldsymbol{r}d\boldsymbol{v})$, along a flow line. Thus, in the presence of scattering, we obtain:

$$\frac{\mathrm{d}f}{\mathrm{d}t} = \left(\frac{\mathrm{d}f}{\mathrm{d}t}\right)_{\boldsymbol{E}} - \left(\frac{\mathrm{d}f}{\mathrm{d}t}\right)_{\mathrm{scat}} = 0. \tag{3.2}$$

In the steady state $\partial f/\partial t = 0$ by definition and the Boltzmann transport equation reads:

$$\boldsymbol{v}\cdot\nabla_{\boldsymbol{r}}\,f + \boldsymbol{a}\cdot\nabla_{\boldsymbol{v}}\,f = \left(\frac{\mathrm{d}f}{\mathrm{d}t}\right)_{\mathrm{scat}}, \tag{3.3}$$

where $\boldsymbol{a} = \partial\boldsymbol{v}/\partial t$. A very useful approximation, which is often made in the literature for the term on the right-hand side of Eq. (3.3), is the so-called relaxation time approximation. It says that $(\mathrm{d}f/\mathrm{d}t)_{\mathrm{scat}}$ is proportional to the deviation of the distribution function from equilibrium, with the constant of proportionality one over the relaxation time τ:

$$\left(\frac{\mathrm{d}f}{\mathrm{d}t}\right)_{\mathrm{scat}} = -\frac{(f - f^0)}{\tau} \equiv -\frac{g}{\tau}. \tag{3.4}$$

Here f^0 denotes the Fermi-Dirac distribution function at thermal equilibrium,

$$f^0 = \frac{1}{\exp\left(\frac{\epsilon-\epsilon_F}{k_B T}\right) + 1}, \tag{3.5}$$

with $\epsilon = \frac{1}{2}\,m\,v^2$ for a parabolic band with effective mass m, and $g \ll f^0$. Suppose we apply an electric field in the x-direction to a semi-infinite sample with only

its dimension in the z-direction limited. In that case, combining Eqs. (3.3) and (3.4) yields

$$\frac{\partial g}{\partial z} + \frac{g}{v_z \tau} = \frac{e E}{m v_z} \frac{\partial f^0}{\partial v_x}. \tag{3.6}$$

Equation (3.6) states that the perturbation caused by the electric field is balanced by scattering processes and by diffusion, trying to make the distribution function uniform over the sample. For bulk samples $g \equiv g_\mathrm{b}$ is uniform, i.e. $\partial g_\mathrm{b}/\partial z = 0$, and we obtain as the solution to Eq. (3.6): $g_\mathrm{b} = (e E \tau/m)(\partial f^0/\partial v_x)$. This corresponds exactly to a displacement of the Fermi sphere in $\boldsymbol{k}$-space as we have already found in Eq. (3.1). For a thin film with a finite thickness, t, however, the situation changes considerably and the general solution to Eq. (3.6) becomes:

$$g(z, \boldsymbol{v}) = g_\mathrm{b}(\boldsymbol{v}) \left\{ 1 + A(\boldsymbol{v}) \exp(-\frac{z}{\tau v_z}) \right\}. \tag{3.7}$$

$A(\boldsymbol{v})$ denotes an integration constant which is determined by the boundary conditions of the specific problem. The current density can now be calculated according to $j = \sigma E \propto \int e v_x g(z, \boldsymbol{v}) \, \mathrm{d}^3 v \, \mathrm{d}z$. Following the Fuchs-Sondheimer approach, which assumes purely diffusive scattering at the outer edges of the thin film, i.e. the distribution function of electrons leaving the interface does not depend on the direction of $\boldsymbol{v}$, we find for the resistivity, $\rho = 1/\sigma$, of the thin film:

$$\rho = \frac{m v_F}{n e^2} \left(\frac{1}{\lambda} + \frac{3}{8 t} \right) \text{ for } \lambda \ll t, \tag{3.8a}$$

$$\rho = \frac{4 m v_F}{3 n e^2} \left(\frac{1}{t \{ \ln(\lambda/t) + 0.423 \}} \right) \text{ for } \lambda \gg t. \tag{3.8b}$$

Here, we have introduced the electron mean free path, $\lambda = v_F \tau$. Equation (3.8b) reveals one of the shortcomings of the classical Fuchs-Sondheimer description. In the limit $\lambda/t \to \infty$ the resistivity of a thin film with diffusive boundary scattering tends to zero due to a complete shunting of electrons with their velocity parallel to the plane of the film.

The above description of the resistivity of thin films can now easily be generalized to the case of metallic multilayers. Equation (3.6) needs to be solved for each layer separately and those solutions must be matched at the interfaces by appropriate boundary conditions. In the case of ferromagnetic layers, the scattering time τ (and thus the mean free path λ) is assumed to be spin dependent. Furthermore, also the transmission coefficients, T_σ, at the interfaces, phenomenologically representing interface scattering, are taken spin dependent. By evaluating the two extreme magnetic configurations of parallel and antiparallel alignment of the magnetization vectors of the magnetic layers, one can calculate the magnetoresistance ratio. This has been done numerically by many

groups in the literature with the spin-asymmetry parameters $\alpha_{\text{bulk}} = \lambda_\uparrow/\lambda_\downarrow$ and $\alpha_{\text{int}} = T_\uparrow/T_\downarrow$ as important fitting parameters. This method appeared to be a very powerful tool for describing many current-in-plane (CIP) magnetoresistance experiments. The general trends in the dependence of the magnetoresistance as a function of the (non)magnetic layer thickness and the number of repeats can be explained by this theory. An essential drawback of the theory, however, remains the different treatment of the bulk and interface contributions to the resistivity. As pointed out by Barthélémy and Fert [30], and Levy *et al.* [36, 37] this leads to an underestimate of the interfacial contribution to the resistivity and magnetoresistance. For instance, in the case of Fe/Cr superlattices, the semiclassical theory is unable to account for the large MR values in a quantitative way. These large MR values can only be explained by the theory when taking an unrealistic magnitude of the mean free path of the electrons, thereby deteriorating the fit of the thickness dependence of the magnetoresistance. In the magnetoresistance model of Levy, Zhang, and Fert [37, 38], however, which will be described in section 3 of this chapter, bulk and interface scattering are treated in the same way. Then, a better quantitative agreement with experiments can be obtained, from which the separate contributions of the spin-dependent bulk and interface scattering to the magnetoresistance can be deduced.

3.2 The Boltzmann Approach in the Current-Perpendicular-to-Plane Geometry

In this section we will discuss the effects of spin accumulation and spin relaxation at the boundaries between magnetic and nonmagnetic materials. This is an important fundamental issue, since it distinguishes clearly the current-in-plane (CIP) case from the current-perpendicular-to-plane (CPP) situation. Both the CIP and CPP magnetoresistance can be described by a two-current model in which spin-up and spin-down electrons have different conductivities as addressed in the previous section. The most important difference between the two geometries now arises from spin accumulation effects, playing only a role in the CPP case. In the CIP geometry these effects are not present, since no net electrical or spin current is passing through the various interfaces of the multilayer. We first give a relatively simple example of a single interface between two magnetic layers with their magnetizations pointing in opposite directions. Subsequently, the basic ideas will be extended to the case of magnetic multilayers consisting of magnetic layers separated by nonmagnetic spacer layers. Finally, expressions for limiting cases which are experimentally accessible will be formulated.

3.2.1 Spin accumulation and relaxation at interfaces

Figure 3.1 schematically shows the situation of an interface between two semi-infinite ferromagnetic materials with opposite magnetizations. We assume that the conductivity of the majority spin channel (spin-up electrons) is larger than that of the minority spin channel (spin-down electrons). In that case, far from the interface, the electrical current in ferromagnet L is carried mainly by the, say, spin(+) electrons (spin up in ferromagnet L), whereas in ferromagnet R the spin(−) electrons (spin up in ferromagnet R) contribute mostly to the current. So, for spin(+) electrons flowing from ferromagnet L to ferromagnet R the electron flux approaching the interface is actually larger than the electron flux going away from the interface. This results in an accumulation of spin(+) electrons around the interface and consequently a depletion of spin(−) electrons. Therefore, in the vicinity of the boundary between the two ferromagnets, a nonequilibrium spin polarization occurs and, in this example, a raise of the spin(+) chemical potential. The length to which the nonequilibrium polarization extends is determined by spin relaxation processes. Normally this spin diffusion length, l_{sf}, is much longer (≈ 1000 Å at low temperature) than the mean free path, λ, which implicates that the accumulation effects will be noticeable in the ferromagnets L and R, even relatively far from the interface. In Fig. 3.1(a) the position dependence of the excess chemical potential $\Delta\mu = (\mu_+ - \mu_-)/2$ for spin(+) electrons is plotted. $\Delta\mu$ varies exponentially with the typical decay length l_{sf}. The position dependence of the chemical potential can be regarded as an extra spin-dependent diffusion term to the gradient in the electrostatic potential, which drives the current flow. So, the electric field and consequently the current density are influenced over a typical distance l_{sf} away from the interface, which is visualized in Figs. 3.1(b) and 3.1(c), respectively.

Macroscopic equations for the spin accumulation effect at interfaces were first derived by Johnson and Silsbee [40] and Van Son *et al.* [41]. Later on, Johnson extended his treatment to the case of CPP magnetoresistance in multilayers [42] assuming the effects of the individual interfaces to be just additive. Valet and Fert [12, 39] calculated the problem of the CPP magnetoresistance in a microscopic model based on the Boltzmann equation, which will be summarized in the next paragraph. An important conclusion of the microscopic model is that the macroscopic equations for the single interface problem are valid in the limit where the spin diffusion length is much longer than the mean free path, in which case l_{sf} becomes the unique scaling length of the CPP magnetoresistance. However, the results of the calculations of Valet and Fert on multilayers differ quite strongly from those of Johnson [42], which finds its origin in the interplay of the spin accumulation at the various interfaces. In the limit of extremely long l_{sf} as compared to the individual layer thicknesses, the theoretical expressions become conveniently simple and relatively easy to comprehend. In fact, they can be understood in terms of a two-channel model with an additional spin-dependent

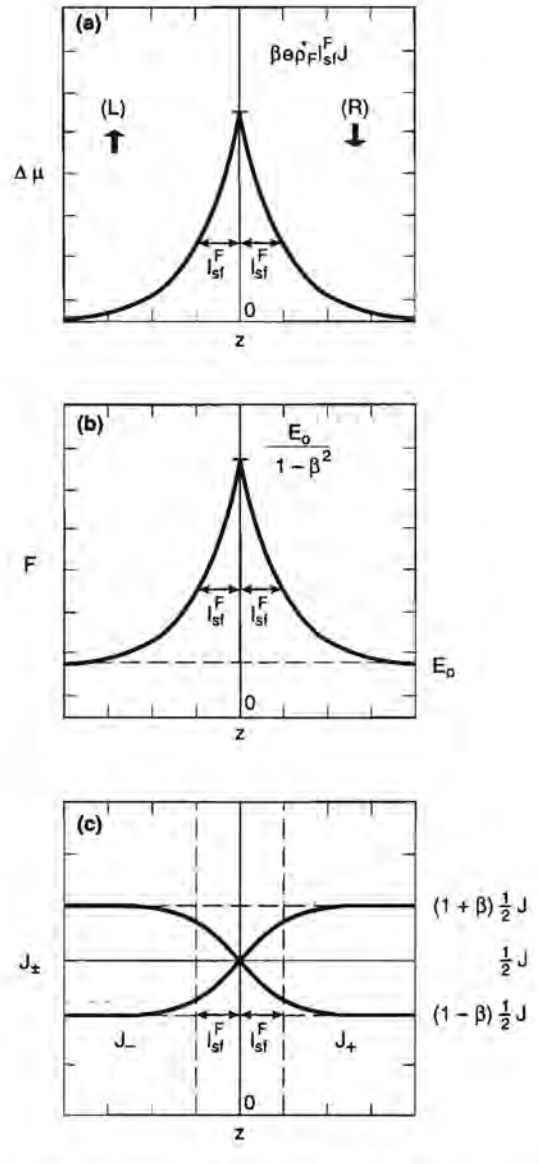

Figure 3.1. *(a) Chemical potential difference $\Delta\mu$, (b) electric field F, and (c) current densities J_+ and J_- as a function of the distance, z, to the interface between two semi-infinite ferromagnetic layers positioned at z=0. The arrows denote the magnetization directions of both layers. Data are from Valet and Fert in Refs. 12, 39.*

interface resistance as was already intuitively developed by Pratt and coworkers [43–46]. The fact of l_{sf} being the new scaling length of the CPP magnetoresistance implies that one is able to still measure an appreciable magnetoresistance effect in the CPP geometry at layer thicknesses exceeding the mean free path (where the CIP magnetoresistance vanishes).

Here, we will consider the case of magnetic multilayers consisting of an alternate stacking of single-domain ferromagnetic layers and nonmagnetic spacer layers. This model was developed by Valet and Fert [12, 39]. In the calculations a single parabolic conduction band with effective mass, m, and Fermi velocity, v_F, is assumed in all layers. The z-axis is defined as the axis perpendicular to the plane of the layers and we choose the x-axis as the spin quantization axis. The only configurations considered are those with the magnetic moments of the ferromagnetic layers pointing along the x-direction. The notation is such that $(+,-)$ indicates the absolute spin direction and $(\uparrow,\downarrow)$ the majority and minority spin directions, respectively. The model is limited to low temperatures where spin-flip scattering by electron-magnon interactions can be neglected and the only spin-flip scattering events are due to spin-orbit interactions. The following distribution function for the electrons of spin σ is introduced, which is a sum of the Fermi-Dirac distribution function, f^0, given by Eq. (3.5) and small perturbations:

$$f_\sigma(z,\boldsymbol{v}) = f^0(v) + \frac{\partial f^0}{\partial \epsilon}\{[\mu^0 - \mu_\sigma(z)] + g_\sigma(z,\boldsymbol{v})\}. \tag{3.9}$$

Here, $\epsilon = \frac{1}{2} m v^2$ and μ^0 is the equilibrium chemical potential. Apart from the term g_σ representing the "normal" displacement of the distribution function when a current is flowing, there is an additional term $\mu_\sigma(z)$ associated with the z-dependence of the chemical potential. This additional term makes the CPP description different from the CIP case. If one takes only linear terms in perturbation the Boltzmann transport equation reduces to

$$v_z \frac{\partial g_\sigma}{\partial z}(z,\boldsymbol{v}) + \left(\frac{1}{\tau_\sigma} + \frac{1}{\tau_{sf}}\right) g_\sigma(z,\boldsymbol{v}) = \left(v_z \frac{\partial \bar{\mu}_\sigma}{\partial z}(z) + \frac{\bar{\mu}_\sigma(z) - \bar{\mu}_{-\sigma}(z)}{\tau_{sf}}\right), \tag{3.10}$$

with $\bar{\mu}_\sigma(z) = \mu_\sigma(z) - e\,V$ the electrochemical potential for spin σ. The relaxation rates τ_σ and τ_{sf} are the usual relaxation rates associated with spin-conserving and spin-flip scattering events. They inversely add up to the total relaxation rate for momentum within each spin channel, τ'_σ, as $(\tau'_\sigma)^{-1} = \tau_\sigma^{-1} + \tau_{sf}^{-1}$. The term on the right-hand side in Eq. (3.10) proportional to τ_{sf}^{-1} reflects the relaxation of the nonequilibrium spin accumulation by spin-flip scattering processes. As already mentioned above, *spin mixing*, usually denoted as $\tau_{\uparrow\downarrow}$, which expresses momentum transfer from one spin channel to the other, is not taken into account here as it concerns a low-temperature limit. Valet and Fert show in Refs. 12, 39 that in the limit $\tau_\sigma \ll \tau_{sf}$, which is essentially the limit where the spin diffusion length

is much longer than the mean free path, the macroscopic transport equations derived by Johnson and Silsbee [40] or Van Son *et al.* [41] are recovered, i.e.

$$J_\sigma = \frac{1}{\rho_\sigma e}\frac{\partial \bar{\mu}_\sigma}{\partial z}, \tag{3.11a}$$

and

$$\rho_\sigma e \frac{\partial J_\sigma}{\partial z} = \frac{(\bar{\mu}_\sigma - \bar{\mu}_{-\sigma})}{l_\sigma^2}. \tag{3.11b}$$

Here, J_σ is the current density for spin σ and $\rho_\sigma = m/(n_\sigma e^2 \tau'_\sigma) = m\, v_F/(n_\sigma e^2 \lambda_\sigma)$ the resistivity for spin channel σ, where we introduced the mean free path, λ_σ, as $\lambda_\sigma = v_F\, \tau'_\sigma$. The spin diffusion length for spin σ is defined as

$$l_\sigma = v_F\,[\tau_{sf}\,(\tau_{sf}^{-1} + \tau_\sigma^{-1})^{-1}/3]^{1/2} \approx v_F\,(\tau_{sf}\,\tau_\sigma/3)^{1/2}. \tag{3.12}$$

Equation (3.11a) is just Ohm's law and Eq. (3.11b) expresses that the nonequilibrium chemical-potential difference between the two spin channels (or spin accumulation) due to the mismatch of the spin currents on either side of the interface is balanced by spin-flip scattering processes. Van Son *et al.* [41] have shown that one can deduce from Eqs. (3.11a) and (3.11b) a differential equation for $\Delta\mu = \frac{1}{2}(\mu_+ - \mu_-)$:

$$\frac{\partial^2 \Delta\mu}{\partial z^2} = \frac{\Delta\mu}{l_{sf}^2}, \tag{3.13}$$

with $l_{sf}^{-2} = l_\uparrow^{-2} + l_\downarrow^{-2}$. This leads to exponential variations with decay length l_{sf} for $\Delta\mu$, the current density J_σ, and the electric field $F(z) = (1/e)\,\partial\bar{\mu}/\partial z$. These variations have been shown in Fig. 3.1. In the case of multilayers with various successive interfaces, the interferences between them give rise to oscillations with a period equal to the multilayer period. When l_{sf} is much longer than the typical layer thicknesses, t, this oscillation amplitude becomes very small. In Ref. 12 for example, Valet and Fert show that the oscillation amplitude of $(J_+ - J_-)/(J_+ + J_-)$ vanishes as $(t/l_{sf})^2$. Therefore, in this limit, the current in each spin channel is conserved, which is a basic assumption in many theories on giant magnetoresistance.

The above model has been applied to calculate the CPP resistance of magnetic multilayers in both the situations where the magnetic moments of the ferromagnetic layers are aligned parallel and where they are antiparallel. The CPP magnetoresistance then follows directly from the difference between these two configurations in the usual way. Here, we present only the outcome of the calculations (for a complete derivation, see Ref. 12). To express the difference in the resistivities of the spin $\uparrow$ and spin $\downarrow$ electrons in the ferromagnetic layers a spin-asymmetry parameter β is used:

$$\rho_{\uparrow(\downarrow)} = 2\rho_F^*\,[1 - (+)\beta]. \tag{3.14}$$

Here, $\rho_F^* = \rho_F/(1-\beta^2)$ with ρ_F the experimentally measurable resistivity of the ferromagnetic layers ($\rho_N^* = \rho_N$ for the nonmagnetic spacer layers, where $\beta = 0$). An analogous definition can be formulated for the interface resistance, r, between the ferromagnetic and nonmagnetic layers arising from both diffuse and specular scattering. In this situation the spin-asymmetry parameter is denoted as γ:

$$r_{\uparrow(\downarrow)} = 2r_b^* \left[1 - (+)\gamma\right]. \tag{3.15}$$

The final result for the total resistance, R, of a multilayer system consisting of M bilayers in the parallel (P) and antiparallel (AP) configurations are:

$$R^{(\mathrm{P,AP})} = M(r_0 + 2r_{\mathrm{SI}}^{\mathrm{P,AP}}), \tag{3.16}$$

with

$$r_0 = (1-\beta^2)\rho_F^* t_F + \rho_N^* t_N + 2(1-\gamma^2)r_b^*, \tag{3.17}$$

and

$$r_{\mathrm{SI}}^{(\mathrm{P})} = \frac{\frac{(\beta-\gamma)^2}{\rho_N^* l_{\mathrm{sf}}^{(N)}} \coth\left(\frac{t_N}{2l_{\mathrm{sf}}^{(N)}}\right) + \frac{\gamma^2}{\rho_F^* l_{\mathrm{sf}}^{(F)}} \coth\left(\frac{t_F}{2l_{\mathrm{sf}}^{(F)}}\right) + \frac{\beta^2}{r_b^*}}{\frac{1}{\rho_N^* l_{\mathrm{sf}}^{(N)}} \coth\left(\frac{t_N}{2l_{\mathrm{sf}}^{(N)}}\right) \frac{1}{\rho_F^* l_{\mathrm{sf}}^{(F)}} \coth\left(\frac{t_F}{2l_{\mathrm{sf}}^{(F)}}\right) + \frac{1}{r_b^*} \times [\ldots}$$
$$\ldots \frac{1}{\rho_N^* l_{\mathrm{sf}}^{(N)}} \coth\left(\frac{t_N}{2l_{\mathrm{sf}}^{(N)}}\right) + \frac{1}{\rho_F^* l_{\mathrm{sf}}^{(F)}} \coth\left(\frac{t_F}{2l_{\mathrm{sf}}^{(F)}}\right)], \tag{3.18a}$$

$$r_{\mathrm{SI}}^{(\mathrm{AP})} = \frac{\frac{(\beta-\gamma)^2}{\rho_N^* l_{\mathrm{sf}}^{(N)}} \tanh\left(\frac{t_N}{2l_{\mathrm{sf}}^{(N)}}\right) + \frac{\gamma^2}{\rho_F^* l_{\mathrm{sf}}^{(F)}} \coth\left(\frac{t_F}{2l_{\mathrm{sf}}^{(F)}}\right) + \frac{\beta^2}{r_b^*}}{\frac{1}{\rho_N^* l_{\mathrm{sf}}^{(N)}} \tanh\left(\frac{t_N}{2l_{\mathrm{sf}}^{(N)}}\right) \frac{1}{\rho_F^* l_{\mathrm{sf}}^{(F)}} \coth\left(\frac{t_F}{2l_{\mathrm{sf}}^{(F)}}\right) + \frac{1}{r_b^*} \times [\ldots}$$
$$\ldots \frac{1}{\rho_N^* l_{\mathrm{sf}}^{(N)}} \tanh\left(\frac{t_N}{2l_{\mathrm{sf}}^{(N)}}\right) + \frac{1}{\rho_F^* l_{\mathrm{sf}}^{(F)}} \coth\left(\frac{t_F}{2l_{\mathrm{sf}}^{(F)}}\right)]. \tag{3.18b}$$

The thicknesses t_F and t_N are those of the ferromagnetic and the nonmagnetic layers, respectively, whereas $l_{\mathrm{sf}}^{(F)}$ and $l_{\mathrm{sf}}^{(N)}$ denote the spin diffusion lengths in the ferromagnetic and nonmagnetic layers, respectively. The spin diffusion length in the nonmagnetic layers is related to the mean free path $\lambda^{(N)}$ by $l_{\mathrm{sf}}^{(N)} = (\lambda^{(N)}\lambda_{\mathrm{sf}}^{(N)}/6)^{1/2}$ with $\lambda_{\mathrm{sf}} = v_F \tau_{\mathrm{sf}}$, which is a similar relation as Eq. (3.12) for the ferromagnetic layers. Equations (3.18a) and (3.18b) look rather intransparent, but it turns out that they become extremely simple in the limit of infinite spin diffusion length.

3.2.2 Limit of infinite spin-diffusion length

When $l_{\mathrm{sf}}^{(F)} \gg t_F$ and $l_{\mathrm{sf}}^{(N)} \gg t_N$, Eqs. (3.16)-(3.18b) turn into the following simple relations already derived by Pratt *et al.* [43–46]:

$$R^{(\mathrm{AP})} = M(\rho_F^* t_F + \rho_N^* t_N + 2r_b^*), \tag{3.19a}$$

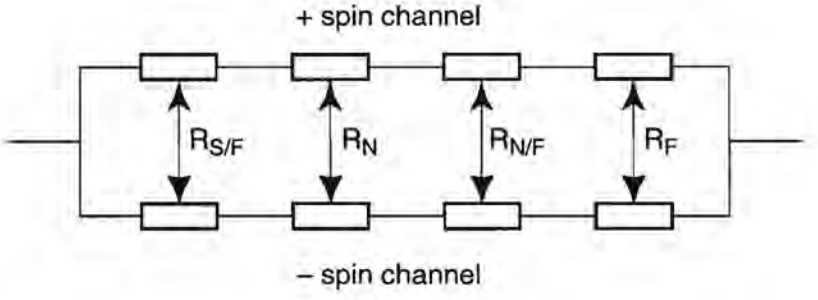

Figure 3.2. *Equivalent resistor scheme of the two-current model as proposed by the Michigan State University group [47]. Here, $A\,R_{S/F}=r_{S/F}$ and $A\,R_{N/F}=r$, where A denotes the area of the multilayer. Similarly, $A\,R_N=\rho_N\,t_N$ and $A\,R_F=\rho_F\,t_F$.*

$$\frac{1}{R^{(\mathrm{P})}} = \frac{1}{M}\left(\frac{1}{2\rho_F^*(1-\beta)t_F + 2\rho_N^* t_N + 4r_b^*(1-\gamma)} + \frac{1}{2\rho_F^*(1+\beta)t_F + 2\rho_N^* t_N + 4r_b^*(1+\gamma)}\right), \tag{3.19b}$$

and eventually, by combining Eqs. (3.19a) and (3.19b),

$$\sqrt{(R^{(\mathrm{AP})} - R^{(\mathrm{P})})R^{(\mathrm{AP})}} = \beta\frac{t_F}{t_F + t_N}\rho_F^* L + 2\gamma r_b^* M. \tag{3.20}$$

L denotes the total thickness of the sample and is defined by $L = M(t_F + t_N)$. These equations are precisely the outcome of a two-channel model, in which for a multilayer of unit area the total resistance within each spin channel is just the sum of the resistivities times the thicknesses of the ferromagnetic and nonmagnetic layers plus the various interface resistances. To be more specific, for the experiments of Refs. 43–46, where they used superconducting Nb contacts to define their CPP measuring geometry and to create a nicely uniform current-distribution pattern, expressions of the form

$$R^{(+,-)} = 2\,r_{S/F} + (M+1)\,\rho_F^{(+,-)}\,t_F + M\,\rho_N\,t_N + 2\,M\,r_{+,-} \tag{3.21}$$

were formulated for each spin $(+,-)$ channel. This resistor scheme is depicted in Fig. 3.2. Here, $2\,r_{S/F}$ represents the interface resistance between the two superconducting current leads and the ferromagnetic layers at the outer boundaries of the multilayer stacking. Assuming M sufficiently large to neglect the difference between M and $(M+1)$ and inserting the appropriate resistivity values for the

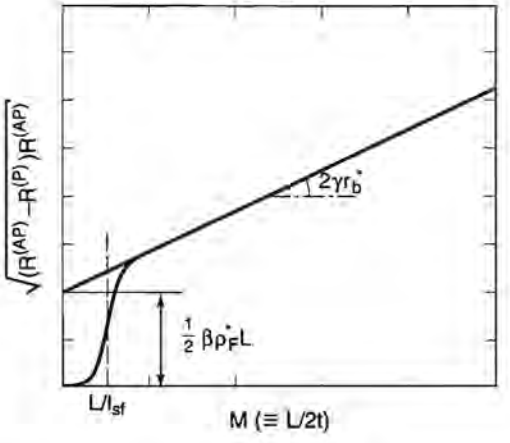

Figure 3.3. $\sqrt{(R^{(AP)} - R^{(P)})R^{(AP)}}$ *as a function of the number of bilayers, M, with a fixed total sample thickness, L. For simplicity, the individual thicknesses of the magnetic and nonmagnetic layers are chosen equal and set to t, so that L=2 t M. The slope of the linear variation, which is expected for* $l_{sf} \gg t$ ($M \gg L/l_{sf}$), *can be derived from Eq. (3.20). When* $M < L/l_{sf}$ *deviations from this linearity occur.*

parallel and antiparallel situations (adding eventually the total resistances of each spin channel in parallel) one obtains again Eqs. (3.19a)-(3.19b).

As an illustration, in Fig. 3.3 we plot $\sqrt{(R^{(AP)} - R^{(P)})R^{(AP)}}$ as a function of the number of bilayers for a fixed total sample thickness L with equal thicknesses of the ferromagnetic and nonmagnetic layer. This kind of plots has been experimentally verified by numerous low-temperature studies at the Michigan State University [43–46] and, more recently, also by Gijs *et al.* [48] who were able to measure the CPP magnetoresistance up to room temperature of multilayers evaporated on specially prepared grooved InP-substrates. The important spin-asymmetry parameters determining the magnitude of the magnetoresistance can be easily deduced from plots like the one of Fig. 3.3; the slope essentially gives the interface asymmetry parameter, γ, whereas the intercept with the vertical axis reveals the bulk asymmetry parameter, β. Moreover, the linear variation itself is already an indication that the assumption of a very long spin diffusion length is valid. Deviations from this linearity is expected to occur for finite spin diffusion lengths, i.e. on the left-hand side of the dashed line in Fig. 3.3.

3.3 Other Models

3.3.1 The Kubo formalism

Here, we will briefly outline the magnetoresistance theory of Levy, Zhang, and Fert [37,38] which is based on the Kubo formula [49]. Consider the case of a magnetic multilayer with individual layer thicknesses L_M and L_N for the magnetic and nonmagnetic layers, respectively. In their approach a local in-plane conductivity σ is dependent on the coordinate z perpendicular to the multilayer planes (lattice planes). An essential difference with the semiclassical model is the representation of the electron by a wave packet having (spin dependent) scattering probabilities at the interfaces or bulk lattice planes. A scattering potential of the form

$$V_{\text{scat}} = \sum_l V_l(\boldsymbol{\sigma})\,\delta(\boldsymbol{r} - \boldsymbol{r}_l) \tag{3.22}$$

is introduced, where $\boldsymbol{r} = (\boldsymbol{r}_\parallel, z)$ and $V(\boldsymbol{\sigma}) = v + j\,\boldsymbol{\sigma}\cdot\boldsymbol{M}$, with $\boldsymbol{M}$ a unit magnetization vector and $\boldsymbol{\sigma}$ the Pauli spin operator. Bulk scattering is assumed to occur throughout the sample due to imperfections and impurities in the bulk; no contribution from thermally excited phonons or magnons is taken into account, which limits the validity of this description to low temperatures. Interface scattering is assumed to be due to interface roughness, i.e. magnetic atoms situated in a nonmagnetic environment and vice-versa. Both bulk and interface scattering are taken to be spin dependent. For simplicity, local scattering is assumed, which means that the scattering potentials have zero range. Therefore, they are modeled as random in the plane of the layers and a δ function in the z direction. The model now contains five parameters. The strength of the scattering is represented by the potentials v_i, v_l^{M}, and v_l^{N} for scattering at the interfaces, within the magnetic layers, and within the nonmagnetic layers, respectively. The spin dependence of the scattering is characterized by p_i and p_l^{M}, where $p \equiv j/v$; the scattering in the nonmagnetic layers is not spin dependent, i.e. $p_l^{\text{N}} = 0$.

In their first calculations, Levy, Zhang, and Fert used the Kubo formula in momentum space to describe the giant magnetoresistance effect in the CIP geometry. For this geometry, the electric field parallel to plane of the layers is constant and uniform within the plane, and the local conductivity σ becomes only dependent on the coordinate z. The full calculation is of this so-called one-point conductivity $\sigma(z)$ is given in Ref. [37] and the outcome is summarized below. One should note that Eqs. (3.23)-(3.25) are only valid when the magnetizations of the magnetic layers are either parallel or antiparallel:

$$\sigma_{\text{CIP}}(z) = \frac{ne^2}{2m}\sum_\sigma \frac{\hbar}{E^\sigma(z)}, \tag{3.23}$$

with

$$E^{\sigma}(z) = \frac{\hbar^2 k_F}{m\lambda^{\sigma}} \left\{ \sum_i \mathrm{Re}\ \Delta_i^{\sigma}\ \mathrm{e}^{-|z-z_i|/\lambda^{\sigma}} + \sum_l \mathrm{Re}\ \Delta_l^{\sigma}\ \mathrm{e}^{-|z-z_l|/\lambda^{\sigma}} \right\}, \tag{3.24a}$$

$$\lambda^{\sigma} = L \left\{ \sum_{i \in L} \mathrm{Re}\ \Delta_i^{\sigma} + \sum_{l \in L} \mathrm{Re}\ \Delta_l^{\sigma} \right\}^{-1}, \tag{3.24b}$$

and

$$\mathrm{Re}\ \Delta_i^{\sigma} = \frac{1}{\lambda'} \left\langle \sigma | (1 + p_i\, \boldsymbol{\sigma} \cdot \boldsymbol{M}_i)^2 | \sigma \right\rangle, \tag{3.25a}$$

$$\mathrm{Re}\ \Delta_l^{\sigma} = \frac{a_0}{\lambda_l} \left\langle \sigma | (1 + p_l\, \boldsymbol{\sigma} \cdot \boldsymbol{M}_l)^2 | \sigma \right\rangle. \tag{3.25b}$$

Here n is the free electron density, e the electronic charge, m the electron mass, k_F the Fermi wave number, and L $[= 2 \times (L_{\mathrm{M}} + L_{\mathrm{N}})]$ one period of the superlattice. The summation in Eq. (3.23) is over the two spin directions; z_i and z_l in Eq. (3.24a) represent the position of a M/N interface and a lattice plane, respectively. The summations in Eq. (3.24b) are over interfaces and lattice planes within one superlattice period L. Equations (3.25a) and (3.25b) contain the scattering matrix elements at the M/N interface and in the bulk, respectively. $\boldsymbol{M}_i$ and $\boldsymbol{M}_l$ denote the magnetization at an interface and a lattice plane, respectively; p_i and p_l, defined above, should not be confused with the ratios of spin-up over spin-down scattering, but they are related via $\alpha = \lambda_{\uparrow}/\lambda_{\downarrow} = (1+p)^2/(1-p)^2$. The quantities λ' and λ_l are fitting parameters determining the magnitude of the scattering lengths due to interface and bulk scattering, respectively. The lattice plane distance is denoted by a_0. To calculate the MR, an average of Eq. (3.23) over the z coordinate must be taken for the situations of parallel and antiparallel alignments.

Equation (3.24b) shows that both interface and bulk scattering contribute on equal footing to the mean free path. This is a noticeable difference from the Boltzmann approach described in the preceding sections. Furthermore, this theory also accounts for the finite conductivity for a thin film without bulk scattering, whereas the Fuchs-Sondheimer theory [Eq. (3.8)] gave the unphysical result of an infinite conductivity due to complete shunting in the bulk, as we noted before.

In the CPP geometry, the situation is substantially different. In that case, spin accumulation effects, as discussed in the previous section, play a role, which is accounted for by spin-dependent chemical potentials or "effective" electric fields. These fields are not uniform through the multilayer system, as for the CIP-case, but vary from one layer to another. Neglecting spin-flip scattering, i.e. in the limit of a long spin diffusion length, the currents in each spin channel are constant,

though not necessarily equal. In this case, the expression for the conductivity becomes much simpler than for the CIP-case [Eq. (3.23)] (see Refs. 36, 37, 50):

$$\sigma_{\mathrm{CPP}}(z) = \frac{n\,e^2}{2\,\hbar\,k_F} \sum_{\sigma} \lambda^{\sigma}. \tag{3.26}$$

In other words, for the CPP geometry it turns out that the resistivity of each spin channel is self-averaging, which means that the total resistivity is determined by just the sum of all scattering processes.

It may be instructive to consider some limiting situations. When the mean free path is very small, the CIP magnetoresistance vanishes, whereas this is not true for the CPP magnetoresistance. On the other hand, for extremely long λ, the z dependence of the conductivity disappears and also the resistivity in the CIP geometry becomes self-averaging. Then, the following expressions for the magnetoresistance can be deduced in case of only bulk or interface scattering [37]. For only interface scattering, we obtain

$$\mathrm{MR}_i = \frac{4\,p_i^2}{(1+p_i^2)^2} = \left(\frac{1-\alpha}{1+\alpha}\right)^2, \tag{3.27a}$$

and for only bulk scattering

$$\mathrm{MR}_b = \frac{4\,p_l^2}{(1+p_l^2+L_{\mathrm{N}}/L_{\mathrm{M}})^2}. \tag{3.27b}$$

Equation (3.27a) is exactly the outcome of a simple two-current model with all scattering processes spin-dependent. The term $L_{\mathrm{N}}/L_{\mathrm{M}}$ in the denominator of Eq. (3.27b), on the other hand, can be regarded as the part of the magnetic multilayer that is magnetically inert, since for the nonmagnetic layers $p = 0$, i.e. they do not contribute to the magnetoresistance.

3.3.2 The Landauer-Büttiker formalism

This section addresses the perpendicular electronic transport in metallic magnetic multilayers on the basis of the Landauer-Büttiker scattering formalism as it was developed by Bauer *et al.* [51–54]. In this approach charge and spin accumulation effects in the multilayers are implicitly integrated out. Spin-flip scattering is neglected which limits the theory to low temperatures. Firstly, the ballistic regime is discussed, followed by the introduction of imperfections in the bulk of the various layers and at the interfaces.

The Landauer conduction formula at temperatures well below the Fermi energy expresses the conductance G of a sample in terms of the transmission probabilities $|t_{n,m,\sigma}|^2$ between the different modes n and m with spin σ at the Fermi energy, E_F, of two perfect leads with low impedance [55]:

$$G = \frac{e^2}{h}\,\mathrm{Tr}\,\mathbf{t}\mathbf{t}^{\dagger} = \frac{e^2}{h} \sum_{nm,\sigma} |t_{nm,\sigma}|^2. \tag{3.28}$$

The leads are connected to contacts which are assumed to be in thermodynamic equilibrium with a small electrochemical potential difference. Equation (3.28) neglects inelastic and spin-flip scattering, which is allowed in case the inelastic and spin-flip relaxation lengths are much longer than the sample size. Figure 3.4(a) shows a schematic picture of a two-contact geometry in which the conductance is assumed to be determined by a very narrow sample region. In such a configuration the above condition of small sample size is fulfilled and, moreover, the Landauer-Büttiker formalism can be well applied. The complications arising from nonequilibrium spin polarization near the interfaces between magnetic and nonmagnetic layers, as was discussed in section 3.2, are not important here and can be disregarded as the conduction is limited by a sample region much smaller than the spin diffusion length l_{sf}. This means, however, that the temperature dependence of the magnetoresistance cannot be described by this theory, since thermally induced electron-magnon scattering shortens l_{sf}.

For a small sample, but sufficiently large compared to the Fermi wavelength, which is typical of the order of a lattice constant, the incoming and outgoing states n and m are Bloch waves at the Fermi energy. For simplicity, these are approximated by plane waves, so that in the ballistic regime without scatterers the conductance of the sample reads:

$$G_0 = \frac{2\,e^2}{h}\,\frac{S\,k_F^2}{4\,\pi}, \tag{3.29}$$

where k_F denotes the Fermi wave vector. Here, the cross section, S, of the sample completely determines the conductance. Figure 3.4(a) depicts a multilayer consisting of an alternate stacking of a nonmagnetic metal N and a metal M which may be a ferromagnet. The arrows indicate the directions of the magnetization vectors in the various magnetic layers. In this situation the Fermi energies in the layers are matched and the relative shifts of the conduction bottoms may be sketched as is done in Figs. 3.4(b) and 3.4(c) for the case of an antiparallel alignment of the successive magnetic layers. Reflection of the conduction electrons at the potential barriers lowers the conductivity below G_0 even in the absence of scattering by impurities or imperfections. In the semiclassical approximation the transmission is zero for modes with a kinetic energy normal to the layers smaller than the potential barrier, $\Delta U = U_M - U_N$. So, the contact conductance is then given by

$$G_{con} = G_0 \left(1 - \frac{\max\{0, \Delta U\}}{E_F}\right). \tag{3.30}$$

Applying relation (3.30) to the different magnetic configurations where the magnetic layers are aligned parallel (P) and antiparallel (AP), the magnetoconductance ratio $\Delta G_{con}/G_0 \equiv (G_{con}^{(P)} - G_{con}^{(AP)})/G_0$ can be easily calculated, which results in

$$\frac{\Delta G_{con}}{G_0} = \frac{\max\{0, \Delta U_{min}\} - \max\{0, \Delta U_{maj}\}}{2\,E_F}. \tag{3.31}$$

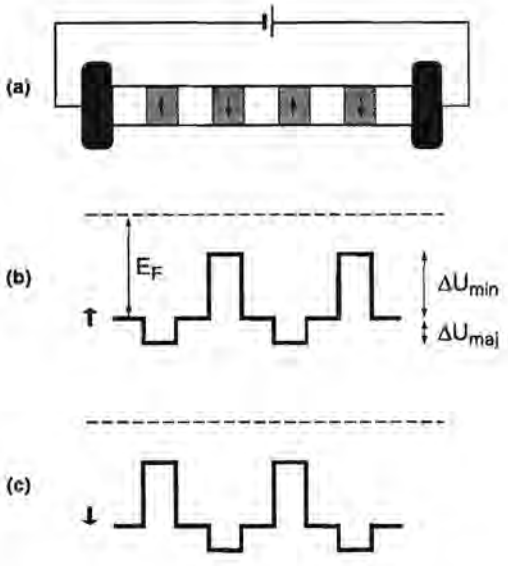

Figure 3.4. *(a) Schematic sample representation consisting of x bilayers of nonmagnetic and ferromagnetic material. As is assumed in the text, the conductance is fully determined by the sample alone. The contacts are in thermodynamic equilibrium with a small potential difference. The arrows indicate the directions of the magnetization vectors in the various magnetic layers. (b) Potential landscape for spin-up electrons when the magnetic layers are oriented antiparallel. (c) The same as (b), but for the spin-down electrons.*

ΔU_{min} and ΔU_{maj} are the potential barriers for the minority and majority spin channels, respectively, with $\Delta U_{\text{maj}} < \Delta U_{\text{min}}$. Note that, according to Eq. (3.31), only the first two multilayer periods contribute to the magnetoconductance ratio in the ballistic regime, since no scattering is taken into account.

In the case of interface roughness and bulk impurities or imperfections the additional scattering processes will result in an enhancement of the backscattering of the conduction electrons at the successive interfaces. The interface roughness is modeled by short-range scattering potentials, γ_i, that are randomly distributed over the interface with a density n_i. Also within the bulk of the nonmagnetic and magnetic layers (with thicknesses L_{N} and L_{M}, respectively), randomly distributed point scatterers are assumed. When ΔU is set to zero, which for the case of Fe/Cr, for example, is a very reasonable assumption since potential barriers are very small or negative, Bauer deduced a very simple analytical expression for the

conductance, normalized to G_0, of the channel with spin σ [51,56]:

$$G_\sigma = 1 - \frac{2x}{\bar{x}_\sigma} + 2\left(\frac{x}{\bar{x}_\sigma}\right)^2 \ln\left(1 + \frac{\bar{x}_\sigma}{x}\right). \tag{3.32}$$

Here, x denote the number of multilayer repeats and $\bar{x}_\sigma$ is the mean number of traversed interfaces for spin σ. This means that $\bar{x}_\sigma\,(L_N + L_M) \equiv \bar{x}_\sigma\, L$ is the global mean free path normal to the interfaces. The magnetoconductance can now be easily calculated by evaluating both the situations where the magnetizations of the magnetic layers are aligned parallel (P) and antiparallel (AP). In the parallel case the conductance can be simply written as the sum of the conductances of the spin-up and spin-down channels $G^P = \frac{1}{2}(G_\uparrow + G_\downarrow)$, whereas for the AP-alignment the total conductance is given by Eq. (3.32) with $(\bar{x}^{AP})^{-1} = \frac{1}{2}(\bar{x}_\uparrow^{-1} + \bar{x}_\downarrow^{-1})$. The magnetoconductance (or magnetoresistance MR) then becomes $MR = (G^P - G^{AP})/G^{AP}$ with $\bar{x}_\uparrow/\bar{x}_\downarrow \equiv \bar{\alpha}$ as a fitting parameter representing the integrated contributions of both interface and bulk scattering within the magnetic layers. It can be seen as an average spin-asymmetry parameter as it often appears in the literature.

A final remark will be made at this point. Bauer *et al.* [56] argued that the Landauer-Büttiker formalism is well suited to include real band-structure effects as to go beyond the effective mass and semiclassical approximations. This may be necessary for multilayers consisting of $3d$ transition metals for instance, since in reality the s and d electrons are strongly hybridized. Recently, Schep *et al.* [57,58] succeeded in calculating the magnetoresistance effect from first principles in the ballistic limit (i.e. no scattering) for Fe/Cr and Co/Cu multilayers both in the current-in-plane (CIP) direction and in the current-perpendicular-to-plane (CPP) direction. For the CIP case they found very low magnetoresistance values, far below experimentally measured MR ratios. For the CPP case on the other hand, MR values of the order of 100% were calculated on the basis of band structure effects only. These values are indeed close to the ones experimentally found, which suggests that taking into account the real band structure of the multilayer may be very important towards the understanding of the giant magnetoresistance effect. Up to now, however, results of a full calculation including both band-structure effects as well as scattering, which is obviously present in all experimentally measured structures in the literature, have not yet been obtained.

Chapter 4

Current-In-Plane Magnetoresistance Experiments

4.1 Electrodeposited Co/Cu Multilayers*

This section reports on the structural and electrical characterization of electrodeposited Co/Cu multilayers grown in a single electrolyte based on $CoSO_4$ and $CuSO_4$. A high degree of crystallographic orientation and superlattice coherence is found in the growth on (100)- and (111)-oriented substrates. The magnetoresistance (MR), measured in the current-in-plane configuration at room temperature, is dominated by the giant MR-effect for Cu-layer thicknesses $d_{Cu} \gtrsim 3\,nm$ and by the anisotropic MR-effect for $d_{Cu} \lesssim 2.5\,nm$. A maximum of 14% is measured for $d_{Cu} \approx 4\,nm$. No evidence for antiferromagnetic coupling is found. Instead, the giant MR gradually diminishes with decreasing $d_{Cu} < 4\,nm$, which is attributed to ferromagnetic coupling due to magnetic pinholes. The influence of the Cu^{2+}-ion concentration, the addition of leveling agents, and the Co- and Cu-layer thicknesses on the structure and magnetoresistance is systematically investigated. Especially the use of leveling agents has a catastrophic effect on the structural quality of the multilayers and on the magnitude of the MR.

4.1.1 Introduction

In the past few years magnetic multilayers have been the subject of tremendous scientific effort. This effort is mainly based on the very interesting magnetic and electrical phenomena that can be observed in these artificially layered structures, such as the oscillatory exchange coupling between magnetic layers across nonmagnetic spacer layers and the so-called giant magnetoresistance (MR) effect [59]. For this to be observed, a fair control over the deposition parameters is needed, since rough interfaces between subsequent layers can easily destroy the effect. That is why most of the samples which exhibit large coupling strengths and high MR values have been prepared by sputtering, molecular beam epitaxy (MBE), or other vacuum-based techniques [59]. Recently, Alper *et al.* [60,61] and Hua

* Apart from small changes, this section has been published in J. Magn. Magn. Mater. **148**, 455 (1995).

et al. [62] have reported giant magnetoresistance in Co-Ni/Cu multilayers grown by electrodeposition in a single electrolyte. The concept of multilayer growth by electrodeposition is not a new one [63]. The advantage over vacuum-based techniques mainly lies in the simplicity of the experimental setup. However, growing high quality multilayers that exhibit appreciable giant MR values still remains a challenge. Electrodeposition offers the promising possibility of growing wire-like multilayer structures with very large height-to-width aspect ratios as recently demonstrated by Blondel *et al.* [15] and Piraux *et al.* [16], which enables the study of the giant MR effect with the current perpendicular to the multilayer planes (the so-called CPP MR). Until recently, this could only be realized either by superconducting contacts [13], which limits the measurements to low temperatures, or by advanced microstructuring [64, 65], which results in structures having rather poor aspect ratios compared to the electrodeposited wires. As mentioned above, high quality electrodeposited samples which show giant MR values comparable with those of sputtered or MBE-grown multilayers are scarce, mainly due to a lack of thickness control and growth homogeneity, making the very thin spacer-layer thickness regime of antiferromagnetic (AF) coupling ($\lesssim 3\,\mathrm{nm}$) not yet accessible. For the CPP MR this is less a problem than for the case where the current is flowing in the planes of the layers (the CIP geometry) because of the different length scales involved for the MR effect (see Ref. 12 and section 3.2). Most of the data in the literature on electrodeposited magnetic multilayers deals with the Co/Cu, Ni/Cu, and Co-Ni/Cu systems [60–63, 66–68]. Until now, however, CIP MR results have been reported for Co-Ni/Cu multilayers only [60–62].

In this section we report on a magnetoresistance study of electrodeposited Co/Cu multilayers using a sulfate-based electrolyte containing both Co^{2+} and Cu^{2+} ions. First we will give an outline of the experimental procedures, after which the characterization of the multilayers is presented. A large number of growth parameters has systematically been varied, such as the substrate texture, growth rate, Cu^{2+}-ion concentration, and the use of additives. Special attention has been paid to controlling the layer thicknesses and the crystallographic orientation. We are able to distinguish between (100)- and (111)-oriented multilayers. In a separate section the results of the magnetoresistance measurements, where both the magnetic and the nonmagnetic layer thicknesses have been varied, are discussed.

4.1.2 Experimental

Magnetic Co/Cu multilayers (MLs) are grown by electrodeposition (also termed electroplating) in an electrolyte containing both Co^{2+} and Cu^{2+} ions (single bath method) with the composition controlled by periodically switching the potential of the substrate (pulsed potentiostatic deposition) [69–73]. The aqueous electrolyte is based on $CoSO_4$ and $CuSO_4$. The starting solution consists of $1\,l\,H_2O$ to which $400\,g\ CoSO_4{\cdot}7H_2O$ and $40\,g\ H_3BO_3$ (boric acid) is added. Copper is added

at a low concentration, typically 2 g $CuSO_4 \cdot 5H_2O$. For 1 *l* of solvent H_2O, these amounts correspond to 1.2 mol, 0.55 mol, and 6.8×10^{-3} mol of Co^{2+}, H_3BO_3, and Cu^{2+}, respectively. The pH of this solution is found to be $\approx$ 4-4.5. All results discussed in this section have been obtained for 2 g $CuSO_4 \cdot 5H_2O$ (6.8×10^{-3} mol/*l* = 6.8 mM), except where the dependence of the magnetoresistance on the Cu^{2+} concentration is investigated. In that case, the concentration has been varied in the range 1-100 mM. The effect of the addition of a leveling agent (also called brightener), i.e. a surfactant thought to level out surface roughness, has been tested for the two agents thiourea (CH_4N_2S) and a polyoxyethylene compound Triton X-100 for concentrations of 0.02 g/*l* and 0.5 ml/*l*, respectively [74]. The electrolyte is used without agitation at room temperature.

Electroplating is done in a teflon cell with the substrate (cathode) facing upwards. There is no separate compartment for the counter electrode (anode), which is a Pt plate of about 10 cm^2. A saturated-calomel electrode (SCE) was used as a reference for the applied potential. This electrode is placed $\approx$ 7 mm above the substrate. The center part of the substrate is exposed to the electrolyte via an O-ring seal of size 9 mm in diameter which determines the growth area. The effective growth diameter ($\approx$ 7.5 mm) is, however, somewhat smaller because of boundary effects.

All substrates used originate from 4-inch Si(100) wafers which are segmented by grooves into pieces of size 14×14 mm^2. This facilitates the cleaving-out of one substrate piece. The two types of substrates used differ in the base metal-film which has been evaporated onto the Si wafers prior to electroplating. For substrate A this is a 50 nm Au film electron-beam evaporated at a rate of 0.3 nm/s and for substrate B it is a 20 nm Cu film magnetron sputtered at a rate of 0.2 nm/s. During sputtering or evaporation of the base layer, the Si wafer remains at room temperature. Prior to the growth, the wafers are cleaned and hydrogen passivated using a conventional HF treatment. In the following we will refer to substrate A and B as the Au- and the Cu-substrate, respectively. The major difference between the two substrates is a difference in crystallographic orientation. The Au-substrate exhibits a strong (111) texture in contrast to the Cu-substrate which is predominantly (100) oriented. This allows the study of electroplating for two different crystallographic orientations. The substrates are stored in an ambient atmosphere during a period ranging from 1 week to a few months.

Before electroplating the two substrates are cleaned by two different methods. The Au-substrate is exposed to ozone in an ultraviolet ozone reactor during 10 min which results in a clean surface as demonstrated by its perfect wetability by water. The Cu-substrate is dipped during approximately 1 min into a 10% H_2SO_4 solution in order to remove the surface oxide and then carefully rinsed in H_2O. After the specific cleaning treatment, both substrates are mounted into the electrochemical cell within 5 min and covered by the plating electrolyte. If – in case of the Au-substrate – the cleaning step is omitted, the electroplated multilayer is

of poor optical quality. There are deep cracks which presumably arise from stress that has been built up.

The electroplating commences by pulsed potentiostatic deposition [69–73]. Cu is deposited at the substrate potential $U_{Cu} = -0.58\,V_{SCE}$, which is the experimentally determined equilibrium potential for the reaction $Co \rightleftharpoons Co^{2+} + 2e^-$ (Co^{2+} concentration 1.2 M). Since Cu is much more noble than Co, Cu^{2+} is reduced at this potential and a Cu film is formed. Because of the low concentration of Cu^{2+} ions (6.8 mM), the reduction rate is not kinetically limited, but rather by mass transport (diffusion and convection). Typical current densities for the Cu^{2+} reduction are $\approx 100\,\mu A/cm^2$. Co is deposited at more negative substrate potentials of $U_{Co} = -1.2$ to $-1.6\,V_{SCE}$ and, because of the much higher ion concentration, with much larger current densities of 10 to 40 mA/cm^2, about 200 times larger than the Cu^{2+} current density. During the Co growth, Cu^{2+} continues to be reduced. Therefore, Cu can be built in into the Co layer as impurities.

The growth procedure is as follows. First, the potentiostat is turned on at the electrode potential U_{Cu}. After a delay of about 30 s the Cu-diffusion layer has been built up. The total charge due to Cu^{2+} reduction during this initial phase corresponds to an initially grown Cu layer of approximately 10 nm in thickness. Subsequently, the procedure is continued with a pulse at potential U_{Co} during a time T_{Co} to deposit the Co layer, followed by a longer period T_{Cu} at potential U_{Cu} to plate the Cu layer. This Co/Cu-cycle is repeated 50 times for all multilayers grown. The individual thicknesses of the Co and Cu layers are controlled by the charge Q_{Co} and Q_{Cu} passed during the time intervals T_{Co} and T_{Cu}, respectively. The two charges are measured by a computer and maintained constant during the growth by adjusting the time intervals. To give an example, one unit of Co/Cu of thickness 2/4 nm corresponds in our setup approximately to $T_{Co} = 250$ ms and $T_{Cu} = 100$ s. Hence, a stack of 50 repeats takes 1.5 h to complete. A measured current trace is shown in the inset of Fig. 4.1.

After electroplating, the samples are analyzed as follows: **i)** An X-ray diffraction pattern is measured in the θ-2θ mode using Cu-Kα radiation. **ii)** Some series of multilayers are analyzed by X-ray fluorescence (XRF) spectroscopy to determine the chemical composition. **iii)** The center part of the grown multilayer, typically $5 \times 5\,mm^2$, is cleaved out and further used to measure the electrical sheet resistance using the conventional 4-point Van der Pauw method (Ref. 23 and section 2.2.3). Since the substrate sheet resistance is known, the resistance of the multilayer can be determined. Furthermore, the knowledge of the respective sheet resistances allows the accurate correction of the measured magnetoresistance for substrate shunting. **iv)** The magnetic hysteresis loop is determined in a vibrating sample magnetometer (VSM) with the externally applied magnetic-field oriented in the plane of the film. **v)** Finally, the CIP MR is measured at room temperature.

In the following, some systematic investigations of, e.g., the dependence of the magnetoresistance on the Cu-layer thickness, will be presented. Each sample

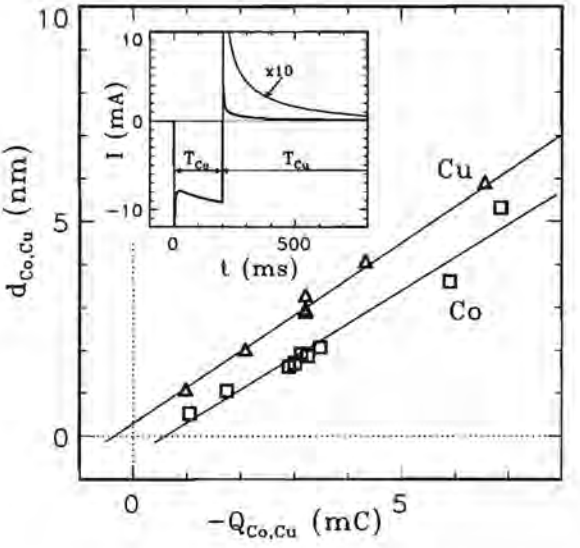

Figure 4.1. *Relation between the mean Co(Cu)-layer thickness, d_{Co} (d_{Cu}), obtained from X-ray fluorescence analysis and the electric charge, Q_{Co} (Q_{Cu}), transferred at the cathode; squares correspond to Co, triangles to Cu. The lines are least-square fits.* **Inset:** *Electric cathode-current transient caused by a negative voltage pulse of potential $U_{Co} = -1.4\,V_{SCE}$ during T_{Co}, applied to plate a Co layer. The Cu layer is formed during the time interval T_{Cu} when the electrode potential is held at $U_{Cu} = -0.58\,V_{SCE}$.*

(multilayer) within one series has been grown shortly after each other under identical conditions. Samples originating from different series may have nominally been grown under identical conditions, but they still may differ, either because the solution has not always been renewed before growing a new series, or the substrates differ in age. The latter appears particularly relevant for the Cu-substrate, which is less noble than the Au-substrate.

4.1.3 Sample characterization

In this section the compositional and structural analyses of as-grown Co/Cu multilayers are discussed. The result of an XRF compositional analysis is shown in Fig. 4.1. The inset displays the current transient measured while pulsing the electrode potential negatively to U_{Co} for the deposition of the Co layer. The current integrated during the pulse duration T_{Co} is the charge Q_{Co}, which is held fixed for each multilayer. Similarly, Q_{Cu} is the charge passed during the

idle period T_{Cu} when the Cu layer is plated. Multilayers have been grown that differ in $Q_{Co,Cu}$ only. XRF analysis allows us to determine the absolute number of Co and Cu atoms per unit surface area. Using the appropriate volume per atom of bulk Co and Cu and the number of layer repeats, the mean Co and Cu layer thicknesses $d_{Co,Cu}$ can be derived. The obtained relation between $d_{Co,Cu}$ and $Q_{Co,Cu}$ is shown in Fig. 4.1 (squares correspond to Co and triangles to Cu).

According to Faraday's law, the number n of electroplated atoms is proportional to the charge Q. In case of 100% current efficiency, i.e. the whole measured current is due to the reduction of Co^{2+} and/or Cu^{2+} ions, the relation reads $n = Q/ez$, where e is the charge of the electron and z the electrovalency of the $Co^{2+}(Cu^{2+})$ ions ($z = 2$). We therefore expect a linear relation between d and $-Q$. The measurement points in Fig. 4.1 have accordingly been fitted to straight lines. The slopes are 770 nm/C and 840 nm/C for Co and Cu, respectively. These two values are in excellent agreement taking into account the atomic volume ratio between Co and Cu atoms, which is 0.93. Hence, d_{Co} is 7% smaller than d_{Cu} for identical charges. We have also analyzed several films where either Co at potential U_{Co} or Cu at potential U_{Cu} was electroplated. These samples serve as references. In contrast to the Cu reference, in which no impurities are found by XRF, Co reference samples typically include 4 at.% Cu. From Cu-reference samples a Cu-growth rate of 837 nm/C is obtained. This rate is in very good agreement with the one that has been obtained from multilayers. Since Cu is grown at moderately negative voltages, we may assume a 100% current efficiency, i.e. the absence of hydrogen evolution (reduction of H^+). The obtained growth rate then allows the determination of the effective growth diameter for our experiment, which is 7.5 mm and consistent with the apparent growth diameter. Furthermore, since the rate of 770 nm/C for Co in multilayers is in agreement with the Cu-growth rate, the current efficiency is apparently also 100% for the pulsed electrodeposition of Co. We mention that this is not necessarily the case for thick Co films. From electroplated Co reference films grown in the electrolyte with the brightener thiourea, we also deduce an efficiency of 100% for U_{Co} in the range from -1.0 to $-1.4\,V_{SCE}$. Without thiourea, however, the efficiency is determined to be only 78% at $-1.4\,V_{SCE}$.

In Fig. 4.1 it is observed that the fitted lines of the d-vs-Q relations do not cross the origin of the coordinate system. For Co, the line intersects the horizontal axis at 0.57 mC and for Cu at -0.37 mC. In order to understand the origin of these offsets we have to consider the current characteristic shown in the inset of Fig. 4.1. When the cathode potential is switched from U_{Co} to the more positive potential U_{Cu}, an anodic transient (also magnified by a factor of 10 in the inset of Fig. 4.1) occurs. This relatively large positive current contribution is found to decay slowly in time, t, approximately proportional to t^{-p} with p a constant ranging between 0.5 and 0.75. The vertical displacement of the d-vs-Q relations can then consistently be explained if the positive current transient is attributed to the dissolution of Co. Immediately at the end of the pulse of duration T_{Co}

the Co-layer thickness is directly proportional to the charge Q_{Co}. Then, however, some Co is dissolved, the amount of which corresponds to a positive charge $Q_a \approx 0.5\,mC$ due to the positive transient visible in the inset of Fig. 4.1. Since the (negative) charge Q_{Cu} transferred during the time interval T_{Cu} is maintained constant, the additional positive charge contribution Q_a tends to increase T_{Cu}. Because the copper current is constant (limited by mass transport), an increased amount of Cu will be deposited. In summary, the presence of the anodic transient Q_a results for fixed predetermined $Q_{Co,Cu}$ in a thinner Co layer and a thicker Cu layer compared to what would be expected in the absence of Q_a.

The anodic transient is thought to be caused by a negatively charged double layer in front of the electrode, which is formed during the Co^{2+} reduction by excess sulfate (SO_4^{2-}) ions. After switching to the Cu-potential U_{Cu}, the Co^{2+} is not yet in equilibrium with the last deposited Co film. The negative near-surface excess charge is compensated i) by dissolution of Co and ii) by diffusion of Co^{2+} ions towards and sulfate ions away from the surface. A more detailed treatment of this effect will be published elsewhere.

Figure 4.2 presents an overview of the structural X-ray diffraction (XRD) analysis of multilayers electroplated in different solutions and on the two different substrates. The compositions are approximately equal with mean layer thicknesses d_{Co}/d_{Cu} of $\approx 1/4\,nm$ for curves (a,b,e) and $\approx 1.5/4\,nm$ for (c,d). Curves (a-c) and (d,e) have been obtained on Cu- and Au-substrates, respectively. Curves (a,d) correspond to multilayers grown in the electrolyte without additives, curves (b,e) with addition of thiourea, and (c) with Triton X-100. Three peak positions have been marked by arrows in Fig. 4.2: the (111) Au-peak and the (111) and (200) peaks of the fcc-Co/Cu multilayer. Three main observations can be made. In the first place, electrodeposited films grown without additives, curves (a,d), are multilayers of high quality as demonstrated by the observation of satellite peaks. Secondly, multilayers grown on (100)-oriented Cu-substrates exhibit only the (200) peak; hence, they are (100) textured. Similarly, multilayers grown on (111)-oriented Au-substrates are (111) textured. Therefore, the multilayers grow with the same crystallographic orientation as the substrates. Finally, the quality of the superlattice is destroyed if a leveling agent is used in the electrolyte (at least for these two examples).

The quality of the superlattice is reflected in the visibility of satellite peaks centered around the main multilayer peak. Without brighteners, we observe satellites up to third order for multilayers (MLs) grown on Cu-substrates (curve a) and first order satellites for (111)-oriented MLs (curve d). If thiourea is added to the electrolyte, the satellite intensity weakens for (111)-oriented MLs (curve e) and almost disappears for (100)-oriented ones (curve b). In case of the additive Triton X-100, the effect is even more dramatic. The main peak shows no satellites and a strong admixture of (111) orientation is observed on the nominally (100)-textured film (curve c). This clearly demonstrates that adding leveling agents can dramatically influence the multilayer growth. For the two additives

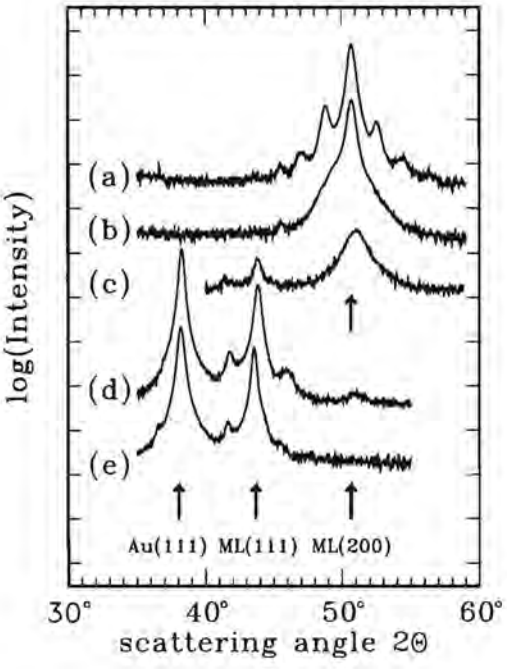

Figure 4.2. *Overview of X-ray diffraction data for multilayers electrodeposited on (100)-oriented Cu-substrates (a-c) and on (111)-oriented Au-substrates (d,e). In the respective plating solutions no brightener was added for curves (a,d), thiourea for (b,e), and Triton X-100 in case of (c). The Au(111) peak position and the positions of the (111) and (200) main multilayer peaks have been marked by arrows.*

investigated here, the superlattice stacking is (partially) destroyed. We would like to mention, that judging from XRD data only, multilayers electrodeposited on Cu-substrates in electrolytes containing no additives are comparable in quality to multilayers fabricated by sputtering, a technique commonly applied for the growth of magnetic multilayers.

From the observed satellite peaks we are able to obtain the multilayer period D_{ML} (see Ref. 20 and section 2.2.1). In addition, the mean Co-layer thickness d_{Co} is derived from measuring the saturation magnetization M_s of the electroplated multilayers and using the bulk-Co value for M_s of 1.79 T. The mean Cu-layer thickness d_{Cu} is then given by $d_{Cu} = D_{ML} - d_{Co}$. Values for the layer thicknesses obtained by this method (XRD&VSM) are in good agreement with the data obtained by XRF analysis presented in Fig. 4.1.

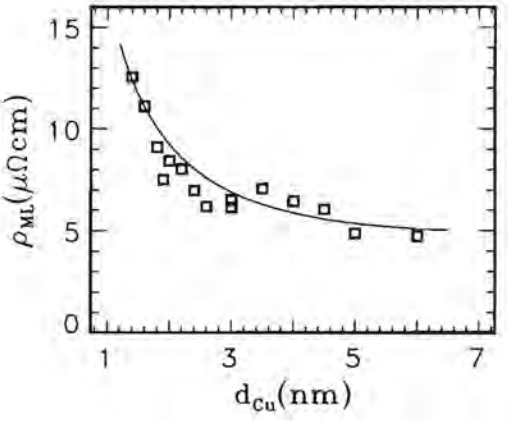

Figure 4.3. *Dependence of the measured resistivity, ρ_{ML}, on the mean Cu-layer thickness for multilayers electroplated on Cu-substrates using an electrolyte without additives (brighteners). The mean Co-layer thickness amounts to 1.35 ± 0.1 nm. The full line is a guide to the eye.*

Figure 4.3 shows the electrical resistivity of multilayers grown on Cu-substrates without additives (no brighteners) for Cu-layer thicknesses varying between $d_{Cu} =$ 1.2 and 6 nm, and a fixed cobalt thickness of $d_{Co} = 1.35 \pm 0.1$ nm. Before the deposition of the multilayer we first determine the sheet resistance, $R_s^{\square}$, of the substrates, which for the series shown in Fig. 4.3 is $R_s^{\square} = 2.6\,\Omega$. After electroplating, the sheet resistance of the multilayer, $R_{ML}^{\square}$, is obtained by measuring the sample sheet-resistance (typically in the range of 0.2-1 Ω) and correcting for the shunting $R_s^{\square}$. The resistivity ρ_{ML} of the ML is now given by $\rho_{ML} = R_{ML}^{\square} N D_{ML}$, where N is the number of multilayer periods.

In Fig. 4.3 the resistivity is seen to decrease with increasing Cu-layer thickness d_{Cu}. This is expected since the relative contribution of Co/Cu-interface scattering decreases and because of the relatively low resistivity of bulk Cu ($1.7\,\mu\Omega$ cm) compared to bulk Co ($5.8\,\mu\Omega$ cm). For large d_{Cu} we asymptotically obtain a resistivity of $5\,\mu\Omega$ cm. For a thin film, this value is rather low, demonstrating the high Cu-layer quality.

In the case of multilayers grown in an electrolyte with thiourea, ρ_{ML} is found to be systematically larger. The observed difference is particularly pronounced for thinner Cu-layers where ρ_{ML} can be two times larger than for multilayers of identical composition but grown without thiourea. We attribute this increased resistivity to additional interface scattering due to thiourea (or products from thiourea) trapped at the interface.

4.1.4 Magnetoresistance measurements

All magnetoresistance (MR) measurements have been carried out at room temperature with the electric current flowing in the plane of the multilayer using the Van der Pauw geometry (Ref. 23 and section 2.2.3). In this way we can easily correct for the sheet resistance of the base layers used for the deposition of the multilayers, as already explained in the discussion of Fig. 4.3. The inset of Fig. 4.4 shows schematically the position of the electric contacts and the orientation of the applied magnetic field $\boldsymbol{H}$, which was always in the plane of the layers. The resistance $R_{12,34}$ is defined as the voltage difference $V_3 - V_4$ per unit current passing from contact 1 to contact 2. From here on we shall denote $R_{12,34}$ as $R_\perp$ and the corresponding MR as $\mathrm{MR}_\perp$, since in this case the current is flowing mainly perpendicularly to the direction of the magnetic field. Analogously, $R_{13,24}$ is denoted as $R_\parallel$ and the MR in this situation as $\mathrm{MR}_\parallel$. By measuring both $R_\perp(H)$ and $R_\parallel(H)$ we can discriminate between the contributions from the giant MR (GMR) effect, and from the anisotropic MR (AMR) effect [75]. In contrast to the AMR effect, which depends on the angle between the current flow and the magnetization, the GMR effect is due to the relative orientations of the magnetic moments in successive magnetic layers and does therefore not depend on the direction of the current flow. To be able to compare the MR data properly, we define the magnetoresistance by the expression $\mathrm{MR}(H) = (R(H) - R_{\mathrm{sat}})/R_{\mathrm{sat}}$, where R_{sat} is the extrapolated resistance value at zero applied magnetic field obtained from the linear slope at high magnetic field. This slope is temperature dependent, increasing at higher temperatures [76]. Taking the resistance at some high magnetic field value as the scaling resistance R_{sat}, as is usually done, can lead to an overestimate of the GMR effect. With our method of effectively subtracting this slope we have overcome this problem.

Figure 4.4 shows the magnetoresistance at room temperature of a multilayer consisting of 50 repeats of Co(1.5 nm)+Cu(1.6 nm) grown on a Cu-substrate. Mainly an anisotropic MR effect is observed with a negligible giant MR contribution. This is typical for all our multilayers with relatively thin Cu spacer layers. The magnitude and sign of this anisotropic MR effect are in good agreement with earlier studies on bulk ferromagnetic 3*d* alloys [75].

In Fig. 4.5 the MR curves of a typical example of a multilayer with larger Cu-layer thickness are shown. The composition is 50×[Co(1.5 nm)+Cu(4.0 nm)] also grown on a Cu-substrate. As compared to Fig. 4.4, the present MR data display an entirely different behavior. Both $\mathrm{MR}_\perp$ and $\mathrm{MR}_\parallel$ have the same sign and are considerably larger ($\approx 10\%$) than the anisotropic MR values seen in these materials. This indicates that here we observe the giant MR effect, although there still remains an anisotropic MR contribution, since $\mathrm{MR}_\parallel < \mathrm{MR}_\perp$. In the remainder of the text the average of $\mathrm{MR}_\perp$ and $\mathrm{MR}_\parallel$ is used as an indication of the giant MR contribution.

We mention that the two MR curves in Fig. 4.5 were measured differently:

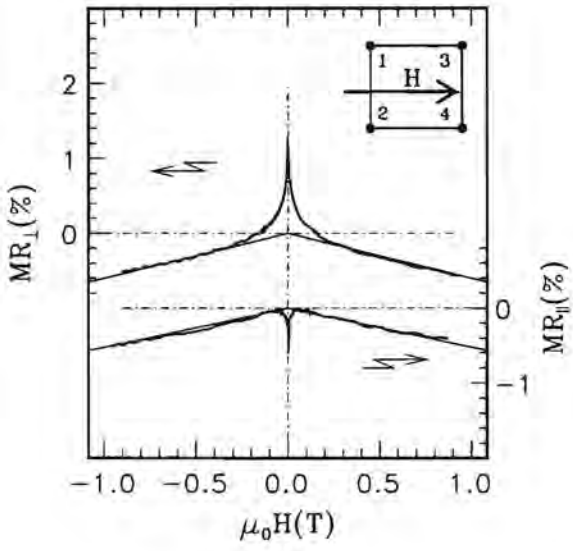

Figure 4.4. *Magnetoresistance (MR) curves at room temperature for a (100)-oriented multilayer 50×[Co(1.5 nm)+Cu(1.6 nm)] grown on a Cu-substrate. The inset shows the position of the electric contacts and the direction of the magnetic field, which was always in the plane of the layers. The "transverse" magnetoresistance, $MR_{\perp}$, and the "longitudinal" magnetoresistance, $MR_{||}$, are defined as $R_{12,34}$ and $R_{13,24}$, respectively.*

$MR_{\perp}$ was obtained while lowering the applied magnetic field from +0.8 to −0.8 T, and $MR_{||}$ while increasing the field back to +0.8 T. The asymmetric shape of the MR curves around $H = 0$ is due to magnetic hysteresis. For this relatively large Cu-layer thickness of 4 nm one is in the so-called uncoupled regime rather than in the regime of antiferromagnetically coupled Co layers, which can be achieved for thinner Cu layers ($d_{Cu} \lesssim 3$ nm) only [77]. In the uncoupled regime the giant MR effect originates from the random orientation of the magnetic domains at the coercive field H_c. The giant MR maxima in Fig. 4.5 are therefore positioned at the fields $\pm H_c$, where the total magnetization is zero.

The absence of significant antiferromagnetic (AF) coupling can also clearly be demonstrated by means of magnetization measurements. In Fig. 4.6 the magnetization behavior of the two multilayers of Figs. 4.4 and 4.5 is shown. The solid and dashed curves correspond to the multilayers with $d_{Cu} = 1.6$ nm (MR of Fig. 4.4) and $d_{Cu} = 4.0$ nm (MR of Fig. 4.5), respectively. In the case of perfect AF coupling between the magnetic layers a very low remanence would have been

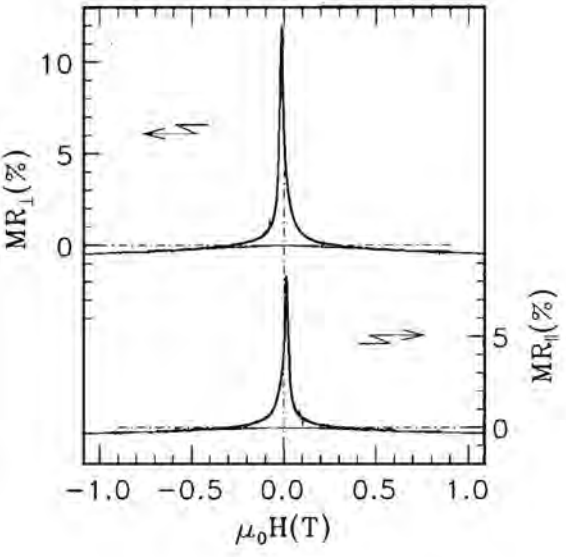

Figure 4.5. *Magnetoresistance (MR) curves at room temperature for a (100)-oriented multilayer 50×[Co(1.5 nm)+Cu(4.0 nm)] grown on a Cu-substrate. The "transverse" magnetoresistance, $MR_{\perp}$, and the "longitudinal" magnetoresistance, $MR_{\parallel}$, are defined in the caption of Fig. 4.4.*

observed due to the antiparallel alignment of the magnetization vectors. This is obviously not true for our multilayers. Instead, high remanence values of 70-80% of saturation are found. In addition, the coercive field H_c increases for multilayers with thicker Cu spacer. These two observations are characteristic for all electrodeposited multilayers and are in agreement with the experiments of Hua *et al.* [62].

The amount of Cu^{2+} and Co^{2+} ions in the solution is of great influence for the quality of the electrodeposited multilayers. A relatively high concentration of Cu^{2+} with respect to Co^{2+} results in the inclusion of an increased amount of Cu impurities into the Co layers. Because of the immiscibility of Cu in Co, this leads to the segregation of small Cu crystallites. For a Cu^{2+} concentration $\gtrsim 10\,\mathrm{mM}$ we observe for thick Co-films a clear separation in Cu- and Co-rich phases. For multilayers, XRD scans indicate the loss of texture and the (partial) suppression of the satellite peak intensity. Furthermore, in images obtained by scanning electron microscopy (SEM), small Cu crystallites are clearly visible. These observations demonstrate that the structural quality is reduced for multilayers plated in an electrolyte containing a large fraction of Cu^{2+}. In the case

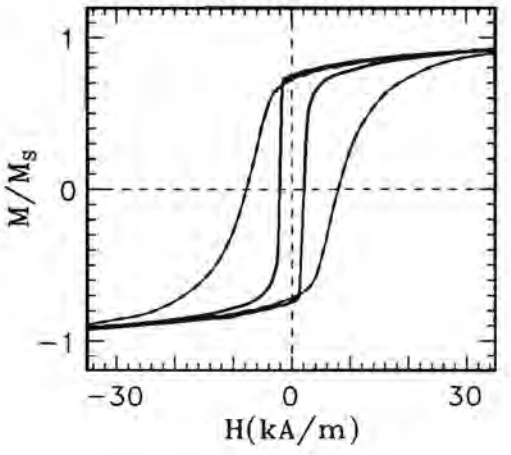

Figure 4.6. *Magnetization loops of two (100)-oriented samples of composition 50×[Co(1.5 nm)+Cu(1.6 nm)] (solid line) and 50×[Co(1.5 nm)+Cu(4.0 nm)] (dashed line) grown on Cu-substrates. The magnetic field was in the plane of the layers. The two curves correspond to the samples for which the magnetoresistance is shown in Figs. 4.4 and 4.5, respectively.*

of a too low Cu^{2+} concentration $\lesssim 2\,mM$, on the other hand, SEM images indicate a tendency for increased surface roughness. In addition, the copper current is so low that the Cu-layer thickness gets increasingly more difficult to control. Typical Cu-growth rates are then as small as 0.1 Å/s. In order to control the small Cu^{2+}-reduction current ($30\,\mu A/cm^2$), the oxygen content in the electrolyte has to be controlled and kept sufficiently small such that the additional cathode current due to the reduction of oxygen can be neglected. Finally, for Cu^{2+} concentrations $\lesssim 1\,mM$, the Cu^{2+}-reduction current becomes of the same order of magnitude as the exchange-current density ($\approx 5\,\mu A/cm^2$) for the equilibrium reaction $Co \rightleftharpoons Co^{2+} + 2e^-$. After the deposition of the Co layer, the Cu growth proceeds so slowly that the simultaneous dissolution of Co has to be taken into account. This definitely increases the interface roughness and, because of the long growing time, appreciable intermixing between Co and Cu may occur. We therefore suspect the MR to be low for small Cu^{2+} concentrations, mainly because of the reduced Co/Cu interface quality, and also low for relatively high Cu^{2+} concentrations, because of phase separation. In Fig. 4.7 we plot the giant MR values versus the Cu^{2+} concentration, c_{Cu}, for multilayers with the composition 50×[Co(1.5 nm)+Cu(5.0 nm)] grown on Au-substrates. An optimum c_{Cu} is found for 3-8 mM. Except for the data of Fig. 4.7, all multilayers were grown

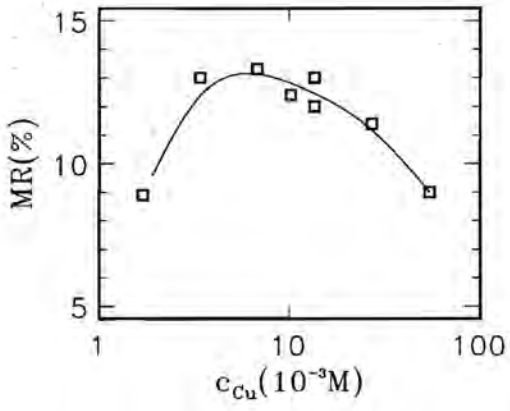

Figure 4.7. *Dependence of the giant magnetoresistance (MR) on the concentration of Cu^{2+} ions, c_{Cu}, in the electrolyte. The concentration of Co^{2+} ions was fixed at 1.2 M. The MR values were measured at room temperature on samples with 50 repeats of [Co(1.5 nm)+Cu(5.0 nm)] grown on Au-substrates. The full line is a guide to the eye.*

with a concentration of 6.8 mM.

The dependence of the giant MR on the spacer layer thickness, d_{Cu}, for two series of Co/Cu(100) and Co/Cu(111) multilayers is shown in Figs. 4.8(a) and 4.8(b), respectively. In both series the magnetic layer thickness, d_{Co}, was kept constant at 1.35 nm. In Fig. 4.8(a) we observe for the (100) orientation a continuous decrease of the giant MR effect above $d_{Cu} \approx 4$ nm. This is in agreement with earlier results on sputtered and MBE-grown multilayers and can be attributed to an increased shunting of the magnetoresistance by the nonmagnetic spacers. We would like to emphasize that the magnitude of the giant MR effect in our electrodeposited Co/Cu samples is comparable to sputtered or MBE-grown samples, which again indicates that electrodeposition is a competitive method for obtaining high quality multilayers. The drop of the giant MR for $d_{Cu} < 4$ nm is less straightforward. The Co/Cu system is known to exhibit antiferromagnetic coupling peaks around $d_{Cu} \approx 2$ nm and $d_{Cu} \approx 3$ nm, which are accompanied by maxima in the giant MR (see, for instance, Ref. 77 and the next section). These maxima are not observed in our (100)-oriented samples. This appears to be a general trend in electrodeposited multilayers, although Hua *et al.* [62] have found evidence for a weak AF coupling peak in the Co-Ni/Cu system. The absence of a strong maximum in the giant MR below $d_{Cu} = 4$ nm is believed to be the result of ferromagnetic pinholes, which tend to couple neighboring magnetic layers

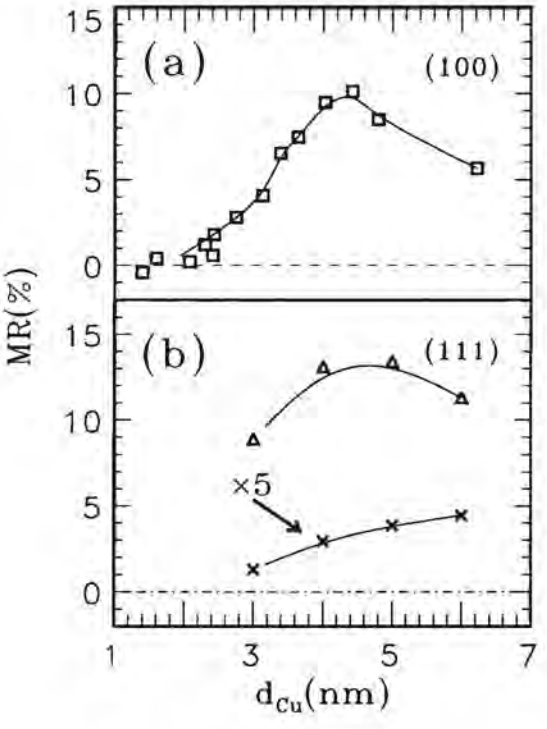

Figure 4.8. *Dependence of the giant magnetoresistance (MR) at room temperature on the thickness of the Cu spacer layer, d_{Cu}, for (a) (100)-oriented Co/Cu multilayers grown on Cu-substrates, and (b) (111)-oriented Co/Cu multilayers grown on Au-substrates. The magnetic layers had a thickness of 1.3 nm and the number of repeats was 50. The crosses in the bottom curve of (b) represent data of samples which were electrodeposited with thiourea added to the electrolyte. Note that these values have been multiplied by a factor of five. The full lines are guides to the eye.*

ferromagnetically.

Figure 4.8(b) contains two data sets of (111)-oriented Co/Cu multilayers. The samples represented by triangles have been prepared in a similar way as the multilayers shown in Fig. 4.8(a) and their magnetoresistance shows the same general behavior with slightly higher giant MR values up to 14% at $d_{Cu} \approx 4$ nm. The bottom curve (crosses) in Fig. 4.8(b) represents giant MR data of (111)-oriented samples grown in an electrolyte containing the brightener thiourea. The MR values of these samples are reduced by at least an order of magnitude (note that

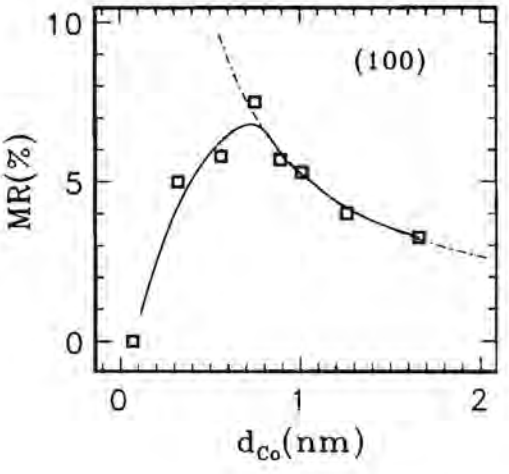

Figure 4.9. *Dependence of the giant magnetoresistance (MR) at room temperature on the magnetic Co layer thickness, d_{Co}, for (100)-oriented Co/Cu multilayers grown on Cu-substrates. The Cu spacer layer thickness was fixed at 4 nm and the number of repeats was 50. The full and dashed-dotted lines are guides to the eye.*

the MR values of the bottom curve in Fig. 4.8(b) have been multiplied by five). This observation is in agreement with the XRD data in Fig. 4.2: the addition of brighteners not only destroys the quality of the multilayer stacking, but also destroys the MR effect! Because of the detection of sulfur (thiourea contains sulfur) as impurity in XRF analysis for samples grown in electrolytes containing thiourea, we think that parts of the brightener are incorporated at the interfaces as additional defects, increasing the rate of spin independent scattering. This is supported by the observation of systematically higher resistivities of samples grown with thiourea. The same influence was found for the other brightener, Triton X-100, which was used by the group of Lashmore *et al.* [73]. To summarize, the results in Fig. 4.8 demonstrate that large MR values are achievable for electroplated multilayers grown in either the (100) or the (111) direction, provided no brightener is added to the electrolyte and the Cu-layer thickness is chosen large enough (regime of uncoupled magnetic layers).

In order to characterize the quality of the Co layers, the dependence of the giant MR on the magnetic layer thickness was studied. Figure 4.9 shows the results of the (100)-oriented Co/Cu multilayers with $d_{Cu} = 4\,\text{nm}$. A maximum in the magnetoresistance is found at a Co thickness of $\approx 0.7\,\text{nm}$. An increase of the MR with decreasing magnetic layer thickness is characteristic for the situation

in which spin-dependent interface scattering is the main cause for the giant MR effect rather than spin dependent scattering within the magnetic layers themselves (Ref. 77 and section 4.2). The drop in MR below $d_{Co} = 0.7\,nm$ is likely to be a structural effect: the Co layers get so thin (2-3 monolayers) that continuous layers cannot be formed any longer. In this Co thickness regime it may be possible to observe the onset of superparamagnetic behavior as has also been found, for instance, in Co/Ag multilayers [78]. As a first indication we indeed see a large drop of both the coercive field and the remanence for samples with $d_{Co} < 0.7\,nm$, but a more detailed study including the temperature dependence has not yet been performed.

One remark has to be made at this point. Although the qualitative trends reproduce remarkably well from one set of samples to another, the absolute MR values of Figs. 4.8(a) and 4.9 differ systematically by a factor of two. As already noted at the end of section 4.1.2, this is probably due to the initial state of the substrate. For the (100)-oriented samples this is Si(100)+20 nm Cu stored under ambient conditions. Before electrodepositing the actual multilayer, the formed copper-oxide layer is removed by dipping the substrate into a H_2SO_4 solution, but differences in the initial roughness after this cleaning process may still occur. This effect is less important for the (111)-oriented samples grown on Au-substrates. There, the variations in MR values between different sets of multilayers are much smaller.

4.1.5 Conclusions and summary

Co/Cu multilayers have been grown on Si substrates, coated with either Cu(100) or Au(111) base layers, by means of electrodeposition in an electrolyte containing both Co^{2+} and Cu^{2+} ions. The multilayers are highly textured in either the (100) or (111) crystallographic direction depending on the substrate base-layer. The sharp and clear satellite peaks observed in X-ray diffraction scans demonstrate that a high quality superlattice can be obtained. Using X-ray fluorescence analysis, layer thicknesses have carefully been calibrated. Typical resistivities of 5-10 $\mu\Omega\,cm$ are comparable to sputtered or MBE-grown multilayers. For both growth orientations the anisotropic MR effect dominates for Cu-spacer-layer thicknesses below 2.5 nm, in contrast to multilayers with thicker spacer layers in which a giant MR-effect up to 14% has been measured at room temperature. No evidence for antiferromagnetic coupling is found. We have demonstrated that the correct choice of Cu^{2+} concentration is crucial for obtaining a large magnetoresistance and high quality Co layers and Co/Cu interfaces. The addition of commonly used brighteners to the electrolyte has a catastrophic effect on both the structural quality of the multilayers, as evidenced by XRD patterns, as well as on the magnitude of the magnetoresistance. The dependence of the giant MR on the magnetic layer thickness, d_{Co}, confirms the idea that the Co/Cu interfaces are the main sources for spin dependent scattering. Indications have been

observed for the onset of superparamagnetic behavior for $d_{Co} < 0.7\,nm$.

4.2 Sputtered Co/Cu Multilayers*

In this section we present magnetoresistance measurements on high-vacuum-sputtered Co/Cu(100) multilayers grown on Cu buffer layers. The magnetoresistance in the first antiferromagnetic- (AF-) coupling peak is very sensitive to the buffer layer thickness. We find a linear dependence between the actual measured magnetoresistance and the fraction of AF coupling, as determined by magnetization measurements. We compare our Co/Cu(100) magnetoresistance data at 4 K of completely antiparallel-aligned multilayers with the quantum model of giant magnetoresistance of Levy, Zhang, and Fert. This reveals evidence for strong spin-dependent interface scattering, whereas the spin dependence of the bulk scattering in Co is small.

4.2.1 Introduction

The giant magnetoresistance (MR) effect in magnetic multilayers has been the subject of numerous studies in recent years (see, for instance, Refs. 79–81 and references therein). On the basis of the giant MR effect, there is a spin dependence of the electron scattering processes, but whether this spin-dependent scattering takes place within the interior of the magnetic layers or at the interfaces between magnetic and nonmagnetic materials still remains a matter of dispute. Since Camley and Barnaś originally introduced their semiclassical MR model based on the spin-dependent Boltzmann equation [28], it has been widely applied in modified forms to several multilayer and spin-valve systems [30–35, 82]. The semiclassical approach gives good qualitative results and, moreover, a quantitative agreement with the experimental data can also be obtained in terms of model parameters [83]. An essential drawback, however, is the different treatment of the bulk and interface contributions to the resistivity. Levy, Zhang, and Fert on the other hand developed a quantum model of the MR, which describes both bulk and interface scattering on equal footing (see Refs. 37, 38 and section 3.3.1). This model was used to explain the giant MR of the Fe/Cr system [84, 85], which is a good model system, since due to the large AF-coupling strength, completely antiparallel alignments at zero applied field can be realized relatively easily up to Cr spacer layer thicknesses of 2.8 nm, corresponding to the second AF-coupling maximum. For the Fe/Cr case it was concluded that the spin-dependent scattering processes are primarily of interfacial nature. In the case of Co/Cu multilayers such a comparison is more difficult, because the much weaker AF-coupling strength easily causes an imperfect antiparallel alignment already in the first AF-coupling peak and certainly in the second peak,

* Apart from small changes, this section has been published in Phys. Rev. B **50**, 9982 (1994).

thereby reducing the measured MR value and leading to data inappropriate for comparison with the model.

In this section we present MR measurements on Co/Cu(100) multilayers grown by sputtering techniques. This system is known to exhibit large MR values and can be grown coherently in a rather easy way [86, 87]. The influence of the Cu buffer layer thickness, t_b, deposited prior to the multilayer to obtain a well defined (100) growth, on the fraction of AF coupling is discussed. We find that t_b has a large influence on that fraction, especially for Cu spacer layer thicknesses corresponding to the first AF-coupling peak. Measured MR values are directly proportional to the AF coupled fraction in the multilayers. Extrapolating our MR data to a completely antiparallel alignment, we can make a reliable comparison of the MR of Co/Cu(100) at 4 K with the quantum model of Levy, Zhang, and Fert (Refs. 37, 38 and section 3.3.1).

4.2.2 Sample preparation and characterization

The multilayer samples were grown by high-vacuum magnetron sputtering. The base pressure of the system prior to deposition was 4×10^{-7} Torr and the Ar pressure during the sputtering was 7×10^{-3} Torr. The samples were deposited at a rate of 4 Å/s onto $4 \times 12\,\mathrm{mm}^2$ Si(100) substrates held at room temperature. Before sputtering, the samples were *ex-situ* cleaned by a HF dip and *in-situ* by a 30-min glow-discharge treatment. In order to obtain a highly face centered cubic (fcc) (100)-oriented texture, we used Cu buffer layers with thicknesses t_b of 200 and 300 Å. For values of t_b below 200 Å we get a mixed (111)-(100) growth. After deposition of the multilayers, they were covered with a 50 Å Au protection layer. The (100) orientation was checked by X-ray diffraction (XRD) measurements using Cu-$K\alpha$ radiation. Figure 4.10 shows a typical high-angle XRD pattern for the superlattice 100×[Co(16 Å)+Cu(10.5 Å)] grown on top of a 200 Å Cu buffer layer.

We observe the main Co/Cu(200) Bragg reflection with several multilayer satellite peaks, very similar to earlier results of Coehoorn *et al.* [88]. There is almost no intensity of Co/Cu(111) reflections present. From the full width at half maximum (FWHM) of the Co/Cu(200) reflection, which is 0.39°, we deduce a perpendicular crystal coherence length of about 240 Å. This value is nearly the same for all our (100)-oriented multilayers. The FWHM of the rocking curves about the (200) maximum (not shown) varied between 1.5° and 2.0°, indicating the good texture of the crystallites.

4.2.3 Magnetoresistance and magnetization measurements

Typical magnetoresistance curves for two samples grown on a 200 Å Cu buffer layer and with Cu spacer layer thicknesses t_{Cu} of 10.5 and 20 Å are shown in Figs. 4.11(a) and 4.11(b), respectively. We define MR as $(R_{max} - R_{sat})/R_{sat}$,

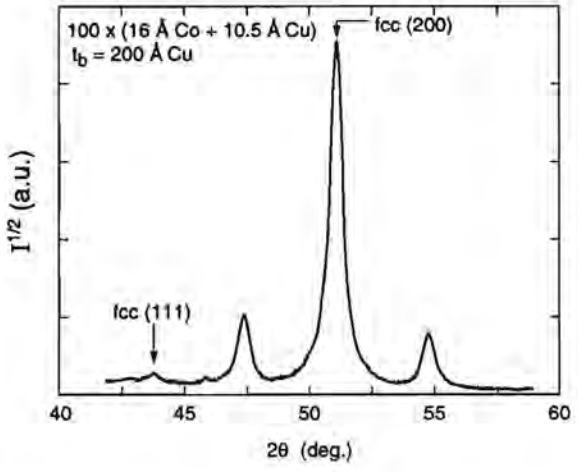

Figure 4.10. *High-angle X-ray diffraction pattern of a 100×[Co(16 Å)+ Cu(10.5 Å)] multilayer grown on a 200 Å Cu buffer layer.*

with R_{max} the maximum resistance around zero field and R_{sat} the value at saturation. High MR values at room temperature are found of 48% (83% at 4 K) for the multilayer with $t_{Cu} = 10.5$ Å and 40% (75% at 4 K) for the multilayer with $t_{Cu} = 20$ Å. The characteristic form of these curves is a consequence of the fact that the magnetic field was applied along a hard magnetization axis, as we will discuss further in more detail in relation to the magnetization experiments. Figure 4.12 depicts the magnetoresistance at room temperature as a function of t_{Cu} for a series of multilayers on 200 and 300 Å Cu buffer layers. One can observe an oscillatory behavior with a period of about 10 Å, which can be associated with maxima in the AF interlayer exchange coupling in this system (see, for instance, Refs. 88–91). Note, however, that the first AF peak around $t_{Cu} = 10$ Å is nearly absent for multilayers grown on a 300 Å thick buffer layer. Similar results were found by Giron *et al.* [92] and they attributed this phenomenon to the roughness of the multilayers and pinholes causing effective ferromagnetic coupling. Because of the relative importance of the roughness compared to t_{Cu}, this effect is more important for the first than for the second AF peak. Apparently, there is a critical maximum value for the buffer layer thickness, since for Fe/Cr multilayers, interface roughness has also been found to increase cumulatively with increasing number of layers [93, 94]. To support this idea, we show in Figs. 4.13(a)-(b) atomic force microscopy (AFM) pictures of the surface roughness of samples consisting of a limited number (four) of [Co(16 Å)+Cu(10 Å)] bilayers grown on a

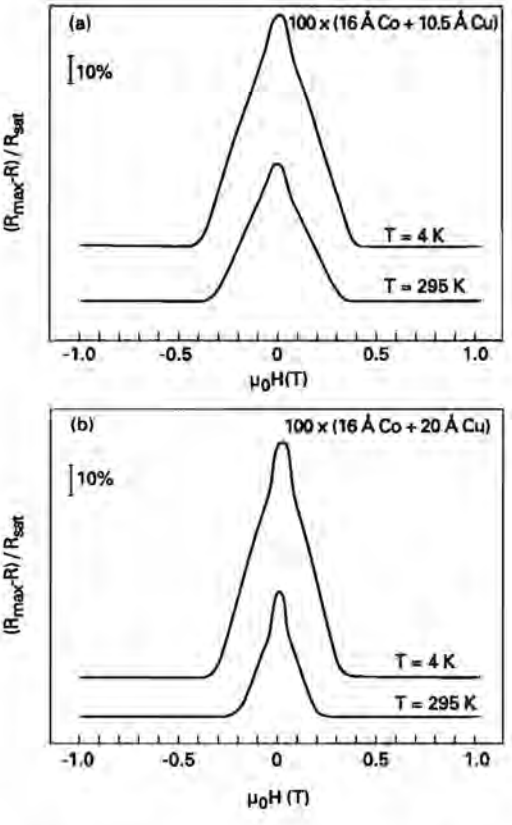

Figure 4.11. *Magnetoresistance curves at room temperature and 4 K for (100)-oriented samples (a) 100×[Co(16 Å)+Cu(10.5 Å)] and (b) 100× [Co(16 Å)+Cu(20 Å)] grown on a 200 Å Cu buffer layer. The magnetic field was along a cubic hard magnetization axis.*

200 and 300 Å thick Cu buffer layer, respectively. We find that the sample on a 200 Å Cu buffer layer [Fig. 4.13(a)], with a mean roughness of about 5 Å, is substantially smoother than the sample on a 300 Å Cu buffer layer, with a mean roughness of about 12 Å [Fig. 4.13(b)]. A noticeable difference in surface roughness, although smaller, could already be observed in single Cu layers of 200 and 300 Å. So, we indeed have evidence that the initially larger surface roughness of a 300 Å Cu base layer leads to relatively rougher multilayers grown on top.

The large difference in MR value found in the first AF peak for the two series of multilayers grown on a 200 and 300 Å thick Cu buffer layer cannot be,

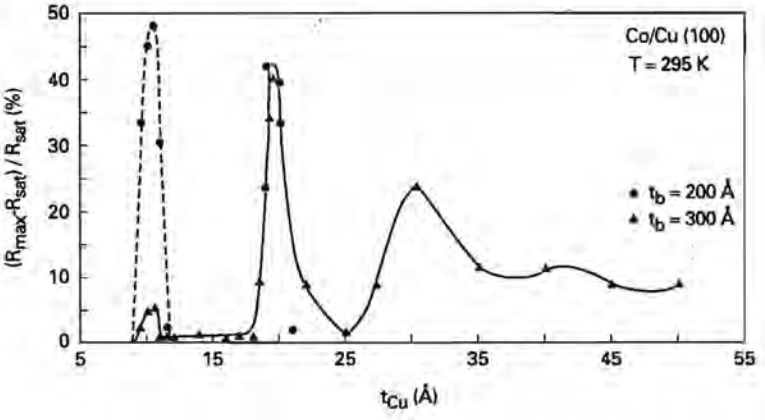

Figure 4.12. *Dependence of the MR ratio at room temperature on the Cu spacer layer thickness t_{Cu} for (100)-oriented 100×[Co(16 Å)+Cu(t_{Cu} Å)] multilayers grown on (●) 200 Å and (▲) 300 Å Cu buffer layers. The solid and dashed lines are guides to the eye.*

as mentioned above, a structural effect in the sense that growth orientation or multilayer periods differ largely for both series, since no evidence for that was found in the XRD data. Shunting effects in the buffer and protection layers can also be excluded considering the magnitude of the MR difference. In order to investigate whether a difference in electronic properties may account for the difference in MR values, such as for instance the ratio $\alpha = \lambda_\uparrow/\lambda_\downarrow$, where $\lambda_\uparrow$ and $\lambda_\downarrow$ are the elastic scattering lengths for spin-up and spin-down electrons, respectively, we measured the temperature dependence of the MR for identical samples grown on a different buffer layer thickness (both samples correspond to the maximum of the first AF-coupling peak). In that case one would expect a much smaller temperature dependence for the series on $t_b = 300$ Å exhibiting the low MR values. Figure 4.14 shows the normalized temperature dependence of the MR for both samples. We obtain an identical behavior, where the MR reaches a value of 83% at 4 K for the multilayer grown on a 200 Å Cu buffer layer and only 8.6% for the multilayer on a 300 Å Cu buffer layer. This identical temperature dependence again suggests that electronic spin-dependent scattering processes are not essentially different and that it is just the fraction of AF coupling that determines the actual value of the MR, similar to the case of (111)-oriented [95] and mixed (100)-(110)-oriented Co/Cu superlattices grown on a variety of buffer layers and under various conditions [96, 97].

We determined the AF coupling behavior by means of magnetization mea-

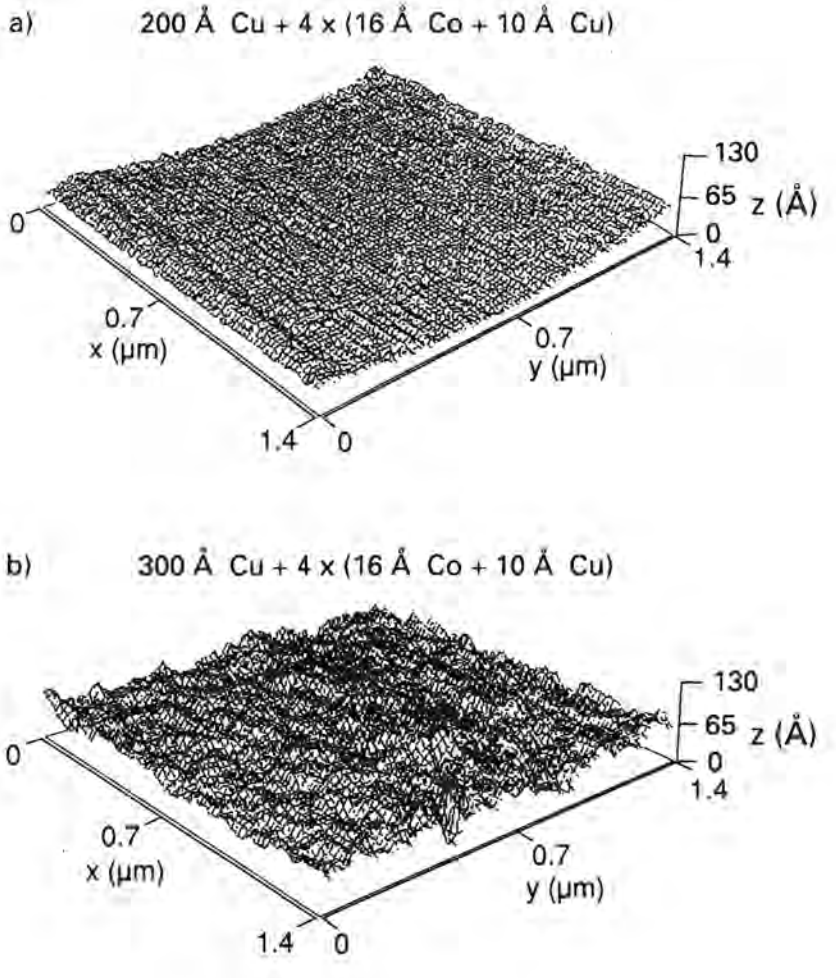

Figure 4.13. *Atomic force microscopy (AFM) pictures of 4×[Co(16 Å)+ Cu(10 Å)] samples grown on (a) 200 Å Cu and (b) 300 Å Cu. The x and y directions are in the plane of the layers, whereas in the z direction the surface roughness is shown. For the sample grown on a 200 Å Cu buffer layer the typical roughness is about 5 Å and for the sample on a 300 Å Cu buffer layer it is about 12 Å.*

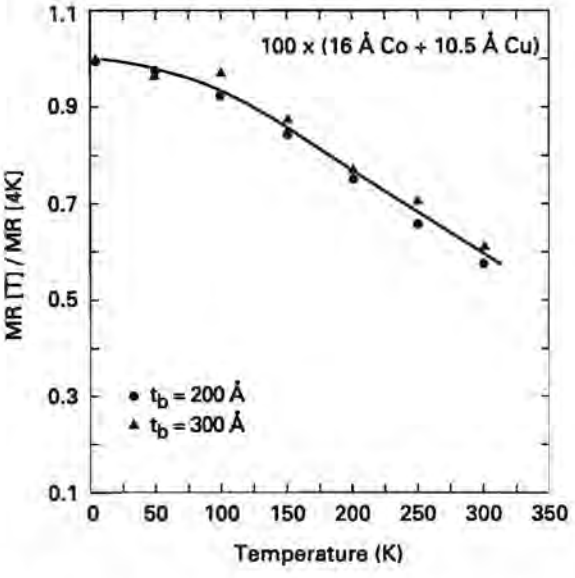

Figure 4.14. *Temperature dependence of the MR for (100)-oriented 100× [Co(16 Å)+Cu(10.5 Å)] multilayers grown on a (●) 200 Å and (▲) 300 Å Cu buffer layer. Both samples correspond to the maximum of the first AF-coupling peak. For the sample on a 200 Å Cu buffer layer, the MR value at 4 K reaches 83%; for the sample on a 300 Å Cu buffer layer the MR is only 8.6% at 4 K.*

surements using a vibrating sample magnetometer (VSM). The magnetic field H was always in the plane of the layers. All our samples had a cubic fourfold in-plane anisotropy with the easy magnetization axis along the crystallographic [011] axis and the hard axis for magnetization along the crystallographic [001] axis. When H is applied parallel to the easy [011] direction, the fraction of AF coupling is defined by $1 - M_r/M_s$, with M_r the remanence at zero field and M_s the saturation magnetization. Figure 4.15 displays the magnetic hysteresis loops at room temperature of the samples with $t_{Cu} = 10.5$ Å on a 200 and 300 Å Cu buffer layer, corresponding to the first AF-coupling maximum. The sample on the 300 Å Cu buffer layer clearly shows a large M_r, indicative for a large ferromagnetic coupling fraction, whereas the situation for the other sample is just opposite.

In order to extract values for the AF-coupling strength J_{AF} and the cubic magnetocrystalline anisotropy constant K_1 from the magnetization measurements, we

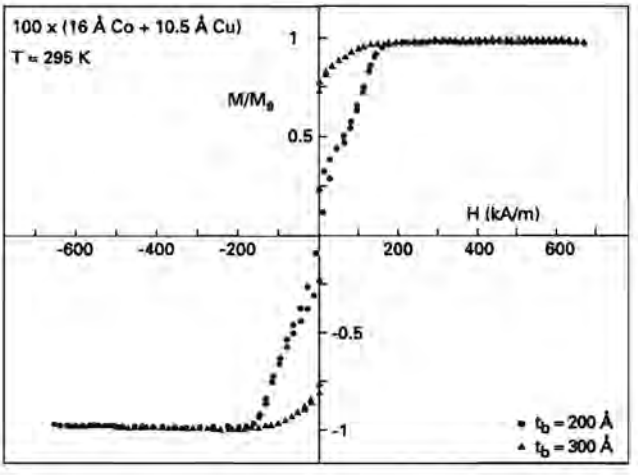

Figure 4.15. *Magnetic hysteresis loops of (100)-oriented 100×[Co(16 Å)+ Cu(10.5 Å)] multilayers grown on a (●) 200 Å and (▲) 300 Å Cu buffer layer. Both samples correspond to the maximum of the first AF-coupling peak. The magnetic field, H, is applied parallel to the easy [011] direction.*

used the expression

$$J_{AF} = \frac{\mu_0 (H_s - H^*) M_s t_{Co}}{4}, \tag{4.1}$$

which has been derived from absolute minimum energy calculations [98–100]. Here, H_s denotes the saturation field along the hard [001] direction and $H^* = 2 K_1/\mu_0 M_s$. Determination of H^* from the saturation field of ferromagnetically coupled samples with adjacent t_{Cu}, yielded an anisotropy constant $K_1 = -8 \times 10^4$ J/m^3, independent of t_{Cu}. This value was confirmed by ferromagnetic resonance measurements. The remanence of those samples was close to the expected value of $\frac{1}{2}\sqrt{2}\, M_s$, assuming coherent rotation from the [001] hard axis at saturation to the [011] easy axis at zero field. With the use of Eq. (4.1) we deduce a maximum coupling strength at room temperature in the first AF peak of J_{AF}(first peak) = 0.15 mJ/m^2 and for the second AF peak J_{AF}(second peak) = 0.068 mJ/m^2. The value of J_{AF} in the first AF-coupling peak is half the value reported by Coehoorn *et al.* [88], but in their analysis they neglected the in-plane anisotropy, although its influence seems to be too small to explain the total difference [101]. The decay in coupling strength from the first to the second AF peak is of similar magnitude as found for molecular-beam-epitaxy- (MBE-) grown wedge-shaped Co/Cu(100) samples [91], but our absolute values are less by a factor 2.5.

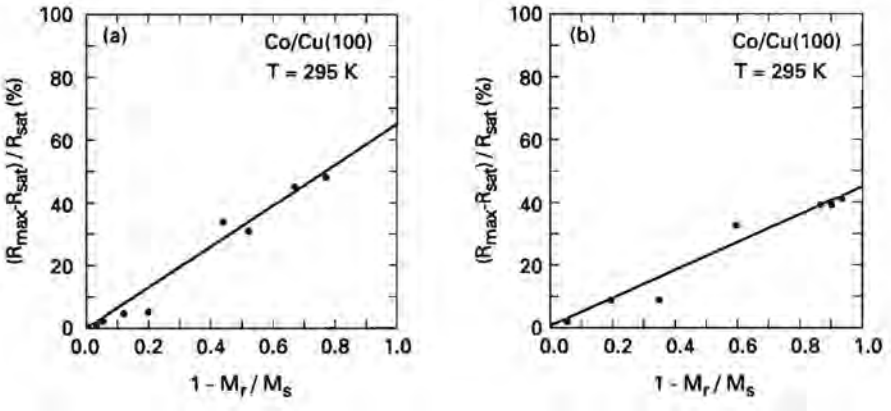

Figure 4.16. *Room temperature magnetoresistance versus* $(1 - M_r/M_s)$ *for (100)-oriented* $100\times$*[Co(16 Å)+Cu(t_{Cu} Å)] multilayers with (a)* t_{Cu} *around the first AF-coupling peak and (b)* t_{Cu} *around the second AF-coupling peak.*

In Fig. 4.16(a) we plot for all our samples with t_{Cu} around 10 Å (samples in the first AF-coupling peak) the MR versus $(1 - M_r/M_s)$. The linear relationship between the MR ratio and the fraction AF coupling allows extrapolation to a completely antiparallel alignment. Doing so yields for the first AF-coupling peak a maximum MR value of 65% at room temperature (108% at 4 K), which is about the same number as found by Parkin *et al.* for Co/Cu(111) multilayers [102, 103]. For the second AF-coupling peak, with $t_{Cu} \approx 20$ Å, we find that the MR values are much less sensitive to the thickness of the Cu buffer layer, because the second AF-coupling peak is somewhat broader and the thicker Cu spacer layer prevents the formation of pinholes. This has already been illustrated in Fig. 4.12, where both samples on a 200 and 300 Å Cu buffer layer exhibit large MR values up to 42%, for t_{Cu} ranging from 18 to 22 Å. In the way described above, we again find a linear dependence of the MR on the fraction of AF coupling [see Fig. 4.16(b)] and an extrapolated MR value of 46% at room temperature (87% at 4 K) in the limiting case of complete antiparallel alignment.

4.2.4 Comparison with the magnetoresistance model based on the Kubo formalism

In this paragraph we calculate the magnetoresistance using Eqs. (3.23)-(3.25) given in section 3.3.1. For the prefactor $ne^2/\hbar k_F$ we used $2 \times 10^{15}\,(\Omega\,\mathrm{m}^2)^{-1}$, which is the mean value of Co and Cu in the free-electron model. We will only compare our low-temperature MR values with the quantum model, since in Eq. (3.23) it

is assumed that the two spin channels are independent, which may no longer be true at elevated temperatures, due to spin mixing.

In Fig. 4.17(a) we plot our experimental MR data as a function of the Cu spacer layer thickness at 4 K in the first two AF-coupling peaks. The top point of each peak now represents the MR value of a 100% antiparallel aligned sample, as determined from the analysis shown in Fig. 4.16. In this way, the theoretical expressions (3.23)-(3.25) can be used for comparison of these maxima. Since the theory describes the case of complete antiparallel alignment, it only reproduces correctly the extrapolated MR values in the first and second AF-coupling peak and not the oscillatory behavior (dashed line). The solid line in Fig. 4.17(a) is a calculation using the quantum model of MR with the parameters: $p_i = 0.64$, $p_l^{Co} = 0.23$, $p_l^{Cu} = 0$ (as Cu is a nonferromagnetic metal), $\lambda_l^{Co} = 20$ Å, $\lambda_l^{Cu} = 250$ Å and $\lambda' = 2.0$. Figure 4.17(b) depicts another set of MR data at 4 K, in which the Cu spacer layer thickness t_{Cu} was fixed at 20 Å (second AF peak) and the magnetic layer thickness t_{Co} was varied. In that way, we are able to discriminate between interface and bulk-Co contributions to the spin-dependent scattering. Since these multilayer samples correspond to the second AF maximum, they all show large AF-coupling fractions of 0.8-0.9. The data plotted in Fig. 4.17(b) are corrected for complete AF coupling, just as it was the case for the data in Fig. 4.17(a). Again, the solid line is a calculation using the quantum model of MR, with essentially the same parameters* as in the calculations of Fig. 4.17(a): $p_i = 0.64$, $p_l^{Co} = 0.23$, $p_l^{Cu} = 0$, $\lambda_l^{Co} = 16$ Å, $\lambda_l^{Cu} = 210$ Å and $\lambda' = 2.0$.

Let us now discuss the significance of the various fitting parameters. It follows that reasonable fits that describe both the data in Figs. 4.17(a) and (b) simultaneously, can only be obtained for $p_i = 0.64 \pm 0.02$ ($\alpha_i = 21 \pm 3$) and $p_l^{Co} = 0.23 \pm 0.03$ ($\alpha^{Co} = 2.6 \pm 0.3$). This value for the bulk asymmetry parameter in Co agrees well with the results of Zhang and Levy [104], and also with those of Pratt *et al.* [47,105], obtained from the analysis of MR measurements of several Co-based multilayer systems with the current perpendicular to the multilayer planes. Hence, it seems to be an intrinsic property of bulk Co. The Co/Cu-interface asymmetry parameter p_i (α_i), however, is rather large compared to the results of Pratt *et al.* [47,105] for sputtered Co/Cu(111) multilayers ($\alpha_i = 6.1 \pm 1.5$). Zhang and Levy [104] also find a considerably smaller value of $\alpha_i \approx 10$. So, this suggests that p_i (α_i) is more dependent on the exact microstructure, orientation, and deposition conditions. For our samples, the large value for α_i is mainly the origin of the large MR values in the first and second AF-coupling peak. The length λ_l^{Cu} is the dominant cause for the decrease in MR when going from the first to the second AF-coupling peak [see Fig. 4.17(a)] and

* The small difference in the parameters λ_l^{Co} and λ_l^{Cu} may be due to the different number of repeats, n, used in the two data series [$n = 100$ for the series in Fig. 4.17(a) and $n = 50$ for the series in Fig. 4.17(b)], which influences the relative contributions of the Cu buffer layer to the MR.

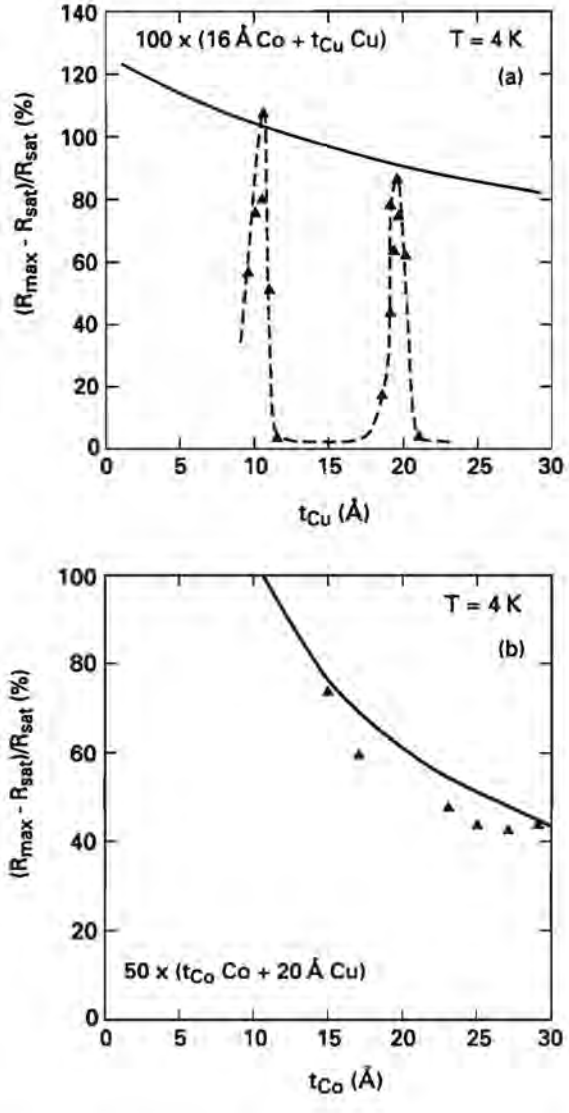

Figure 4.17. *(a) Dependence of the magnetoresistance on the Cu spacer layer thickness t_{Cu} at T=4 K. The solid line is calculated using the quantum model of Levy et al. (Refs. 37,38 and section 3.3.1); the dashed curve is a guide to the eye. (b) Dependence of the magnetoresistance on the magnetic layer thickness t_{Co} at T=4 K. The solid line is a calculation with the quantum model. Fitting parameters are given in the text.*

must be in the range 210 Å$< \lambda_I^{Cu} <$ 250 Å. This result agrees with the large values of λ_I^{Cu} reported in the literature. The length λ_I^{Co}, on the other hand, is mainly responsible for the decrease of the MR with increasing t_{Co} [see Fig. 4.17(b)]; it is found to be within the range 16 Å$< \lambda_I^{Co} <$ 20 Å. The parameter λ', determining the scattering length for interface scattering, can be varied between 1.8 and 2.2, without really worsening the fits. With these fitting parameters we obtain for the first and second AF-coupling peak (t_{Co} = 16 Å) typical multilayer resistivities ρ_{AF} of 77 and 61 $\mu\Omega$ cm, respectively. These are about a factor three larger than experimentally determined resistivities, which may be due to the value of the prefactor in Eq. (3.23), which was taken from the free electron model. The same discrepancy was also found in the case of Fe/Cr multilayers [37, 38, 84, 85]. Our main conclusion is that large spin-dependent interface scattering is absolutely necessary to explain the giant MR effect in Co/Cu, and that the contribution from the spin-dependent bulk scattering is small. This is in accordance with the findings of Parkin, that the giant MR effect is determined by the character of the ferromagnetic/nonmagnetic interfaces [106].

4.2.5 Summary

We have grown sputtered Co/Cu(100) multilayers on Cu buffer layers with different thicknesses. We found that the measured MR value for the first AF-coupling peak is very sensitive to the thickness of the Cu buffer layer, whereas it is not for the second AF peak. This is attributed to the relative importance of interface roughness in combination with the width of the AF-coupling maxima. Furthermore, we have observed a linear relationship between the actual measured MR ratio and the fraction of AF coupling, with maximum MR values at room temperature for the first and second AF peak of 65% and 46%, respectively (108% and 87%, respectively, at 4 K). These values were interpreted with the quantum model of magnetoresistance of Levy, Zhang, and Fert (Refs. 37, 38 and section 3.3.1), from which we found evidence that spin-dependent scattering at the Co/Cu interfaces is the main cause for the giant MR effect.

4.3 Sputtered NiFe/Cu Multilayers*

Here we present magnetoresistance (MR) data of high-vacuum magnetron sputtered NiFe/Cu multilayers (NiFe=$Ni_{80}Fe_{20}$=Permalloy) grown on Si(100) substrates with a Cu buffer layer and compare these with earlier results on Co/Cu(100) multilayers (see Ref. 77 and the previous section). Measured MR values are directly proportional to the antiferromagnetically coupled fraction in the multilayers. Extrapolating to a completely antiparallel alignment, we can make a reliable comparison of the MR with the magnetoresistance model of Levy, Zhang, and

* Presented at the MRS Spring Meeting, San Francisco, April 17-21, 1995.

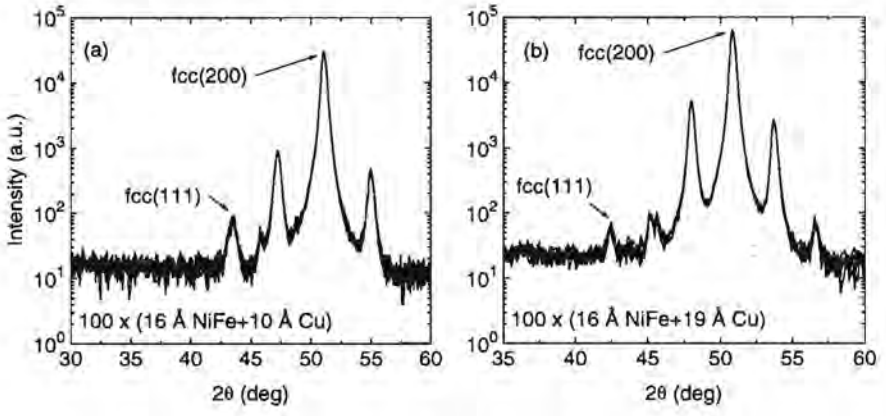

Figure 4.18. *High-angle X-ray diffraction patterns of (a) a 100× [NiFe(16 Å)+Cu(10 Å)] multilayer and (b) a 100×[NiFe(16 Å)+Cu(19 Å)] multilayer. Both samples were grown on Cu buffer layers of 200 Å.*

Fert [37, 38] (see also section 3.3.1). For the NiFe/Cu multilayers, the deduced spin-asymmetry parameters are $\alpha_i^{\mathrm{NiFe/Cu}} = 5.0 \pm 0.4$ and $\alpha_b^{\mathrm{NiFe}} = 2.1 \pm 0.3$ for interface and bulk scattering, respectively. Although much smaller than in our Co/Cu multilayers, where $\alpha_i^{\mathrm{Co/Cu}} = 21 \pm 3$ and $\alpha_b^{\mathrm{Co}} = 2.6 \pm 0.3$, it is still the spin dependence of the interface scattering that is the main cause for the large MR values.

4.3.1 Sample fabrication and characterization

The multilayer samples were grown by high-vacuum magnetron sputtering. The base pressure of the system prior to the deposition was 4×10^{-7} Torr and the Ar pressure during sputtering was 7×10^{-3} Torr. The samples were deposited at a rate of 2-4 Å/s onto $4 \times 12\,\mathrm{mm}^2$ Si(100) substrates held at room temperature. Before sputtering, the samples were *ex-situ* cleaned by a HF-dip and *in-situ* by a 30 min glow-discharge treatment. In order to obtain a highly face centered cubic (fcc) (100)-oriented texture, we used a Cu buffer layer with a thickness, t_b, of 200 Å. For values of t_b below 200 Å we get a mixed (111)-(100) growth. After deposition of the multilayers, they were covered with a 50 Å Au protection layer. The (100) orientation was checked by X-ray diffraction (XRD) measurements using Cu-$K\alpha$ radiation. Figures 4.18(a) and 4.18(b) show typical high-angle XRD patterns for the superlattices 100×[NiFe(16 Å)+Cu(10 Å)] and 100×[NiFe(16 Å)+Cu(19 Å)], respectively. In both cases we observe the main NiFe/Cu(200) Bragg reflection with several multilayer satellite peaks. There is

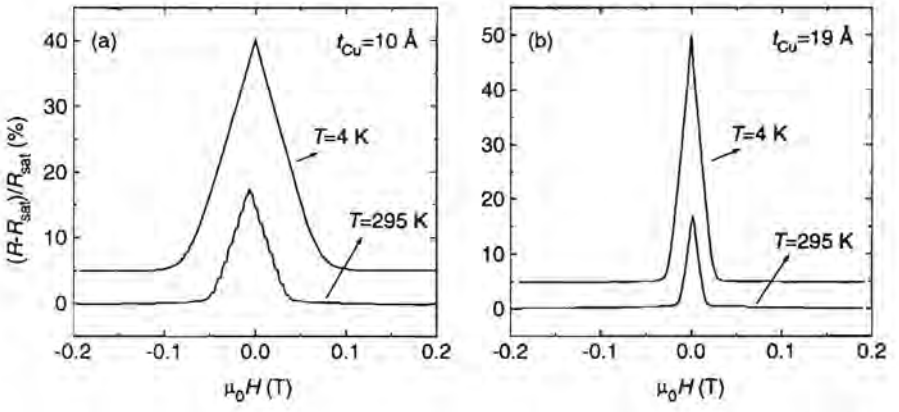

Figure 4.19. *Magnetoresistance curves at room temperature and at 4 K for (100)-oriented multilayers (a) 100×[NiFe(16 Å)+Cu(10 Å)] and (b) 100× [NiFe(16 Å)+Cu(19 Å)] grown on Cu buffer layers of 200 Å. The magnetic field was in the plane of the layers and perpendicular to the current direction. The structure on the bottom curve of (a) is an artefact of the measurement.*

only little intensity of NiFe/Cu(111) reflections present. From the full width at half maximum (FWHM) of the NiFe/Cu(200) reflection, which is 0.40°, we deduce a perpendicular crystal coherence length of about 230 Å. This value is nearly the same for all our (100)-oriented NiFe multilayers and comparable to previously grown Co/Cu(100) multilayers (Ref. 77 and section 4.2). The FWHM of the rocking curves about the (200) maximum (not shown) varied between 1.5° and 2.0°, indicating the good texture of the crystallites.

4.3.2 Results and discussion

In Figs. 4.19(a) and 4.19(b) we show typical MR curves both at room temperature (RT) and at 4 K for two NiFe/Cu multilayers with Cu spacer layer thicknesses, t_{Cu}, of 10 and 19 Å, respectively. We define MR as $(R_{max} - R_{sat})/R_{sat}$, with R_{max} the maximum resistance around zero magnetic field and R_{sat} the value at saturation. We observe high MR values at RT of 18% for the multilayer with $t_{Cu} = 10$ Å (35% at 4 K) and 17% for the multilayer with $t_{Cu} = 19$ Å (45% at 4 K). These two copper thicknesses correspond to the first two antiferromagnetic (AF) maxima of the interlayer exchange coupling in the NiFe system. From the magnetic field at which the MR saturates, H_s, one can deduce the magnitude of this AF-coupling strength, J_{AF}, via the relation $J_{AF} = \mu_0 H_s M_s t_F/4$, with M_s and t_F the saturation magnetization and the thickness of the magnetic layers, re-

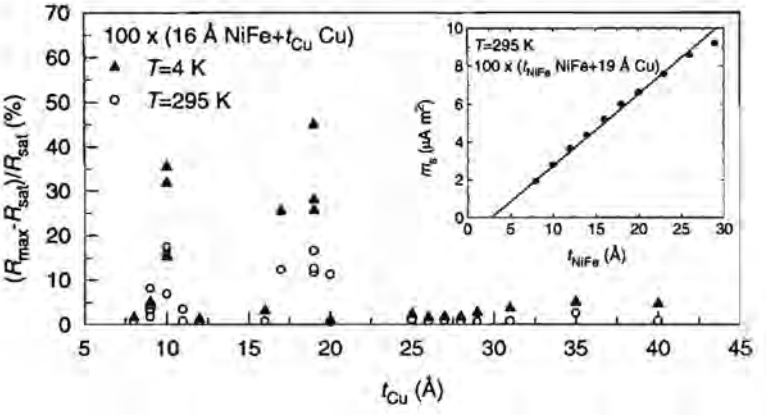

Figure 4.20. *Dependence of the magnetoresistance ratio on the Cu spacer layer thickness, t_{Cu}, for (100)-oriented 100×[NiFe(16 Å)+Cu(t_{Cu} Å)] multilayers grown on Cu buffer layers of 200 Å.* **Inset:** *Saturation magnetic moment, m_s, versus the NiFe layer thickness, t_{NiFe}, for a series of multilayers with t_{Cu} =19 Å.*

spectively. For $t_{Cu} = 10$ Å a coupling strength $J_{AF} = 0.013\,mJ/m^2$ at RT is found and $J_{AF} = 0.023\,mJ/m^2$ at 4 K. These values are about a factor of twelve smaller than in our sputtered Co/Cu samples (Ref. 77 and section 4.2). Similarly, for $t_{Cu} = 19$ Å we find $J_{AF} = 4.3 \times 10^{-3}\,mJ/m^2$ at RT and $J_{AF} = 7.4 \times 10^{-3}\,mJ/m^2$ at 4 K, approximately 16 times smaller than in comparable Co/Cu samples. This relatively small coupling strength, and hence H_s, leads to a sizable sensitivity of $\Delta R/(R\,\Delta H) = 0.19\%/Oe$ at 4 K for $t_{Cu} = 19$ Å.

The temperature dependence of J_{AF} in both AF maxima appears to be the same. This is in marked contrast to the results of Parkin [107], who found that J_{AF} in the second AF peak (around $t_{Cu} = 20$ Å) falls off dramatically with increasing temperature, resulting in no measurable AF coupling or MR at RT. This different behavior was attributed to the dissolution of NiFe and Cu at the NiFe/Cu interfaces, being more important for thicker t_{Cu}. Figure 4.20 depicts the MR behavior of NiFe(16 Å)/Cu multilayers as a function of t_{Cu}. Both at RT and at 4 K an oscillatory behavior can be observed with a period of approximately 10 Å. Apparently, in our case, there is no substantial increase of the mixed region at the NiFe/Cu interfaces for the multilayers with thicker t_{Cu} (say 20 Å). This conclusion is supported by measurements of the saturation magnetic moment of NiFe/Cu(19 Å) multilayers as a function of t_{NiFe}, which is shown in the inset of Fig. 4.20. The slope of this curve reflects the bulk value of M_s of NiFe of

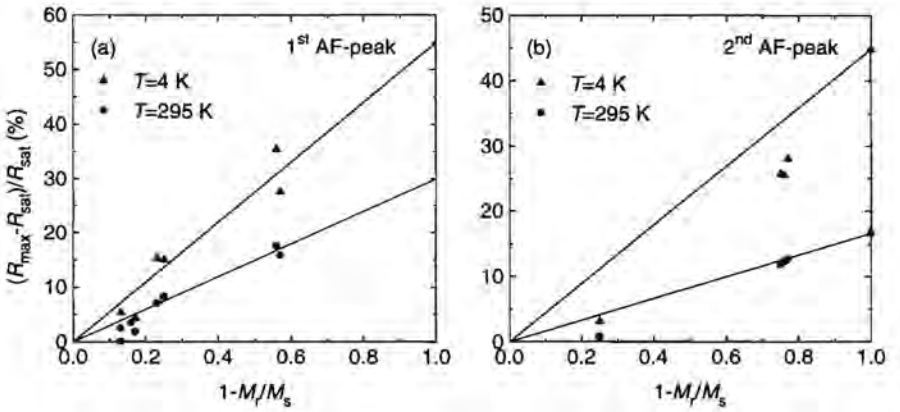

Figure 4.21. *Magnetoresistance ratio versus $(1 - M_r/M_s)$ for (100)-oriented $100\times$[NiFe(16 Å)+Cu(t_{Cu} Å)] multilayers with (a) t_{Cu} around the first antiferromagnetic- (AF-) coupling peak and (b) t_{Cu} around the second AF-coupling peak.*

1.0 T. The offset from the origin can be attributed to a nonmagnetic layer at the NiFe/Cu interfaces with a thickness of about only 1.5 Å, as was also found by Speriosu and coworkers [108].

To compare the MR data of the first and second AF maximum properly, a correction for the fraction of AF coupling, F_{AF}, in the multilayers has to be made. For example, the sample of Fig. 4.19(a) exhibits only a F_{AF} of 63% as determined from the remanence measured with a vibrating sample magnetometer. In Figs. 4.21(a) and 4.21(b) plots of MR versus F_{AF} for our NiFe/Cu multilayers are given for $t_{Cu} \approx 10$ Å (1st AF peak) and $t_{Cu} \approx 19$ Å (2nd AF peak), respectively. From these plots we can deduce the MR values for a completely antiparallel alignment by extrapolation. At 4 K we find MR values of 55% for $t_{Cu} \approx 10$ Å and 45% for $t_{Cu} \approx 19$ Å. We only compare these low-temperature data with the magnetoresistance model of Levy *et al.* [37,38], since it is assumed that electric conduction takes place in two separate spin channels. At elevated temperatures spin-flip scattering, which effectively mixes both spin channels, may disturb a proper analysis. Also another set of MR data was measured at $T = 4$ K in which the magnetic layer thickness, t_{NiFe}, has been varied. Again, these MR values are corrected for incomplete antiparallel alignment. A detailed description of the fitting procedure is given elsewhere (see Ref. 77 and sections 3.3.1 and 4.2). Important fitting parameters of the model are p_i and p_b, representing the ratio of spin-dependent to spin-independent scattering at the interfaces or bulk

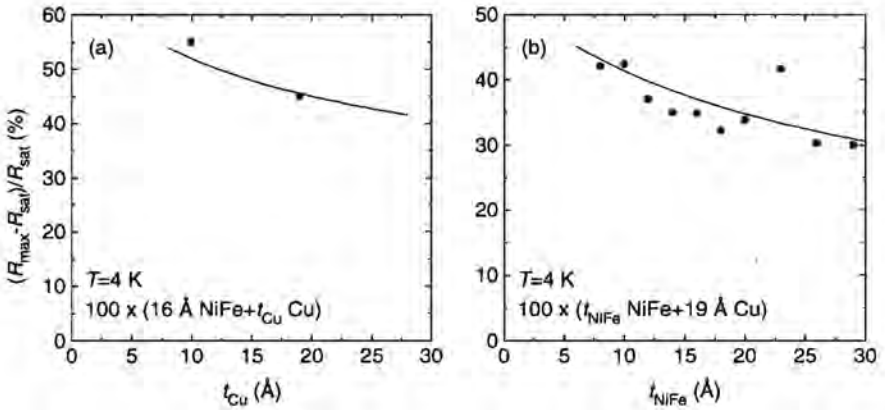

Figure 4.22. *Dependence of the magnetoresistance ratio on the Cu spacer layer thickness, t_{Cu}, at $T = 4\,K$. The solid line is calculated using the magnetoresistance model of Levy et al. (Refs. 37,38 and section 3.3.1). (b) Dependence of the magnetoresistance ratio on the magnetic layer thickness, t_{NiFe}, at $T = 4\,K$. The solid line represents the model calculation. Fitting parameters are indicated in the text.*

lattice-planes, respectively. These parameters are related to the more conventional spin-asymmetry parameter $\alpha = \lambda_\uparrow/\lambda_\downarrow$ according to $\alpha = (1+p)^2/(1-p)^2$. In Figs. 4.22(a) and 4.22(b) we plot the results of the fits with the parameters $p_i = 0.38$ ($\alpha_i^{NiFe/Cu} = 5.0 \pm 0.4$) and $p_b = 0.18$ ($\alpha_b^{NiFe} = 2.1 \pm 0.3$). The values for the mean-free path, λ, for NiFe and Cu used in the calculations are $\lambda^{NiFe} = 60$ Å and $\lambda^{Cu} = 200$ Å. Both data series have been fitted with the same parameter set. These spin-asymmetry parameters of NiFe and NiFe/Cu are significantly smaller than those for our Co/Cu multilayers ($\alpha_i^{Co/Cu} = 21 \pm 3$ and $\alpha_b^{Co} = 2.6 \pm 0.3$; see Ref. 77 and the previous section), but it is still the spin dependence of the interface scattering that plays the dominant role. A similar conclusion can be drawn from current-perpendicular-to-plane MR measurements by Yang *et al.* [5,47] on Co/Cu/NiFe/Cu multilayers with rather large individual layer thicknesses. However, our α-values are somewhat smaller. In general, for various multilayer systems, α_i seems to depend highly on the exact microstructure, orientation, and deposition conditions of the samples. Although still within experimental uncertainty, a possible explanation for the discrepancy between the experimental bulk values α_b^{NiFe} was recently suggested by Rijks *et al.* [109], who showed that grain-boundary scattering may reduce the effective spin dependence of the scattering.

4.3.3 Conclusions

We have grown sputtered NiFe/Cu(100) multilayers (NiFe=$Ni_{80}Fe_{20}$) on Cu buffer layers and observed an oscillatory behavior of the magnetoresistance (MR) as a function of the Cu spacer-layer thickness even at room temperature. The measured MR values are directly proportional to the antiferromagnetically coupled fraction in the multilayers. We have interpreted low-temperature MR data, corrected for incomplete antiparallel alignment, with the magnetoresistance model of Levy *et al.* (Refs. 37, 38 and section 3.3.1) and found that the spin dependence of the NiFe/Cu-interface scattering is the most important source for the giant MR effect.

Chapter 5

Current-Perpendicular-to-Plane Magnetoresistance Experiments

5.1 New Contacting Technique for Thin Film Resistance Measurements Perpendicular to the Film Plane*

Using microlithography, we have fabricated Au thin film structures for resistance measurements with the current directed perpendicularly to the film plane. We propose a novel contact geometry for an accurate measurement of the very low metallic perpendicular resistance, which prevents any disturbing influence from the much larger resistance of the contact leads. Our experimental results are well explained by a classical model and our interpretation is independently confirmed by a three-dimensional electrostatic calculation based on the finite element method.

5.1.1 Introduction

Resistance measurements on metallic superlattices (see, e.g., Ref. 110) revealed interesting effects, which originate from the anisotropic conductance implemented by the artificial multilayer period. Mostly, these experiments are done using a measuring current parallel to the multilayer plane, but a complete study of the resistance anisotropy would also require measurements with the current perpendicular to the plane. However, the latter experiment is not straightforward at all, basically because the perpendicular resistance of a microstructured thin film typically is much smaller than the resistance per square, $R^{\square}$, of the contact leads. This is the reason why, until now, reliable perpendicular resistance measurements on thin films only were done at low temperatures using superconducting contact electrodes (see, e.g., Ref. 111). Hence, there is a need for a specific contact geometry, which allows a proper measurement of the perpendicular resistance of a metal film and can be used at all temperatures. This would not only be interesting for fundamental purposes, but also from an application point of view : several theoretical articles [12, 42, 44, 51, 112] predicted for magnetic multilayers a

* Apart from small changes, this section has been published in Appl. Phys. Lett. **63**, 111 (1993).

giant magnetoresistance effect, which is typically an order of magnitude larger for the current perpendicular-to-plane case than for the current in-plane case. This enhanced effect indeed was observed at 4.2 K in Co/Ag and Co/Cu multilayers [13, 113].

In this section we demonstrate a thin film contacting geometry suitable for measuring ultra-low perpendicular thin film resistances, which eliminates spurious resistance contributions from the contact leads. We compare this geometry with a slightly different geometry in which contact lead resistance effects do play a role. For demonstration purposes we discuss only test samples fabricated from pure Au, but our discussion can be easily generalized to other kinds of films or multilayers. By comparing the resistance behavior of the two geometries we determined the contribution of the contact leads and of the proper perpendicular resistance; our results are in quantitative agreement with a classical Ohmic model. Moreover, we have confirmed our conclusions independently by an electrostatic calculation based on the finite element method.

5.1.2 Sample preparation

The sample layout is sketched schematically in Fig. 5.1. Figure 5.1(a) shows the cross section of the center of the structure. A sputtered Au base layer of thickness t ($t = 0.3$ or $1.9\,\mu$m) is covered with $0.1\,\mu$m of Mo and a $0.9\,\mu$m-thick insulating polyimide (PI) layer (Probimide 408), which in turn is covered by a $0.1\,\mu$m-thick Mo layer. The Mo serves just as an adhesion promoter for the PI and the Au, respectively. Using standard photoresist (HPR 204)-based lithography, combined with wet etching for the Mo and oxygen plasma etching for the PI ($10\,\mu$bar pressure with a power density of $0.26\,\mathrm{W/cm^2}$ during 15 min), a hole is etched in the PI with a radius r ranging between 3 and $9\,\mu$m. Finally, immediately after an Ar-ion surface cleaning process, the top Au layer is deposited and structured using wet etching in an I_2/KI solution, followed by wet Mo etching. Figure 5.1(b) is a simplified top view of the structure obtained, in which the top and bottom Au electrodes and the hole in the PI, forming a microconstriction between the two Au layers, are indicated. We will call this structure "geometry I" in the following. Using a four-probe measuring technique (with current leads I^+ and I^- and voltage leads V^+ and V^-), we aim to measure only the resistance of the conceptually cylindrical Au "pillar" with a ground plane area of πr^2 defined by the hole in the PI. This will turn out to be impossible for geometry I, due to spreading resistance effects in the lead electrodes. As a solution to this problem, we propose the structure of Fig. 5.1(c) (called "geometry II" in the following), which differs from geometry I only by additional trenches, etched down to the substrate using a Nd-YAG laser (532 nm).* This structure allows a reliable measurement of

* The Nd-YAG laser etching results in narrowing down the contact leads of the pillar (see section 2.1.4). Alternatively, this can be realized using an appropriate lithographic process, which have been demonstrated recently by Vavra *et al.* [114].

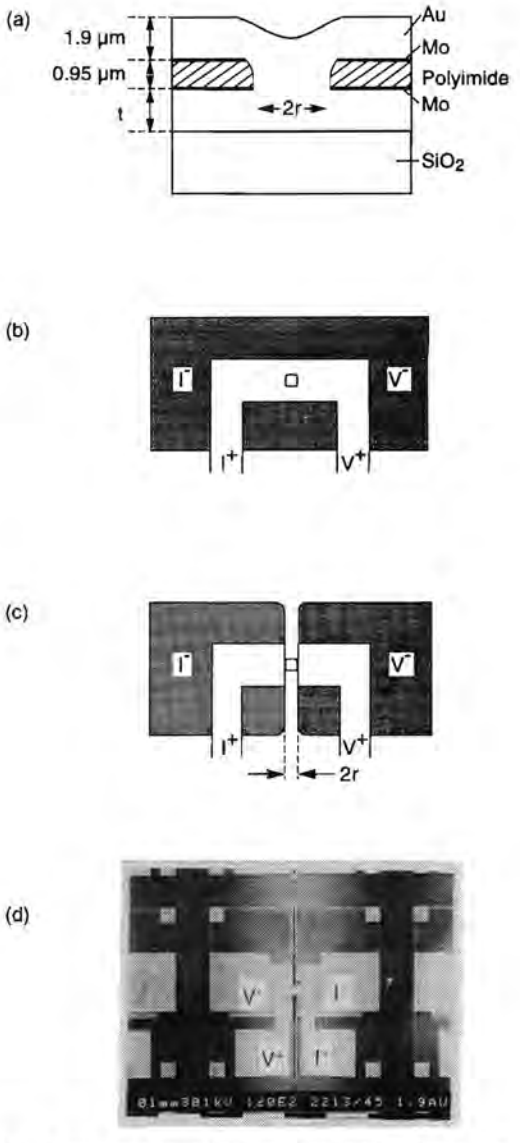

Figure 5.1. *(a) Cross section of the central part of our Au test structure. (b) Top schematic view of our "geometry I" type structure, indicating current (I^+ and I^-) and voltage (V^+ and V^-) leads. The bottom Au layer is shaded, the constriction is indicated by the circular-like center structure. (c) Top schematic view of our "geometry II" type structure, with the additional laser-etched trench. (d) Scanning electron microscopy picture of the structure corresponding to the situation of (c).*

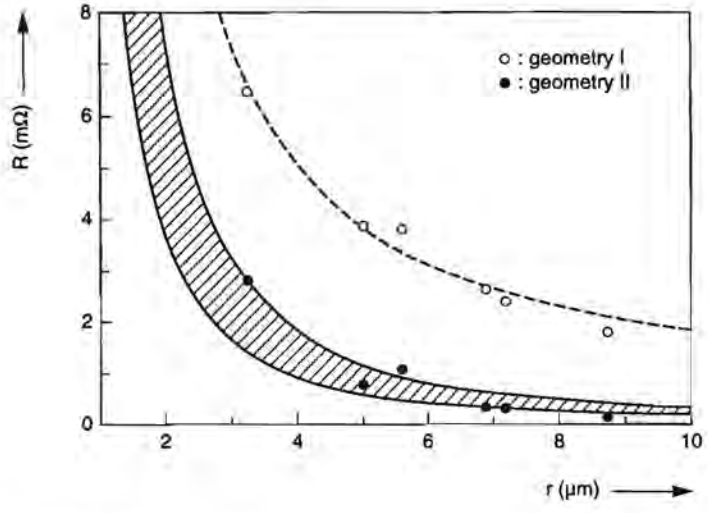

Figure 5.2. *Experimental resistance as a function of the hole radius, r, for geometry I and geometry II. The hatched region corresponds with the "ideal case", in which only the perpendicular Au resistance is measured. The dashed curve is calculated using Eq. (5.1) and includes the contributions from both the perpendicular resistance and the spreading resistance in the lead electrodes.*

the perpendicular resistance without any disturbing electrode effects, as we will discuss. A scanning electron microscope picture of the complete structure with Au bonding contacts is shown in Fig. 5.1(d).

5.1.3 Perpendicular resistance measurements

In Fig. 5.2 the experimentally measured resistance as a function of hole radius r is indicated for the two geometries for a bottom electrode thickness $t = 1.9\,\mu$m. Geometry I gives systematically higher values than geometry II. The hatched region represents the resistance values one would measure in the "ideal" case (i.e., only the perpendicular resistance of the Au). The full curves forming the borders of that region are given by $R = (90\,\text{m}\Omega\,\mu\text{m}^2)/(\pi r^2)$ and $R = (45\,\text{m}\Omega\,\mu\text{m}^2)/(\pi r^2)$, representing the true perpendicular resistance of a Au pillar with a height of 3.8 and 1.9 μm, respectively, corresponding to the complete film thickness and half of that thickness, respectively, while taking for Au a resistivity $\rho = 2.4\,\mu\Omega\,\text{cm}$. It is clear that the measurements for geometry II are within or close to this ideal region. The dashed curve through the experimental points of geometry I is a

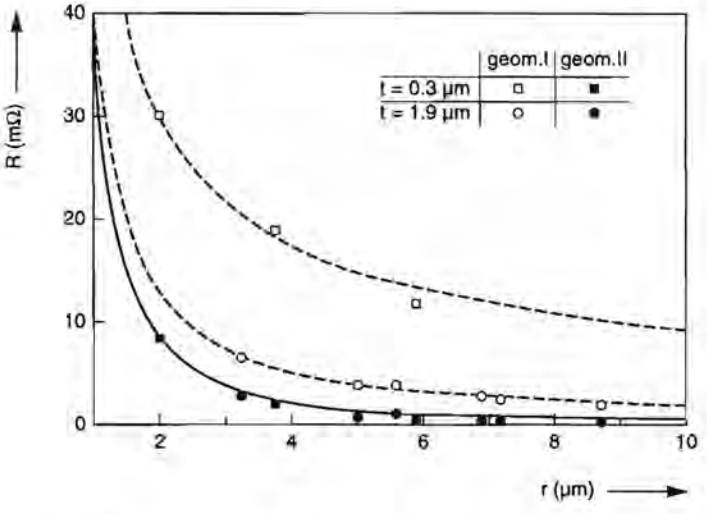

Figure 5.3. *Experimental resistance as a function of the hole radius, r, for the two geometries and for two different thicknesses, t, of the bottom electrode. The full curve is calculated for the ideal case and the dashed curves include electrode spreading resistance effects.*

fitting curve calculated from

$$R = \frac{R^{\square}}{\pi} \ln\left(\frac{r+A}{r}\right) + \frac{B}{\pi r^2}, \tag{5.1}$$

with A and B fitting parameters. The second term on the right of Eq. (5.1) is the perpendicular resistance of the Au, while the first term equals $(\rho/t\pi)\int_r^{r+A} dx\, x^{-1}$ and is a two-dimensional (Maxwell) spreading resistance in the electrodes. For the given sample $R^{\square} \equiv \rho/t = 11\ \mathrm{m\Omega/\square}$. It is assumed that the measuring current spreads radially around the hole with radius r, giving rise to a measurable voltage drop typically over a distance A away from the hole. For the dashed curve in Fig. 5.2 we found $A = 5.16\,\mu\mathrm{m}$ and $B = 105\,\mathrm{m\Omega}\,\mu\mathrm{m}^2$. Clearly by going from geometry I to geometry II, we eliminate the electrode spreading resistance contribution. This is even more evident from Fig. 5.3, where additional measurements are shown for samples with a $0.3\,\mu\mathrm{m}$ thick bottom electrode, which due to its larger $R^{\square} = 70\,\mathrm{m\Omega/\square}$ gives rise to a much larger spreading resistance effect. From this fit we find that $B = 103\,\mathrm{m\Omega}\,\mu\mathrm{m}^2$ and that $A = 12\,\mu\mathrm{m}$ in the bottom electrode. Clearly the resistance of the Au pillars is equal for both series of samples, which explains why for geometry II all points are nearly on a single curve.

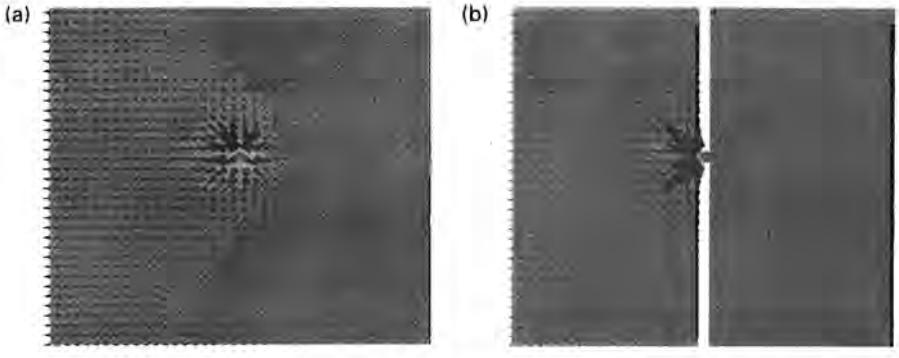

Figure 5.4. *(a) Finite element calculation and vector plot of the electric field in the bottom electrode of a structure corresponding to geometry I. (b) Same as (a), but for a structure with laser-etched trenches, corresponding to our geometry II.*

Independent confirmation of our explanation for this geometrical effect was obtained with the three-dimensional simulation package TOSCA [115]. More specifically, electrostatic calculations, based on the finite element method, were done for a structure consisting of two $140 \times 140\,\mu m^2$ square films with a thickness of 1.9 and $0.3\,\mu m$, respectively, centrally connected by a $4 \times 4\,\mu m^2$ pillar with a height of $1\,\mu m$. When a current is flowing from the top to the bottom electrode, just as in the case of our geometry I, we find the electric field distribution as shown in Fig. 5.4(a) in arbitrary units. The direction of the arrows corresponds to the direction of the field and their thickness to the field magnitude. It is clear that, between the voltage probes (situated on the right of the figure), a large spurious voltage contribution from the leads is present. For the simulated structure, we find, using contour integration, that only 3% of the totally measured voltage actually corresponds to a voltage drop over the perpendicular resistance. This number increases to 100% in the case of Fig. 5.4(b), which is the simulation for a structure with a trench corresponding to our geometry II.

In summary, we have proposed, experimentally studied, and theoretically explained a new contacting technique, which allows the measurement of the thin film resistance perpendicular to the film plane. We used Au as the testing material for our geometry, but we want to stress that our structuring method is widely applicable to thin films made of other materials and to multilayer configurations. For example, a multilayer was sandwiched between two metallic layers for contacting and then etched back into a pillar, after which the structuring described in this section took place (Ref. 64 and section 5.3). We think that our contacting

technique for such anisotropic systems may lead to the discovery of new effects with possibly high application potential.

5.2 Current-Distribution Effects in Microstructures for Perpendicular Magnetoresistance Experiments*

We present a simple Ohmic model to calculate the current distribution in small pillar-like structures for perpendicular magnetoresistance experiments. These calculations are consistent with three-dimensional electrostatic simulations, based on the finite element method, and facilitate the analysis of magnetoresistance data of microstructured multilayers.

5.2.1 Introduction

Since the discovery of the giant magnetoresistance (MR) effect [1] in magnetic multilayers, a large variety of multilayer systems has been investigated [84, 85, 89, 102, 103, 116–118]. Almost all experimental data concern the so-called current-in-plane (CIP) geometry, in which the measuring current is along the plane of the multilayer. Up to now, only two groups have reported on MR experiments where the current is perpendicular to the plane of the multilayer (the so-called CPP geometry) [13, 64, 113]. The CPP geometry is of particular interest, since it can identify more clearly than the CIP geometry the separate contributions from spin-dependent bulk and interface scattering to the giant MR effect [13, 113]. However, such a CPP-MR experiment is certainly not straightforward, essentially because of the very low perpendicular thin film or multilayer resistance involved. In principle, one can think of two solutions to this problem. One is to use superconducting leads. This was done by Pratt *et al.* [13, 113], who measured the CPP-MR of Co/Ag and Co/Cu magnetic multilayers using crossed (superconducting) Nb top and bottom electrodes. With this method, they were able to determine the CPP-MR at low temperatures with an ultra-sensitive SQUID-based system. The second way is to increase the perpendicular multilayer resistance into a more simply measurable range by fabricating micron-size structures by means of optical lithography and reactive ion etching techniques, as was recently demonstrated in our previous paper (Ref. 65 and the previous section). The advantage of the latter method is the possibility of studying the temperature dependence of the CPP-MR effect. When using such very small structures on the other hand, extreme care has to be taken in order to discriminate between spreading resistance effects originating from the contact leads and the proper perpendicular resistance [65]. Apart from the low perpendicular resistivity itself, another, very general, complication will arise. Even in the case of the structures

* Apart from small changes, this section has been published in J. Appl. Phys. **75**, 5154 (1994).

with the smallest diameter obtained thus far [64, 65] (see also sections 3 and 4 of this chapter), the height of such "pillars" (0.5-1 μm) is still small compared to their width (3-10 μm). As a consequence, the perpendicular current distribution in the pillars is nonuniform, which makes additional corrections for the actual measured resistance in some cases necessary.

In this section, we present a simple Ohmic model to calculate analytically the current distribution in two different experimental measuring geometries [65]. The results of these calculations are consistent with numerical electrostatic calculations, based on the finite element method. Finally, for the geometry that measures the proper perpendicular pillar resistance with negligible contributions from the contact leads, we use our expressions to interpret the CPP-MR data of microstructured Fe/Cr and Co/Cu multilayers.

5.2.2 Current-distribution calculations

The two measuring geometries we are going to describe are depicted in Fig. 5.5. Figure 5.5(a) shows a schematic side view of a microstructured pillar, in which typical dimensions of the various parts are indicated. The actual multilayer (ML) for the perpendicular resistance experiment is in contact with a base layer (B) of thickness 0.3 μm and a top layer (T) of thickness 1.9 μm; the current (I^+, I^-) and voltage (V^+, V^-) contact configuration is indicated, whereas the hatched part is insulating material. In Figs. 5.5(b) and 5.5(c), top views of the two different geometries are given. In the remainder of this section, we will call the structure of Fig. 5.5(b) geometry I and the one of Fig. 5.5(c) geometry II. Geometry II differs from geometry I only by two additional trenches etched through the complete structure. As explained in Ref. 65 and the previous section, these trenches prevent the measuring current from spreading out radially in the top and bottom electrodes. In the case of geometry I, this results in a contact resistance contribution, which cannot be eliminated even though we use a four-probe technique. So, in geometry I, this contact resistance adds to the totally measured resistance and can be much larger than the actual perpendicular resistance of the thin film or multilayer [65].

The difference between the two geometries can be demonstrated by means of electrostatic simulations, based on the finite element method [115]. These were done for a test structure consisting of two $140 \times 140\,\mu\text{m}^2$ square films with thicknesses of 1.9 and 0.3 μm, respectively, centrally connected by a $4 \times 4\,\mu\text{m}^2$ pillar with a height of 1 μm. When a current is flowing from the top to the bottom electrode, we find equipotential lines in the 0.3 μm thick bottom electrode as shown in Fig. 5.6. In the case of geometry I without trenches [see Fig. 5.6(a)], one can indeed observe clearly the presence of a large spurious voltage-drop contribution from the contact leads. This effect is eliminated in geometry II [see Fig. 5.6(b)] and the totally measured voltage drop actually corresponds to a voltage drop over the perpendicular film resistance. However, the pillar height is still

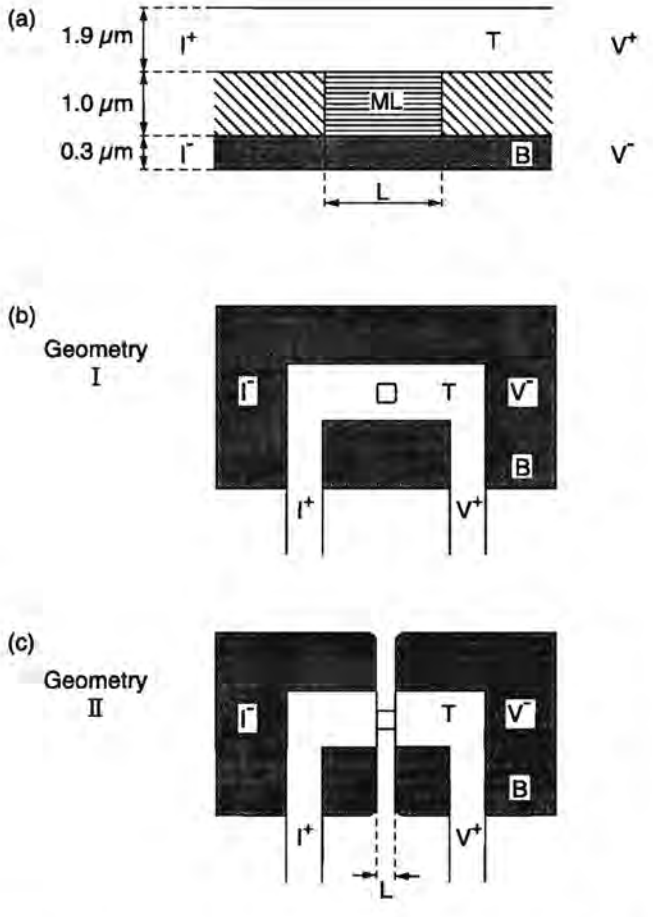

Figure 5.5. *(a) Side view of the central part of the structure for the perpendicular resistance experiment. The actual multilayer is indicated by ML, whereas T and B mark the top and bottom electrodes, respectively. The hatched part of the structure is insulating material. (b) Schematic top view of our geometry I. The constriction is indicated by the square-like structure in the center. For clarity, the insulating layer has been omitted. (c) Schematic top view of our geometry II, with the additional laser-etched trenches.*

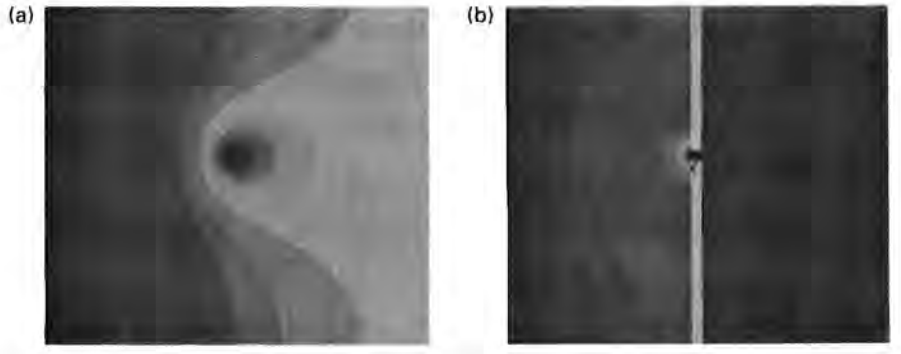

Figure 5.6. *Finite element calculation of the equipotential line distribution in the bottom electrode in the case of (a) geometry I (without laser-etched trenches) and (b) geometry II (with trenches). For each simulation the current drain is on the left and the voltage contacts are on the right.*

relatively small compared to its width, which gives rise to a nonuniform current distribution in the pillar. The analytical calculation of this current distribution in the two geometries and the effect on the resistance measurement is the subject of this section.

a. geometry I

The finite element simulation of Fig. 5.6(a) already revealed that, in the case of geometry I, the total current i driven through the pillar spreads out almost radially in the top and bottom electrode. Therefore, it seems appropriate to approximate the pillar by a cylinder (with radius R) in our analytical model. Figure 5.7 shows a schematic current diagram. We assume, for $r \geq R$, a homogeneous current density $j_t(r) = -i/(2\pi r\, d_t)$ in the top electrode and $j_b(r) = i/(2\pi r\, d_b)$ in the bottom electrode, with d_t and d_b the thicknesses of the top and bottom electrode, respectively, and r the radial coordinate of the cylinder. For $r < R$, $j_t(r)$ changes monotonically to zero at the center of the pillar (where $r = 0$), so that $j_t(r)$ is gradually transformed into a current flowing perpendicularly through the pillar. In our model, the associated perpendicular current density, $j_p(r)$, also depends on r only. In the bottom electrode this perpendicular current gradually turns into a radial current density $j_b(r)$ again. Using Ohm's law in the different sections of the geometry and current conservation, the following one-dimensional equations hold :

$$\rho_t\, j_t(r) = -\frac{\mathrm{d}V_t}{\mathrm{d}r}, \tag{5.2a}$$

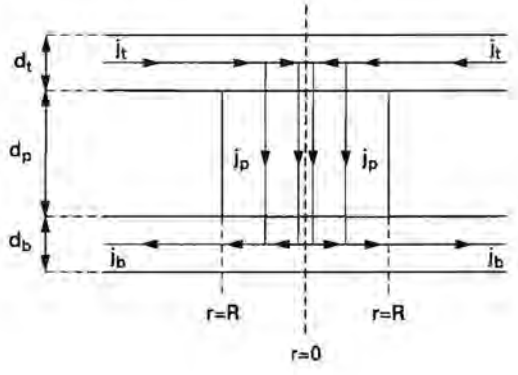

Figure 5.7. *Schematic current diagram for geometry I.*

$$\rho_b\, j_b(r) = -\frac{\mathrm{d}V_b}{\mathrm{d}r}, \tag{5.2b}$$

$$C\, j_p(r) = V_t(r) - V_b(r), \tag{5.2c}$$

$$j_t(r)\, d_t + j_b(r)\, d_b = 0, \tag{5.2d}$$

with ρ_t and ρ_b the resistivities of the top and bottom electrodes, respectively; $V_t(r)$ and $V_b(r)$ are the voltages at r in the top and bottom electrodes, respectively. The constant C is defined by

$$C = \frac{1}{2}(\rho_t d_t + \rho_b d_b) + \rho_p d_p + R_c, \tag{5.3}$$

with ρ_p the resistivity and d_p the height of the pillar. R_c represents a surface contact resistance contribution, which may originate from an unwanted thin oxide layer between the electrode and pillar material formed during deposition. The perpendicular current density $j_p(r)$ through the pillar is related to $j_t(r)$ by current conservation :

$$j_p(r) = -\frac{d_t}{r}\frac{\mathrm{d}(j_t\, r)}{\mathrm{d}r}. \tag{5.4}$$

Differentiating Eq. (5.2c) and inserting Eqs. (5.2a), (5.2b), (5.2d), and (5.4), one obtains for j_t the modified Bessel equation

$$\frac{\mathrm{d}^2 j_t}{\mathrm{d}z^2} + \frac{1}{z}\frac{\mathrm{d}j_t}{\mathrm{d}z} - \left[1 + \frac{1}{z^2}\right] j_t = 0, \tag{5.5}$$

with $r = kz$ and

$$k = C^{\frac{1}{2}} \left(\frac{\rho_t}{d_t} + \frac{\rho_b}{d_b} \right)^{-\frac{1}{2}}. \tag{5.6}$$

Using the boundary conditions $j_t(R) = -i/(2\pi R\, d_t)$ and $j_t(0) = 0$, already mentioned above, the solution to Eq. (5.5) becomes :

$$j_t(z) = \frac{-i}{2\pi R\, d_t\, \mathrm{I}_1(\frac{R}{k})}\, \mathrm{I}_1(z). \tag{5.7}$$

Here, $\mathrm{I}_1(z)$ denotes the modified Bessel function of order 1. Finally, combining Eqs. (5.4) and (5.7), $j_p(z)$ is found to be

$$j_p(z) = \frac{i}{2\pi R\, k\, \mathrm{I}_1(\frac{R}{k})}\, \mathrm{I}_0(z), \tag{5.8}$$

with $\mathrm{I}_0(z)$ the modified Bessel function of zeroth order. In Fig. 5.8, we plot this analytical result together with the outcome of numerical electrostatic calculations, based on the finite element method [115], for the special case where both the electrodes and the pillar are of Au (we take $\rho_{\mathrm{Au}} = 2.4\,\mu\Omega\,\mathrm{cm}$). This choice of material was made for illustrative reasons only, but can very easily be extended to the case of other films or multilayers. Pillar dimensions are indicated in the inset and correspond to typical values for real microstructured multilayers (Refs. 64, 65 and sections 5.3 and 5.4). We observe a good agreement between the numerical calculations and the analytical result of Eq. (5.8), which justifies the one-dimensional approximations made in its derivation. Note that the finite element calculation gives a slightly lower current density on the right side (the side where the voltage leads are located) than on the left side. The solution of the analytical theory is, of course, symmetric with respect to the center of the pillar. So, in the case of the four-point configuration of geometry I, the measured perpendicular resistance of a pillar, R_p, can be deduced by combining Eqs. (5.8) and (5.2c) :

$$R_p = \frac{V_t(R) - V_b(R)}{i} = \frac{C}{\pi R^2}\, \frac{\frac{1}{2}\,(R/k)\, \mathrm{I}_0(\frac{R}{k})}{\mathrm{I}_1(\frac{R}{k})}. \tag{5.9}$$

However, geometry I is, in practice, only suitable for obtaining the proper perpendicular resistance of the pillar in the limit when the resistivity of the contact leads is much smaller than the resistivity of the pillar. Otherwise, the voltage drop in the contact leads can still contribute considerably to the totally measured voltage drop as is the case for our microstructures in Fe/Cr multilayers, where the bottom electrode consists of relatively highly resistive Cr (Ref. 64 and the next section). Using superconducting electrodes on the other hand [13, 113], it follows from Eq. (5.6) that $k \to \infty$ and therefore that $R_p \to C/\pi R^2$, as expected.

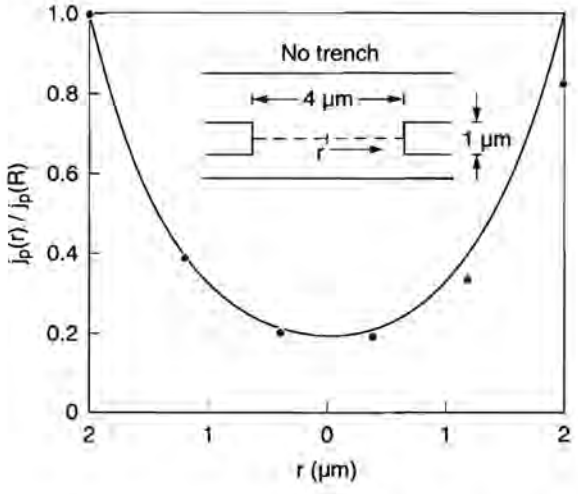

Figure 5.8. *Perpendicular current-distribution in the pillar in the case of geometry I. The solid line is calculated with Eq. (5.8), while the filled circles are the results from a finite element simulation. The inset shows the pillar dimensions used in the calculations. The thicknesses of the top and bottom electrodes are 1.9 μm and 0.3 μm, respectively.*

b. geometry II

In the configuration of our geometry II, two trenches prevent the current from penetrating into the voltage leads on the right side of the structure [see Fig. 5.6(b)]. For symmetry reasons, without changing the basic physics of the problem, we here model the pillar as a parallelepiped with height d_p and square ground surface area L^2. A schematic current diagram is shown in Fig. 5.9. We assume that the current density $j_t(x)$ in the top electrode decreases monotonically from $i/(L\,d_t)$ at the edge of the current lead ($x = 0$) to zero at the edge of the voltage lead ($x = L$), while, on the other hand, the current density $j_b(x)$ in the bottom electrode changes from zero at $x = L$ to $-i/(L\,d_b)$ at $x = 0$. The current density in the pillar, $j_p(x)$, is assumed to be perpendicular. We again make one-dimensional approximations similar to those in Ref. 119, which yields the following equations for electrical transport :

$$\rho_t\, j_t(x) = -\frac{\mathrm{d}V_t(x)}{\mathrm{d}x}, \tag{5.10a}$$

$$\rho_b\, j_b(x) = -\frac{\mathrm{d}V_b(x)}{\mathrm{d}x}, \tag{5.10b}$$

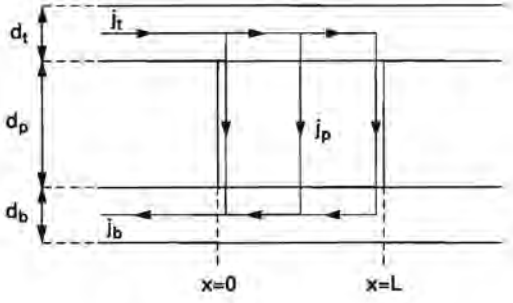

Figure 5.9. *Schematic current diagram for geometry II.*

$$C\, j_p(x) = V_t(x) - V_b(x), \tag{5.10c}$$

$$j_t(x)\, d_t + j_b(x)\, d_b = 0. \tag{5.10d}$$

Here, the same notation holds as in the calculations for geometry I and C is again defined by Eq. (5.3). The current density $j_p(x)$ in the pillar can then be written as

$$j_p(x) = -d_t \frac{\mathrm{d}j_t(x)}{\mathrm{d}x}. \tag{5.11}$$

Following the same procedure as we used for geometry I, one finds as solutions for $j_t(x)$ and consequently $j_p(x)$ in this specific problem :

$$j_t(x) = \frac{1}{L\, d_t} \frac{i}{\sinh(\frac{L}{k})} \sinh\left(\frac{L-x}{k}\right), \tag{5.12a}$$

$$j_p(x) = \frac{1}{L\, k} \frac{i}{\sinh(\frac{L}{k})} \cosh\left(\frac{L-x}{k}\right), \tag{5.12b}$$

where k is defined in Eq. (5.6). A comparison with the finite element calculations is depicted in Fig. 5.10, where we again considered pure Au structures for demonstration purposes. The good agreement allows us to use Eq. (5.12) to calculate the actual measured perpendicular resistance of a pillar, R_p, within the four-point configuration of geometry II :

$$R_p = \frac{V_t(L) - V_b(L)}{i} = \frac{C}{L^2} \frac{(L/k)}{\sinh(L/k)}. \tag{5.13}$$

In the limit $(L/k) \to 0$, we find that $R_p = C/L^2$, just as one expects for a uniform current distribution, whereas in the limit $(L/k) \to \infty$, one obtains a measured resistance $R_p = 0$, because there is no current flowing at the side of the pillar where the voltage probes are located.

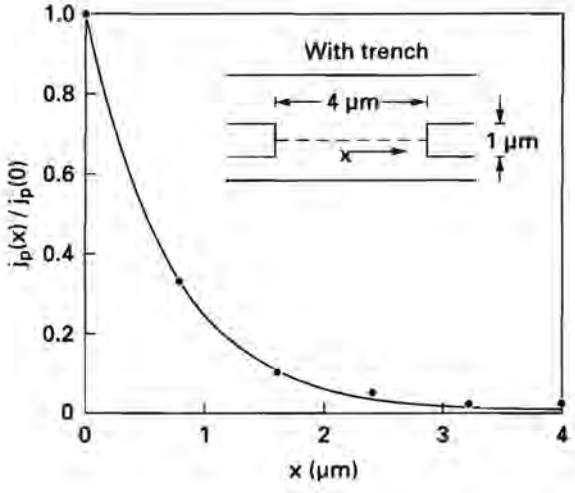

Figure 5.10. *Perpendicular current-distribution in the pillar in the case of geometry II. The solid line is calculated with Eq. (5.12b), while the filled circles are the results from a finite element simulation. The inset shows the pillar dimensions used in the calculations. The thicknesses of the top and bottom electrodes are 1.9μm and 0.3μm, respectively.*

5.2.3 Comparison with experiment and conclusion

In the CPP-MR experiments on Fe/Cr multilayers (Refs. 64, 65 and section 5.3), measuring geometry II was employed, since geometry I is not suitable to measure accurately the proper perpendicular pillar resistance due to the large spurious voltage drop in the relatively high resistive Cr electrode. However, one should note that, because of the resolution of the laser patterning process, it was only possible to etch reproducibly a complete trench to the edge of the largest pillars, whereas for the smaller pillars the trench may end just before the pillar edge. Therefore, to ensure that only the perpendicular pillar resistance value is compared with theory, we consider the variation ΔR_p in the perpendicular resistance of the multilayers between the situations where the magnetic moments of the successive ferromagnetic Fe layers align antiferromagnetically (AF) in zero applied field and where they order ferromagnetically (F) in sufficiently large applied fields. From Eq. (5.13) we find in first order approximation :

$$\Delta R_p = \frac{\Delta C}{L^2} \frac{(L/k_m)}{\sinh(L/k_m)}, \tag{5.14}$$

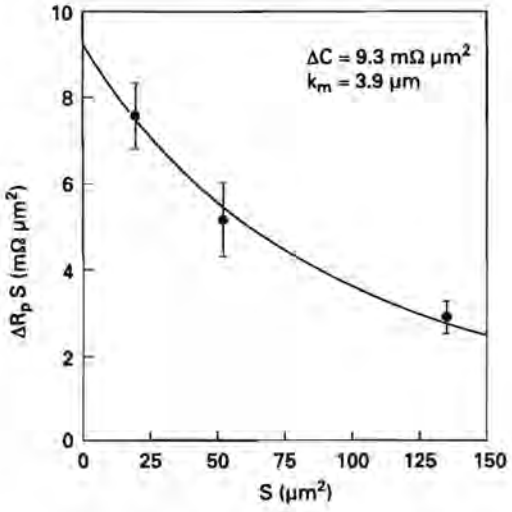

Figure 5.11. *Surface area dependence of $\Delta R_p\, S$ for 100×[Fe(3 nm)+Cr(2.8 nm)] microstructures. ΔR_p is the resistance difference between the situation where the magnetic moments of the successive Fe layers align antiferromagnetically at zero applied magnetic field and ferromagnetically at large enough field, respectively. The solid line represents a fit according to Eq. (5.14) with fit parameters as indicated in the inset.*

with $\Delta C = d_p\, \Delta\rho_p$ and k_m a mean k-value for the F and AF state. In Fig. 5.11, $\Delta R_p\, S$ ($S = L^2$) is plotted as a function of S. The black circles represent actual data derived from microstructured Fe/Cr pillars. Each data point is an average of typically ten different structures of 100×[Fe(3 nm)+Cr(2.8 nm)], corresponding to the second AF coupling maximum. The error bars on each data point reflect the standard deviation. The solid line is a fit according to Eq. (5.14), using parameter values as indicated in the inset of the figure. The somewhat high k_m-value can be explained by a considerable serial contact resistance, R_c. Thus, for this situation we can conclude that, extrapolating to very small pillars ($S \to 0$), the intrinsic $\Delta R_p\, S$-value is typically 1.1-1.2 times larger than the one measured for the smallest pillars.

For the CPP structures in Co/Cu multilayers (Refs. 120, 121 and section 5.4), the situation is quite different. Here, due to the relatively low resistive Cu bottom electrode, the laser-etched trenches of geometry II are much less effective than in the Fe/Cr case in changing the current distribution from the cylindrical pattern of geometry I to the pattern of geometry II. However, even in geometry I, there is

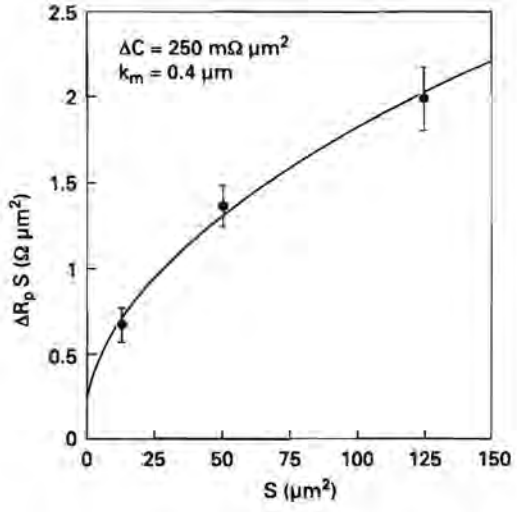

Figure 5.12. *Surface area dependence of $\Delta R_p\, S$ for 180×[Co(1.2 nm)+ Cu(1.1 nm)] microstructures. ΔR_p is the resistance difference between the situation where the magnetic moments of the successive Co layers align antiferromagnetically at zero applied magnetic field and ferromagnetically at large enough field, respectively. The solid line represents a fit according to Eq. (5.15) with fit parameters as indicated in the inset.*

no apparent contribution from the electrode to the totally measured voltage drop because of the very low resistivity of Cu with respect to the perpendicular resistivity of the multilayer. So, now we use geometry I to compare our experimental results of $\Delta R_p\, S$ with. Here

$$\Delta R_p = \frac{\Delta C}{\pi R^2}\, \frac{\frac{1}{2}\,(R/k_m)\; \mathrm{I}_0(\frac{R}{k_m})}{\mathrm{I}_1(\frac{R}{k_m})}. \tag{5.15}$$

follows from Eq. (5.9); again, $\Delta C = d_p\, \Delta\rho_p$ and k_m a mean k-value for the F and AF state. Figure 5.12 shows $\Delta R_p\, S$ ($S = \pi R^2$) as a function of S, where the black circles are actual data from microstructured Co/Cu multilayers and the solid line a fit with Eq. (5.15). One data point represents again an average of about ten microstructures of 180×[Co(1.2 nm)+Cu(1.1 nm)], lying in the first AF coupling peak; the error bars indicate the standard deviation. The difference in behavior from the Fe/Cr microstructures is obvious and results from the different measuring geometries used. The smaller k_m-value for Co/Cu indicates a less pronounced serial contact resistance, but k_m is still somewhat too large to be

explained by Eq. (5.6) only. This can probably be understood by assuming that the change of the radial current density $j_t(r)$ $[j_b(r)]$ not only takes place in the electrode material, but also to a certain extent in the multilayer itself. This would indeed lead to a k_m-value of approximately the height of the pillar.

To summarize, we propose a simple Ohmic model with which we can obtain analytical expressions for the current distribution in small pillar-like structures used to measure the perpendicular resistance of thin films or multilayers. These analytical expressions agree well with numerical electrostatic calculations based on the finite element method, and can be applied in the analysis of CPP-MR data on microstructured magnetic multilayers (Refs. 64, 65, 120 and the next two sections of this chapter).

5.3 Perpendicular Giant Magnetoresistance of Microstructured Fe/Cr Magnetic Multilayers from 4.2 to 300 K*

The fabrication of pillar-shaped microstructures of high vacuum sputtered Fe/Cr magnetic multilayers has enabled us to measure for the first time the giant magnetoresistance effect with the current perpendicular to the film plane from 4.2 to 300 K. At 4.2 K we have found a magnetoresistance of 108% for multilayers with a Fe thickness of 3 nm and a Cr thickness of 1 nm. The pronounced temperature dependence of the perpendicular magnetoresistance has been studied for samples with different Cr thicknesses and compared with current-in-plane measurements.

5.3.1 Introduction

Since the discovery of the giant magnetoresistance (MR) effect in magnetic multilayers [1], numerous studies on a variety of multilayer systems have been reported (e.g., [102, 116]). In practically all these experiments, the measuring current is in the plane of the multilayer, the so-called current-in-plane (CIP) geometry. Nevertheless, the great importance of experiments with the measuring current perpendicular to the multilayer plane (the so-called CPP geometry, which resembles more closely the original spin-valve idea [122]) has been emphasized in several theoretical papers [12, 42, 44, 51, 112]. All these theories are valid only at low temperatures and predict a considerably larger MR effect for the CPP geometry than for the CIP geometry. Up to now, only one experimental group measured the CPP MR for Co/Ag and Co/Cu magnetic multilayers [13, 113]. In these experiments no microfabrication techniques were used; the multilayer was sandwiched between superconducting Nb top and bottom contact electrodes and the very small multilayer resistance (typically 0.01-0.1 $\mu\Omega$) was measured at 4.2 K

* Apart from small changes, this section has been published in Phys. Rev. Lett. **70**, 3343 (1993).

using an ultra-sensitive SQUID-based system. This implies that measurements are only possible at liquid helium temperatures. Consequently, the CPP MR of a strongly antiferromagnetically (AF) coupled system, such as Fe/Cr, which is optimally suited for comparison with existing low-temperature models, was not measured so far due to the large switching fields (typically 400 kA/m) involved with the giant MR effect [84, 85]. At present, the *temperature dependence* of the CPP-MR effect has not been calculated theoretically, nor measured experimentally. Nevertheless, experimental data on the temperature dependence of the perpendicular giant MR effect are highly desirable : they would clarify the role of spin-flip scattering on the giant MR and certainly would trigger new theoretical developments, leading to a CPP-MR theory which is valid at all temperatures.

In this section, we present the first experiments on the temperature dependence of the CPP MR of microstructured multilayers. Pillar structures of a few microns in size were fabricated using optical lithography and reactive ion etching techniques. The perpendicular giant MR effect was measured for $100\times$ [Fe(3 nm)+Cr(t_{Cr})] multilayers with Cr thicknesses $t_{Cr} = 1$ nm, 2.8 nm and 4 nm. The first two thicknesses are in the first two AF regions of the oscillatory coupling between neighboring Fe layers [84, 85, 117], while the last one corresponds to a weaker coupled configuration. The CPP MR* is larger than the corresponding CIP MR, e.g., for $t_{Cr} = 1$ nm, we find a CPP MR of 108% at 4 K, more than four times larger than the CIP MR in similarly prepared multilayers [84, 85]. The CPP MR decreases strongly with temperature. The decrease of the magnetic field induced resistance variation with temperature can be understood in terms of a spin-mixing process by electron-magnon scattering in an anisotropic AF superlattice [123, 124]. Finally, we demonstrate that our low-temperature data are consistent with the model of Valet and Fert (see Ref. 12 and section 3.2).

5.3.2 Sample fabrication

A schematic diagram of the pillar structure is given in the inset of Fig. 5.13(a). Here we present a brief outline of the fabrication method; further information can be found elsewhere (see Ref. 65 and section 2.1.4). First a 0.4 μm-thick Cr base layer is rf sputtered onto a SiO_2 substrate held at room temperature. Then a 0.4-0.7 μm-thick Fe/Cr multilayer is deposited, using dc sputtering for the Fe and rf sputtering for the Cr, followed by a dc sputter deposition of a 0.3 μm-thick Au layer. X-ray diffraction shows a predominantly (110) growth of the multilayer. For lithography the sample is covered by a 0.1 μm-thick Mo layer and then by a 0.2 μm-thick Al_2O_3 layer. This last layer is structured and serves as a mask for the etching of the Au and the Fe/Cr multilayer, which is done in an HCl plasma (40 μbar, 2.1 W/cm^2). After removal of the remaining Al_2O_3, the sample

* We define the MR as $(R_{max} - R_{sat})/R_{sat}$, where R_{max} is the maximum resistance at zero field and R_{sat} the resistance value at saturation of the giant MR effect.

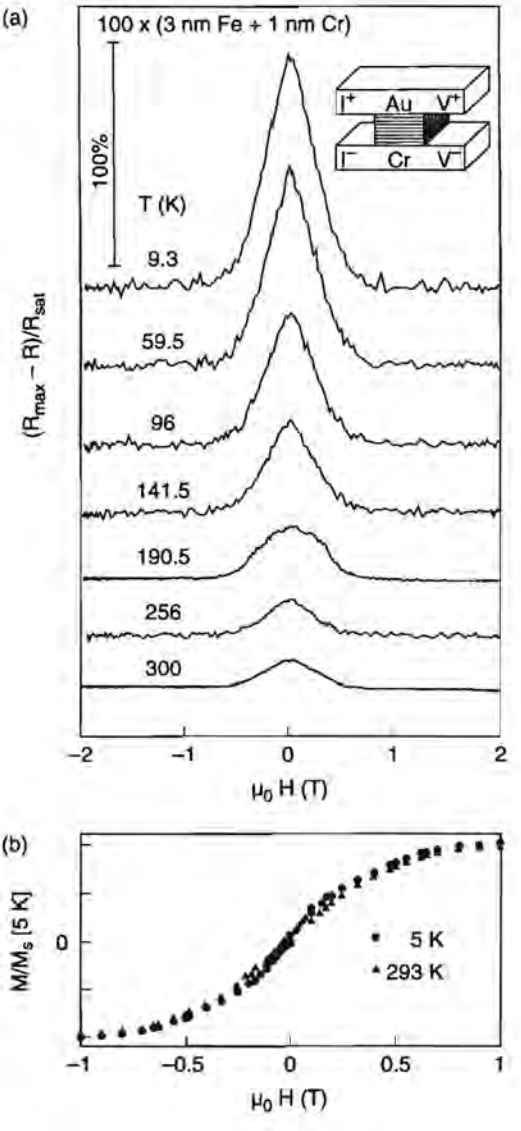

Figure 5.13. *(a) Giant magnetoresistance effect of a microstructured pillar in a 100×[Fe(3 nm)+Cr(1 nm)] multilayer with the current perpendicular to the multilayer plane (CPP) at various temperatures. The inset shows a schematic drawing of the sample. V^+, V^- and I^+, I^- are the voltage and the current contacts of the sample, respectively. (b) Magnetization loops at 5 K and at 293 K, showing the very similar antiferromagnetic coupling behavior at both temperatures.*

is covered with an insulating polyimide layer. Contact holes are etched which are subsequently covered by a 1.9 μm-thick Au film, followed by the structuring of the contact electrodes. A few hundred pillars with a cross section S ranging between 6 and 130 μm^2 are fabricated on one substrate. Fifteen to twenty different pillar structures with variable cross sections were measured for each Cr thickness to check reproducibility. After wire bonding, the samples are mounted in a ^{4}He flow cryostat. Pillar resistances (typically a few mΩ) are measured using an ac bridge technique in the 4-300 K temperature range and in fields up to 1600 kA/m (2 T).*

5.3.3 Magnetoresistance experiments and discussion

Figure 5.13(a) shows CPP-MR curves at different temperatures for a pillar with a cross section $S = 90\,\mu m^2$ structured in a 100×[Fe(3 nm)+Cr(1 nm)] multilayer; for clarity the curves are displaced vertically. At 9.3 K we observe a MR effect of 108%, more than four times higher than the corresponding CIP-MR effect in unstructured films [84, 85]. The MR effect is weakly temperature dependent below about $T = 60$ K; above that temperature the decrease is much stronger. At room temperature a 14% CPP MR remains, two times larger than the corresponding CIP MR. The saturation field B_s ($\equiv \mu_0 H_s$) is defined by the crossing point of the low field resistance decrease with the horizontal line of constant resistance at higher fields. We find that $B_s = 0.54$ T, nearly independent of temperature. This is comparable to the $B_s = 0.51$ T value found for the corresponding CIP sample [84, 85]; the small difference can be explained by a slightly different demagnetization factor. This B_s value corresponds with an interlayer exchange coupling energy per unit surface of 1.3 mJ/m^2 (see Refs. 84, 85). Hence, the interlayer coupling energy is orders of magnitude larger than the thermal energy for our microstructures. This implies that the strong temperature dependence of the CPP MR cannot be attributed to incomplete AF coupling at higher temperatures. Additional evidence for this is presented in Fig. 5.13(b), where we plot the magnetization loops at 5 K and at 293 K for the 100×[Fe(3 nm)+Cr(1 nm)] multilayer, as measured by a SQUID magnetometer (Quantum Design). All magnetization values are normalized by the saturation magnetization M_s at 5 K. The similarity of the two magnetization curves is striking. This confirms that the strong AF coupling is practically independent of temperature in the temperature range studied. For all our multilayer samples we observed such a strong similarity of the magnetization loops, and hence of the AF coupling, at 5 and 300 K.

---

* The resistance of the multilayer is of the same order of magnitude as the contact resistance, which is determined by comparing different multilayer thicknesses. Also the pillar height is relatively small compared to the width, w, which gives rise to a nonuniform current distribution in the pillar. Ohm's law gives for our geometry (see inset of Fig. 5.13) that $(V^+ - V^-)w^2 \propto (w/L)/\sinh(w/L)$ with L typically 2-3 μm. This dependence was checked independently by simulations based on the finite element method (see Ref. 125 and section 5.2). Quoted MR values are extrapolations for $w \to 0$ and typically are a factor 1.1-1.2 higher than the actual measured value for the smallest pillar in each series.

Another remarkable observation is the absence of hysteresis in the magnetoresistance. For the corresponding CIP sample, we found a small, but clear hysteretic effect [84, 85]. We notice that in the (very weakly) AF coupled Ag/Co and Cu/Co CPP samples of Refs. 13, 113 magnetoresistive hysteresis is very important. We therefore believe that both strong AF coupling and microstructuring, which lead to a reduction in the number of magnetic domains, are important for obtaining nonhysteretic MR characteristics.

In Figs. 5.14(a)-5.14(c) the temperature dependence of the CPP MR is shown for multilayers with different t_{Cr}; comparison is made with the corresponding CIP data [84, 85]. Figure 5.14(a) is for $t_{Cr} = 1\,\text{nm}$ and corresponds to the measurements presented in Fig. 5.13. The enlarged CPP-MR effect and its strong decrease with temperature are immediately clear. This decrease is also pronounced for the sample of Fig. 5.14(b) ($t_{Cr} = 2.8\,\text{nm}$, $S = 20\,\mu\text{m}^2$). Above about 100 K, the CPP MR even becomes smaller than the CIP MR. In Fig. 5.14(c), the results on a sample with $t_{Cr} = 4\,\text{nm}$ and $S = 6\,\mu\text{m}^2$ are shown. For this Cr thickness, CIP magnetoresistance and magnetization data indicate weak AF coupling. We observe that the CPP MR is enhanced with respect to the CIP MR and that the temperature dependence is markedly stronger.

The origin of the strong decrease of the CPP MR with temperature can be clarified by investigating the quantity $\Delta R(T) = R_{max}(T) - R_{sat}(T)$. In the inset of Fig. 5.15 we plot $\Delta R(4\,\text{K}) - \Delta R(T)$ versus temperature on a double logarithmic scale for the samples of Fig. 5.14. Within experimental accuracy, the increase of $\Delta R(4\,\text{K}) - \Delta R(T)$ with temperature below about 150 K can be described by a T^2 behavior for all samples. We believe that this temperature dependence is indicative for electron-magnon scattering as the MR-decreasing mechanism. Previously, the temperature dependence of the low-temperature resistivity of dilute magnetic alloys was explained by incoherent (i.e., spin wave-vector-nonconserving) electron-magnon scattering, mixing the two spin channels [123]. In the case of a multilayer consisting of quasi-two-dimensional AF coupled magnetic layers, this mechanism leads to a T^2 dependence of the CIP resistance variation at low temperature [124], as also observed for our AF coupled CIP samples. At higher temperatures, additionally, coherent (i.e., spin wave-vector-conserving) electron-magnon scattering processes contribute, giving rise to a more complicated behavior. Physically, spin-flip scattering due to thermally excited magnons results in equalizing the two spin currents (the classical spin-mixing effect) and also reduces the spin-flip diffusion length l_{sf}. Although a detailed microscopic calculation on the *temperature dependence* of the CPP MR actually does not exist, we hope that our experimental results will stimulate work in this direction.

Here, we compare our low-temperature results with the low-temperature model of Valet and Fert [12], which is similar in approach to the model of Lee *et al.* [44]. It is a theory on a microscopic basis and it takes into account interface spin accumulation effects coming from a difference in chemical potential for spin-up and spin-down electrons. Valet and Fert argue that the most appropriate experimen-

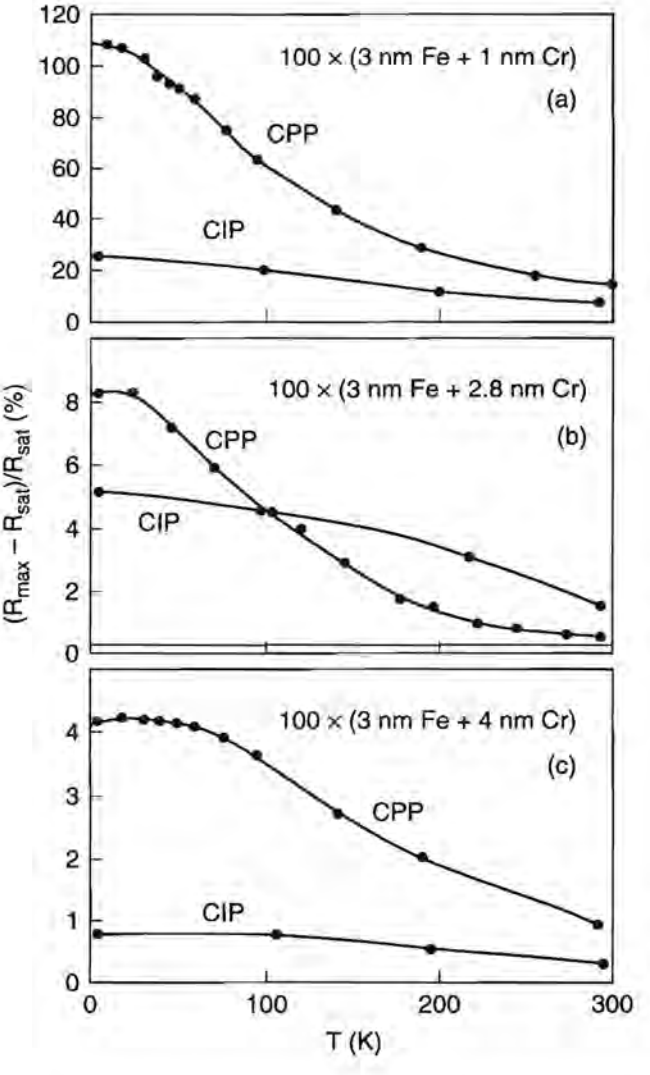

Figure 5.14. *Temperature dependence of the CPP magnetoresistance of pillar structures made in* $100\times[Fe(3\,nm)+Cr(t_{Cr})]$ *multilayers with (a)* $t_{Cr}=1$ *nm, (b)* $t_{Cr}=2.8$ *nm, and (c)* $t_{Cr}=4$ *nm. Corresponding CIP-MR data are given for comparison. The full curves are guides to the eye.*

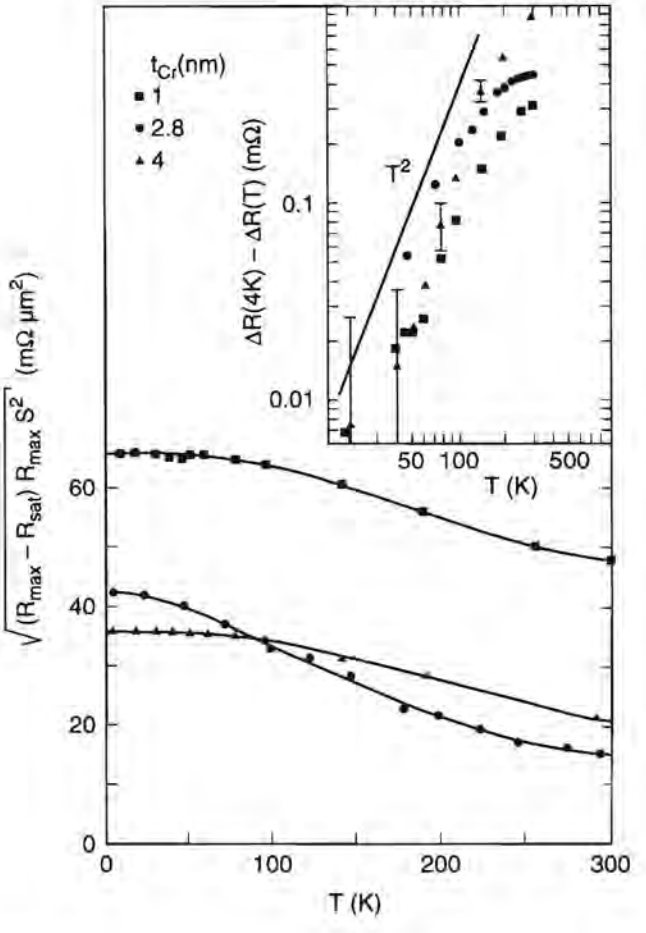

Figure 5.15. *Plot of the temperature dependence of the experimental quantity* $\sqrt{(R_{max} - R_{sat})\, R_{max}\, S^2}$ *given by the Valet-Fert CPP-theory for samples with different* t_{Cr}. *Data are derived from experiments using the extrapolation scheme described in Ref. 125 and section 5.2. Full curves are guides to the eye. The inset shows the temperature dependence of* $\Delta R(4\,K) - \Delta R(T)$ *on a double logarithmic scale. Typical error bars are indicated for several data points. The solid line indicates a* T^2 *behavior, characteristic for electron-magnon scattering in an anisotropic antiferromagnetic system.*

tal quantity to compare with their model is (see also section 3.2):

$$\sqrt{(R_{\max} - R_{\text{sat}})\, R_{\max}\, S^2} = \left[\frac{\beta}{1-\beta^2}\, t_{\text{Fe}}\, \rho_{\text{Fe}} + \frac{2\gamma}{1-\gamma^2}\, r_b\right] M, \tag{5.16}$$

where β and γ are spin-asymmetry coefficients for bulk and interface scattering, respectively ($0 \leq \beta, \gamma \leq 1$). The Fe thickness and Fe resistivity are denoted by t_{Fe} and ρ_{Fe}, respectively; r_b is the spin-averaged Fe/Cr boundary resistance per unit surface in the ferromagnetic state and M is the number of Fe/Cr bilayers in the structure. Equation (5.16) is valid when the spin-flip diffusion length l_{sf} is much larger than the individual layer thicknesses in the structure, a condition which is generally well fulfilled at low temperatures [12]. A plot of the left hand side of Eq. (5.16) is shown in Fig. 5.15 for all temperatures studied. At 4 K, we observe that $\sqrt{(R_{\max} - R_{\text{sat}})\, R_{\max}\, S^2} \approx 65\,\text{m}\Omega\,\mu\text{m}^2$ for the sample with $t_{\text{Cr}} = 1\,\text{nm}$, while for the other two samples this value is reduced to a number around $40\,\text{m}\Omega\,\mu\text{m}^2$. This decrease could indicate the limiting role of l_{sf}, as in samples with larger t_{Cr}, we expect fewer Fe/Cr interfaces and Fe layers to contribute to the giant MR effect. To estimate the magnitude of r_b, we take $\beta = 0.33$ and $\gamma = 0.78$; these values correspond to a ratio of spin-down to spin-up scattering length $l_\downarrow/l_\uparrow = \frac{1+\beta}{1-\beta} \approx 2$ for Fe bulk scattering and $l_\downarrow/l_\uparrow = \frac{1+\gamma}{1-\gamma} \approx 8$ for interface scattering, as obtained from a theoretical analysis of the corresponding CIP-MR data [84, 85].* With $M = 100$, $t_{\text{Fe}} = 3\,\text{nm}$ and $\rho_{\text{Fe}} = 5\text{-}10\,\mu\Omega\,\text{cm}$ we find that $r_b = (1\text{-}1.5) \times 10^{-16}\,\Omega\,\text{m}^2$ for $t_{\text{Cr}} = 1\,\text{nm}$. For the other Cr thicknesses r_b is somewhat reduced. These values are close to the value for r_b found from a similar analysis for the Co/Cu and Co/Ag multilayer system [13, 113]. Although a comparison with the theory is most convenient at low temperatures, where spin-flip scattering is minimum and the two-current model is well applicable, the temperature dependence of the effect is particularly interesting because it provides important new information on the critical length scale of the CPP-MR effect, which we can identify as l_{sf}. As a result of the increasing importance of electron-magnon scattering, the currents are equalized (as in the CIP geometry) and also the reduction of l_{sf} limits the number of layers and interfaces contributing to the CPP-MR effect. The latter is particularly important at high temperatures, where l_{sf} becomes much smaller than the total sample thickness.

In conclusion, we have fabricated pillar-shaped microstructures in Fe/Cr magnetic multilayers and determined for the first time the CPP-MR effect for this strongly AF coupled system. Moreover, we have presented the first experiments on the temperature dependence of the CPP-MR effect and made a comparison with the CIP MR of similarly prepared samples. The decrease of the CPP MR with temperature has been interpreted tentatively in terms of scattering by ther-

* This is in reasonable agreement with the result of a comparison of our CPP-MR data with the Bauer model (Ref. 51 and section 3.3.2), from which we find for the ratio of the scattering lengths, averaged over bulk and interface scattering, that $l_\downarrow/l_\uparrow = 6.4$ [52].

mally excited magnons. Finally we have made a quantitative comparison of our low-temperature data with the model of Valet and Fert.

5.4 Temperature Dependence of the Spin-Dependent Scattering in Co/Cu Multilayers Determined from Perpendicular Giant Magnetoresistance Experiments*

We have fabricated pillar-like microstructures of Co/Cu magnetic multilayers and measured the giant magnetoresistance effect with the current perpendicular to the multilayer plane from 4 up to 300 K. We have analyzed the temperature dependence of the magnetoresistance, using a resistance model of Fert and Campbell, originally proposed for magnetic alloys. We have found that the temperature-dependent scattering rates are strongly spin-dependent, while the spin-mixing scattering rate is small, which explains the relatively weak decrease with temperature of the giant magnetoresistance of Co/Cu.

5.4.1 Introduction

Spin-dependent scattering is at the heart of the giant magnetoresistance (MR) effect in magnetic multilayers [1, 102, 103, 116, 117]. However, the extraction of spin-dependent scattering lengths from experiments is not straightforward, particularly for experiments where the current is in the plane of the multilayer (the so-called current-in-plane (CIP) geometry). In CIP measurements, the conductivity and scattering processes vary on a length scale given by the elastic scattering length, which is mostly of the order of the thickness of individual layers in the multilayer. The situation is conceptually simpler (though much harder accessible experimentally [13, 47, 64, 113, 126]), when the measuring current is perpendicular to the multilayer plane (the so-called CPP geometry); in that case, the results can be analyzed in terms of resistivities, averaged over a large number of layers, since the spin-flip diffusion length is two to three orders of magnitude larger than individual layer thicknesses [12]. The CPP-MR has extensively been studied theoretically [12, 42, 44, 50, 51, 112],† whereby it was assumed that spin-up and spin-down electron channels carry electrical current independently, which is known to be adequate at cryogenic temperatures. At higher temperature, the situation is more complex, because the two spin-channels can mutually influence each other. The temperature dependence due to this so-called spin-mixing by,

---

* Apart from small changes, this section has been published in Phys. Rev. B 50, 16733 (1994).

† We define the MR as $(R_{max} - R_{sat})/R_{sat}$, where R_{max} is the maximum resistance at zero field and R_{sat} the resistance value at saturation of the giant MR effect.

e.g., electron-magnon scattering was not explicitly modeled so far.* Also the few existing experimental results on the temperature dependence of the CPP MR were only qualitatively analyzed [64, 126]. Yet, an understanding of the degree to which spin-mixing occurs, and of the temperature dependence of spin-up and spin-down resistivities is important for providing a basis for a comprehension of the giant MR effect at room temperature.

In this section we present such CPP-MR data as a function of temperature between 4 and 300 K, measured on microstructured pillars defined lithographically in Co/Cu(100) magnetic multilayers. The experimental perpendicular resistivity data are discussed in terms of the resistance model of Fert and Campbell [11], originally proposed to explain the temperature dependence of the resistivity of magnetic alloys. We show that this model can be applied to the CPP-resistivity data and demonstrate that the crucial temperature dependent resistivities for both spin channels, as well as the elastic interchannel spin-mixing resistivity, can be quantified. We find that the temperature-dependent scattering in Co/Cu multilayers is strongly different for spin-up and spin-down electrons, and that spin-mixing is of minor importance. This explains why for Co/Cu the giant MR decreases relatively weakly with increasing temperature.

5.4.2 Sample fabrication

The Co/Cu multilayer stacks were prepared on single crystalline Si(100) substrates in a multichamber MBE system (VG Semicon V80M). Prior to the introduction into the MBE system, the substrates were HF dipped, a procedure which resulted in a sharp low energy electron diffraction (LEED) pattern, characteristic of the Si(100) substrate. All depositions were carried out at room temperature, at a pressure of better than 10^{-10} mbar. The first stage of the multilayer stack involved the deposition of a 300 nm Cu layer, later to be employed as the lower electric contact. A deposition rate of 0.053 nm/s was used, as registered by a calibrated quartz crystal thickness monitor. LEED analysis of the resulting Cu layer indicated that a clear (100) orientation was produced. Subsequent deposition of the Co/Cu multilayer with identical Cu rate and a Co deposition rate of 0.05 nm/s, maintained the (100) orientation established for the Cu base layer. The multilayer stack was completed with the deposition of 300 nm of Au (deposition rate 0.03 nm/s), to be used as the top electric contact. The structuring process of the Co/Cu pillars, using microlithography and reactive ion etching techniques, is similar to that of Fe/Cr multilayers, and has already been discussed in Refs. 64, 65, 126 and section 2.1.4, where also the experimental sample geometries, necessary to allow a proper perpendicular pillar resistance measurement, are described (sections 5.1 and 5.2).

---

* For the CIP-case, a Boltzmann-like model for the temperature dependence of the giant magnetoresistance effect was proposed recently by Duvail *et al.* [35].

5.4.3 Magnetoresistance experiments

In Fig. 5.16(a) we present results on the temperature dependence of the CPP MR of a 180×[Co(1.2 nm)+Cu(1.1 nm)] multilayer ($S = 125\,\mu m^2$). At low temperature we find a MR of 90% and, at room temperature, a MR of 56%. The saturation field B_s ($\equiv \mu_0 H_s$) is defined by the intersection of the extrapolated low-field resistance decrease with the horizontal line of constant resistance at higher fields. For this multilayer, we find that the saturation field $B_s = 0.20\,T$, nearly independent of temperature and, moreover, nearly independent of the in-plane field direction, characteristic for the small anisotropy of fcc Co. This B_s-value can be associated with an interlayer exchange coupling energy per unit area of $0.16\,mJ/m^2$ [77, 90]. We find that the AF coupling is incomplete, as is shown in the magnetization experiments of Fig. 5.16(b). Besides the similarity of the two curves at 50 K and at 300 K, which indicates that the coupling behavior is essentially the same at both temperatures, we see that about 2/3rd of the magnetization signal around the origin reflects ferromagnetic coupling* and only 1/3rd of the sample is AF coupled and contributes to the measured CPP MR. This is also consistent with a CIP-MR reference experiment on a multilayer, grown at the same time on a 30 nm thick Cu buffer layer on a Si(100) substrate. The CIP MR is 43% at 4 K and 21% at room temperature. This last value is one third of the maximum MR (65%), obtained for a an almost completely AF-coupled (100)-oriented Co/Cu multilayer (see Ref. 77 and section 4.2). The problem of growing a thick, perfectly AF-coupled sample is related to the extremely narrow width of the first AF coupling peak of Co/Cu(100) : it has a maximum at 1.0 nm Cu and a width of only 0.3 nm [90] and, hence, is very sensitive to even minor variations of the Cu rate during the evaporation time (3 hours) in the MBE system.

Resistance data like those of Fig. 5.16(a) were obtained for a large number of pillar structures with variable pillar cross sections and are used to deduce the minimum and maximum perpendicular resistivities. Because the height of a pillar is always much smaller than its width, the current-density distribution in the pillar is nonuniform. Therefore, we modeled the current density profile in our experimental geometries, using both the finite element method and analytical calculations (see Ref. 125 and section 5.2). We then extrapolate our resistance data to the limit of zero pillar cross-section, which corresponds to the uniform current density limit.† The result is shown in Fig. 5.17: the maximum resistivity ρ^*_{max} (corresponding to the maximum in the resistance at zero field) and

---

* Ferromagnetic coupling is indicated by the much smaller coercive field than that found for an uncoupled sample (with large Cu thickness).

† We showed in Ref. 125 and section 5.2 that the measured perpendicular resistance of a cylindrical Co/Cu pillar with radius r can be written as : $R = (t\,\rho^*\,r\,I_0(r/k))/(\pi r^2 2\,k\,I_1(r/k))$, with t the thickness of the multilayer, k the length scale on which the current density varies in the pillar, and ρ^* the perpendicular resistivity; $I_0(z)$ and $I_1(z)$ are modified Bessel functions of zeroth and first order, respectively.

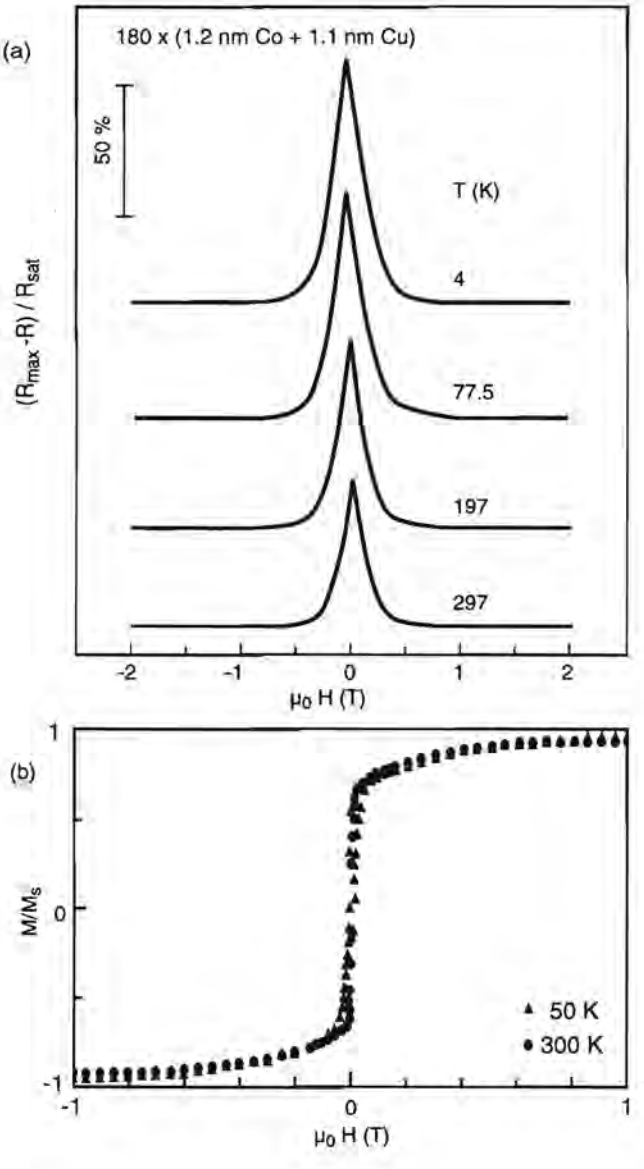

Figure 5.16. *(a) Giant magnetoresistance of a microstructured pillar in a 180×[Co(1.2 nm)+Cu(1.1 nm)] multilayer at different temperatures. (b) Magnetization curves at 50 and 300 K for the multilayer of (a).*

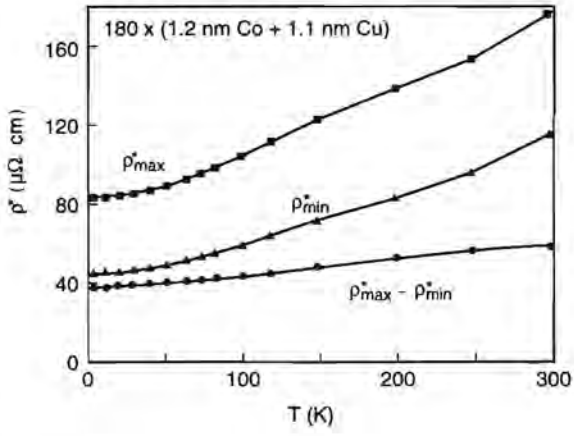

Figure 5.17. *Minimum resistivity ρ^*_{min} and maximum resistivity ρ^*_{max}, and the difference $\rho^*_{max} - \rho^*_{min}$, obtained from a comparison of CPP-MR data of pillar structures with variable cross sections with the current density model (see text). Solid lines are guides to the eye.*

the minimum resistivity ρ^*_{min} (corresponding to the minimum in the resistance at saturation) are shown as a function of temperature, together with the resistivity difference, $\rho^*_{max} - \rho^*_{min}$. With increasing temperature, both ρ^*_{max} and ρ^*_{min} increase due to electron-phonon and electron-magnon scattering processes, but, surprisingly, also the resistivity *difference* $\rho^*_{max} - \rho^*_{min}$ increases. This already suggests that the thermally induced scattering processes are spin-dependent, as will be discussed further. At 4.2 K, our absolute minimum resistivity is a factor 2.6 higher than the "intrinsic" resistivity of the multilayer used in our analysis, and is estimated from experiments by Pratt *et al.*, made on a comparable sample with superconducting contacts [43].*

* In Ref. 43, a minimum resistivity of 17 $\mu\Omega$ cm and a maximum resistivity of 44 $\mu\Omega$ cm was found for a 150×[Co(1.5 nm)+Cu(0.9 nm)] sample. It is expected that these are the intrinsic resistivity values of the multilayer, due to the use of superconducting contact leads. For our pillar structures we find that $\rho^*_{min} = 45\,\mu\Omega$ cm and $\rho^*_{max} = 83\,\mu\Omega$ cm. However, we expect the minimum "intrinsic" resistivity for both fabrication methods to be comparable. The observation that not only ρ^*_{min}, but also ρ^*_{max} has increased approximately by the same factor, indicates that there is no major serial contact resistance involved in our samples, but that the effective contact area on top of the pillar is smaller than expected. The origin for this most probably is a small contamination during the Au top-contact fabrication on the pillar [64, 126].

5.4.4 Discussion and conclusion

An explicit CPP-MR theory, taking into account spin-mixing and remaining valid at higher temperatures is not yet available. However, Fert and Campbell have proposed a model for the temperature dependence of the resistance of ferromagnetic alloys [11], which also may be applied to our CPP-MR data. This is possible, because the CPP MR of a magnetic multilayer is self-averaging [12], i.e., all scattering rates add up and are averaged over a length scale given by the spin flip diffusion length, which is much larger than individual layer thicknesses. This results in effective spin currents that are constant (but not necessarily equal) throughout the system, just as assumed in the alloy model (note that this is not the case for the CIP geometry). In the model, the total resistivity as a function of temperature is written as

$$\rho(T) = \frac{\rho_\uparrow(T)\rho_\downarrow(T) + \rho_{\uparrow\downarrow}(T)(\rho_\uparrow(T) + \rho_\downarrow(T))}{\rho_\uparrow(T) + \rho_\downarrow(T) + 4\,\rho_{\uparrow\downarrow}(T)}, \tag{5.17}$$

where $\rho_\sigma(T)$ is the resistivity for each spin σ and $\rho_{\uparrow\downarrow}(T)$ the spin-mixing resistivity, describing elastic spin-flip scattering processes, which tend to equalize the two spin currents. The significance of Eq. (5.17) for a multilayer is shown in Fig. 5.18 by two resistor schemes. Figure 5.18(a) illustrates the situation of two different spin-resistivities (assuming $\rho_\uparrow < \rho_\downarrow$), corresponding to the situation where magnetizations in the multilayer are aligned parallel. When $\rho_{\uparrow\downarrow}$ is infinite, we have two totally mixed spin-channels with the same resistivity; when $\rho_{\uparrow\downarrow}$ goes to zero, the situation corresponds to the usual two-current model with spin-dependent resistivities. Figure 5.18(b) corresponds with the situation where the magnetizations in the multilayer are aligned antiparallel. In this case, the individual spin-channels are already completely mixed; their resistivities are equal and given by the average of the two spin-resistivities in the ferromagnetic alignment case : $\rho_{AF} = \frac{1}{2}(\rho_\uparrow + \rho_\downarrow)$.

For determining the temperature dependence of the spin-dependent scattering from the experiments, we write $\rho_\sigma(T) = \rho_{0\sigma} + \rho_{i\sigma}(T)$, where $\rho_{0\sigma}$ is the low-temperature resistivity and $\rho_{i\sigma}(T)$ a temperature dependent contribution, originating from electron-phonon or intrachannel (non-spin-flip) electron-magnon scattering. The important spin-dependent scattering parameters are defined as $\alpha \equiv \rho_{0\downarrow}/\rho_{0\uparrow}$ and $\mu \equiv \rho_{i\downarrow}(T)/\rho_{i\uparrow}(T)$. In the limit that $\rho_{i\uparrow}, \rho_{i\downarrow}, \rho_{\uparrow\downarrow} \ll \rho_{0\uparrow}, \rho_{0\downarrow}$, Eq. (5.17) can be written as:

$$\rho(T) - \rho_0 = \left(1 + \frac{(\alpha-\mu)^2}{(1+\alpha)^2\,\mu}\right)\rho_i(T) + \frac{(\alpha-1)^2}{(\alpha+1)^2}\,\rho_{\uparrow\downarrow}(T), \tag{5.18}$$

with ${\rho_0}^{-1} \equiv \rho_{0\uparrow}^{-1} + \rho_{0\downarrow}^{-1}$ and ${\rho_i}^{-1} \equiv \rho_{i\uparrow}^{-1} + \rho_{i\downarrow}^{-1}$. One should bear in mind that the validity of Eq. (5.18) is roughly restricted to temperatures below about 100 K, where the limiting conditions leading to Eq. (5.18) are fulfilled. In the case that

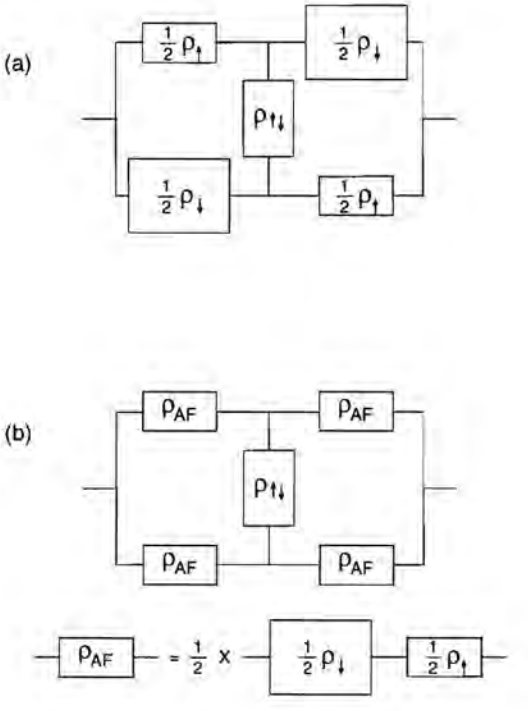

Figure 5.18. *Resistor scheme, corresponding with Eq. (5.17) and corresponding to a magnetic multilayer with (a) parallel aligned magnetizations and (b) antiparallel aligned magnetizations.*

the magnetizations in the multilayer are aligned parallel, the experimental minimum resistivity can, in principle, be directly compared with Eq. (5.18). The situation for the maximum resistivity is somewhat different. If the maximum resistivity corresponds to a completely AF-coupled situation, with the two spin channels having the same resistivity [see Fig. 5.18(b)], we must set $\alpha^{AF} = \mu^{AF} = 1$, and Eq. (5.18) is replaced by

$$(\rho(T) - \rho_0)^{AF} = (\rho_i(T))^{AF} = \frac{(1+\mu)}{4\mu}\,\rho_{i\downarrow}(T), \tag{5.19}$$

with $\rho_{i\downarrow}(T)$ the resistivity of the spin-down channel and μ the scattering asymmetry parameter in the *ferro*magnetic alignment configuration of the multilayer. We use the experimental minimum and maximum resistivities of Fig. 5.17 for comparison with Eqs. (5.18) and (5.19), respectively, with the condition that

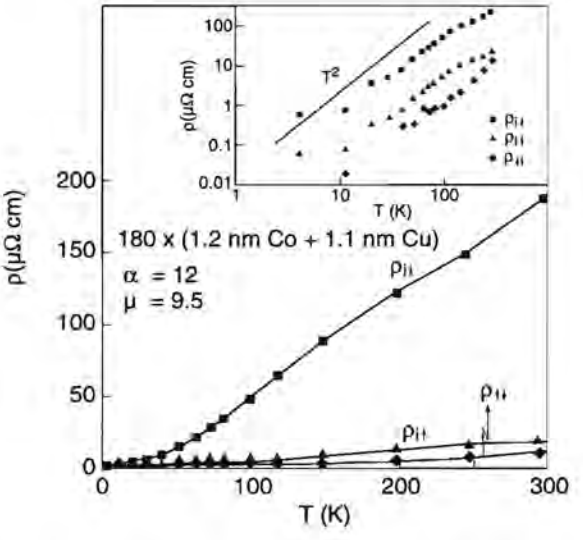

Figure 5.19. *Temperature dependent resistivities [$\rho_{\uparrow\downarrow}(T)$, $\rho_{\uparrow\uparrow}(T)$, and $\rho_{\uparrow\downarrow}(T)$], for a Co/Cu multilayer, determined from a comparison of experimental CPP-MR data with the Fert-Campbell theory. Full curves are guides to the eye.* **Inset:** *Temperature dependent resistivities on a double logarithmic scale. The temperature dependence is consistent with a T^2-behavior.*

$d\rho_{\uparrow\downarrow}(T)/dT = 0$ at the lowest temperatures.* The result is shown in Fig. 5.19. Prior to the analysis, the value for α is determined from a comparison of the CPP MR at 4.2 K with the (self-averaged) MR-model, where $MR = (1-\alpha)^2/(4\alpha)$ [Ref. 12 and sections 3.2 and 3.3; see also Eq. (3.27a)]. We find that $\alpha = 12$ for a perfectly AF-coupled sample, indicating the strong spin-dependent scattering at low temperatures.† Very striking is the large value for $\mu = 9.5$, which means that also the temperature dependent part of the resistivity is strongly spin-dependent. This number is in agreement with the result of Ref. 35, and not inconsistent with experiments on Co bulk alloys [127]. Qualitatively, we can understand this number, when we consider the *d*-band structure of Co. The spin-up *d*-band is completely filled, while the Fermi level is within the spin-down *d*-band. Raising the temperature only provides additional phase space for scattering of spin-down

* The experimental data have been recalculated, assuming complete AF-coupling in the sample. Without this procedure, values for the fitting parameters would be $\alpha = 5.5$ and $\mu = 10.1$.

† $\alpha = 12$ corresponds to a low-temperature CPP MR of 250%, a value of the same order as found in Ref. 43.

electrons (states within an energy range $k_B T$ around E_F), causing the spin-down scattering length to be much smaller than the spin-up scattering length. $\rho_{\uparrow\downarrow}$ is the smallest resistivity in the problem, indicating that momentum-conserving spin-flip scattering is not very important (note that $\rho_{\uparrow\downarrow} = 0$ corresponds with a situation without spin-mixing). This means that the usual two-current model with independent spin-currents might be a meaningful approximation, even at higher temperatures. When we plot the results on a double logarithmic scale, we find that the temperature dependence of the three resistivities below 100 K can be described by a T^2-law (see inset of Fig. 5.19). This seems reasonable for $\rho_{i\uparrow}(T)$ and $\rho_{i\downarrow}(T)$, which are determined by a combination of both electron-phonon and intrachannel electron-magnon scattering processes [11], whose contributions cannot be separated further.

The spin-mixing scattering rate $\tau_{\uparrow\downarrow}^{-1}$, originating from elastic interchannel electron-magnon scattering, has been microscopically modeled by Fert at low temperatures [128] as $\tau_{\uparrow\downarrow}^{-1} = F(T)\ (\mu_m^2 v_a k_F^3 (k_B T)^2)/(m^2 4\pi\hbar E_F)$ with μ_m the magnon effective mass, m the free electron mass, v_a the atomic volume, k_F and E_F the Fermi wave number and Fermi energy, respectively; $F(T)$ is a function which in the temperature regime of interest is close to 1. When taking $\mu_m/m = 11$ [129], and for the free-electron parameters of fcc Co $v_a = 1.12 \times 10^{-29}\,\mathrm{m}^3$, $k_F = 1.74 \times 10^{10}\,\mathrm{m}^{-1}$ and $E_F = 5.6\,\mathrm{eV}$, we find that $\tau_{\uparrow\downarrow}^{-1} = 1.15 \times 10^9\,[\mathrm{s}^{-1}\,\mathrm{K}^{-2}]\,T^2$. Taking for the multilayer the product $\rho\,\tau = 3.0 \times 10^{-22}\,\Omega\,\mathrm{m\,s}$, we find the theoretical value for the resistivity $\rho_{\uparrow\downarrow}/T^2 = 3.4 \times 10^{-13}\,[\Omega\,\mathrm{m\,K}^{-2}]$. Our experimental result is $\rho_{\uparrow\downarrow}/T^2 = 1.0 \times 10^{-12}\,[\Omega\,\mathrm{m\,K}^{-2}]$, which is a factor of three larger. This is in satisfactory agreement, considering the uncertainties in deriving the parameters above. For the spin-flip diffusion length associated with this spin-flip scattering time, we find that $(D\,\tau_{\uparrow\downarrow})^{1/2} = 50\,\mathrm{nm}$ at 100 K, for a typical metallic diffusion constant $D = 10^{-2}\,\mathrm{m}^2/\mathrm{s}$. This long length is consistent with the relatively small value of $\rho_{\uparrow\downarrow}$. The latter, together with the large value for μ is the basic explanation for the relatively weak temperature dependence of the MR of Co/Cu.*

In conclusion, we have fabricated pillar structures in MBE-grown Co/Cu magnetic multilayers and studied the CPP-MR effect from 4 K up to room temperature. We have argued that the model of Fert and Campbell for the temperature dependence of the resistivity of magnetic alloys can be used to analyze our experimental data, because of the self-averaging character of the CPP geometry. We have found that the temperature dependent part of the resistivity is strongly spin-dependent : $\mu \equiv \rho_{i\downarrow}(T)/\rho_{i\uparrow}(T) \approx 10$ and that spin-flip scattering is relatively weak, in agreement with theory. The large μ-value and the small $\rho_{\uparrow\downarrow}$ fundamentally explains the weak temperature dependence of the CPP MR of Co/Cu.

---

* Applying the same analysis to Fe/Cr magnetic multilayers, where the CPP MR strongly decreases with increasing temperature (see Refs. 64, 126 and section 5.3), we find a value for $\mu = 2.2$.

References

[1] M. N. Baibich, J. M. Broto, A. Fert, F. Nguyen Van Dau, F. Petroff, P. Etienne, G. Creuzet, A. Friederich, and J. Chazelas, Phys. Rev. Lett. **61**, 2472 (1988).

[2] B. Dieny, V. S. Speriosu, S. Metin, S. S. P. Parkin, B. A. Gurney, P. Baumgart, and D. R. Wilhoit, J. Appl. Phys. **69**, 4774 (1991).

[3] A. Chaiken, P. Lubitz, J. J. Krebs, G. A. Prinz, and M. Z. Harford, Appl. Phys. Lett. **59**, 240 (1991).

[4] H. Yamamoto, Y. Motomura, T. Anno, and T. Shinjo, J. Magn. Magn. Mater. **126**, 437 (1993).

[5] Q. Yang, P. Holody, R. Loloee, L. L. Henry, W. P. Pratt, Jr., P. A. Schroeder, and J. Bass, Phys. Rev. B **51**, 3226 (1995).

[6] P. Xiong, G. Xiao, J. Q. Wang, J. Q. Xiao, J. S. Jiang, and C. L. Chien, Phys. Rev. Lett. **69**, 3220 (1992).

[7] M. J. Carey, A. P. Young, A. Starr, D. Rao, and A. E. Berkowitz, Appl. Phys. Lett. **61**, 2935 (1992).

[8] T. L. Hylton, Appl. Phys. Lett. **62**, 2431 (1993).

[9] T. L. Hylton, K. R. Coffey, M. A. Parker, and J. K. Howard, Science **261**, 1021 (1993).

[10] P. Holody, L. B. Steren, R. Morel, A. Fert, R. Loloee, and P. A. Schroeder, Phys. Rev. B **50**, 12999 (1994).

[11] A. Fert and I. A. Campbell, J. Phys. F: Met. Phys. **6**, 849 (1976).

[12] T. Valet and A. Fert, Phys. Rev. B **48**, 7099 (1993).

[13] W. P. Pratt, Jr., S.-F. Lee, J. M. Slaughter, R. Loloee, P. A. Schroeder, and J. Bass, Phys. Rev. Lett. **66**, 3060 (1991).

[14] T. M. Whitney, J. S. Jiang, P. C. Searson, and C. L. Chien, Science **261**, 1316 (1993).

[15] A. Blondel, J. P. Meier, B. Doudin, and J.-P. Ansermet, Appl. Phys. Lett. **65**, 3019 (1994).

[16] L. Piraux, J. M. George, J. F. Despres, C. Leroy, E. Ferain, R. Legras, K. Ounadjela, and A. Fert, Appl. Phys. Lett. **65**, 2484 (1994).

[17] P. J. H. Bloemen, *Metallic Multilayers: Experimental Investigation of Magnetic Anisotropy and Magnetic Interlayer Coupling*, Ph.D. thesis, Eindhoven University of Technology, 1993.

[18] W. B. Zeper, *Magneto-Optical Recording Media Based on Co/Pt Multilayers*, Ph.D. thesis, Twente University of Technology, 1991.

[19] P. Beliën, R. Schad, C. D. Potter, G. Verbanck, V. V. Moshchalkov, and Y. Bruynseraede, Phys. Rev. B **50**, 9957 (1994).

[20] A. Segmüller and A. E. Blakeslee, J. Appl. Cryst. **6**, 19 (1973).

[21] S. Foner, Rev. Sci. Instrum. **30**, 548 (1959).
[22] J. P. C. Bernards and C. P. G. Schrauwen, *Co-Cr layers for perpendicular magnetic recording*, Ph.D. thesis, Twente University of Technology, 1990.
[23] L. J. van der Pauw, Philips Res. Rep. **13**, 1 (1958).
[24] P. M. Levy, *Giant Magnetoresistance in Magnetic Layered and Granular Materials*, vol. 47 of *Solid State Physics* (1995) pp. 367–462.
[25] M. A. M. Gijs, *Experiments on the Perpendicular Giant Magnetoresistance in Magnetic Multilayers*, Springer Series in Material Sciences: Magnetic Thin Films and Industrial Applications (Springer, 1995) chapter 4, *to be published.*
[26] K. Fuchs, Proc. Cambridge Philos. Soc. **34**, 100 (1938).
[27] E. H. Sondheimer, Adv. Phys. **1**, 1 (1952).
[28] R. E. Camley and J. Barnaś, Phys. Rev. Lett. **63**, 664 (1989).
[29] J. Barnaś, A. Fuss, R. E. Camley, P. Grünberg, and W. Zinn, Phys. Rev. B **42**, 8110 (1990).
[30] A. Barthélémy and A. Fert, Phys. Rev. B **43**, 13124 (1991).
[31] B. L. Johnson and R. E. Camley, Phys. Rev. B **44**, 9997 (1991).
[32] B. Dieny, Europhys. Lett. **17**, 261 (1992).
[33] T. G. S. M. Rijks, R. Coehoorn, and W. J. M. de Jonge, Mat. Res. Soc. Symp. Proc. Vol. **313**, 283 (1993).
[34] L. M. Falicov and R. Q. Hood, J. Magn. Magn. Mater. **121**, 362 (1993).
[35] J. L. Duvail, A. Fert, L. G. Pereira, and D. K. Lottis, J. Appl. Phys. **75**, 7070 (1994).
[36] P. M. Levy and S. Zhang, J. Magn. Magn. Mater. **93**, 67 (1991).
[37] S. Zhang, P. M. Levy, and A. Fert, Phys. Rev. B **45**, 8689 (1992).
[38] P. M. Levy, S. Zhang, and A. Fert, Phys. Rev. Lett. **65**, 1643 (1990).
[39] T. Valet and A. Fert, J. Magn. Magn. Mater. **121**, 378 (1993).
[40] M. Johnson and R. H. Silsbee, Phys. Rev. B **35**, 4959 (1987).
[41] P. C. van Son, H. van Kempen, and P. Wyder, Phys. Rev. Lett. **58**, 2271 (1987); *comment and reply* **60**, 377 (1988).
[42] M. Johnson, Phys. Rev. Lett. **67**, 3594 (1991).
[43] W. P. Pratt, Jr., S.-F. Lee, P. Holody, Q. Yang, R. Loloee, J. Bass, and P. A. Schroeder, J. Magn. Magn. Mater. **126**, 406 (1993).
[44] S.-F. Lee, W. P. Pratt, Jr., Q. Yang, P. Holody, R. Loloee, P. A. Schroeder, and J. Bass, J. Magn. Magn. Mater. **118**, L1 (1993).
[45] P. A. Schroeder, J. Bass, P. Holody, S.-F. Lee, R. Loloee, W. P. Pratt, Jr., and Q. Yang, in *Magnetism and Structure in Systems of Reduced Dimension*, Vol. 309 of *NATO Advanced Study Institute, Series B: Physics* edited by R. F. C. Farrow *et al.* (Plenum, New York, 1993), p. 129.
[46] J. Bass, Q. Yang, S.-F. Lee, P. Holody, R. Loloee, P. A. Schroeder, and W. P. Pratt, Jr., J. Appl. Phys. **75**, 6699 (1994).
[47] P. A. Schroeder, J. Bass, P. Holody, S.-F. Lee, R. Loloee, W. P. Pratt, Jr., and Q. Yang, Mat. Res. Soc. Symp. Proc. Vol. **313**, 47 (1993).
[48] M. A. M. Gijs, M. T. Johnson, A. Reinders, P. E. Huisman, R. J. M. van de Veerdonk, S. K. J. Lenczowski, and R. M. J. van Gansewinkel, Appl. Phys. Lett. **66**, 1839 (1995).

[49] G. D. Mahan, *Many-Particle Physics* (Plenum, New York, 1986).
[50] H. E. Camblong, S. Zhang, and P. M. Levy, Phys. Rev. B **47**, 4735 (1993).
[51] G. E. W. Bauer, Phys. Rev. Lett. **69**, 1676 (1992); *erratum* **70**, 1733 (1993).
[52] G. E. W. Bauer, M. A. M. Gijs, S. K. J. Lenczowski, and J. B. Giesbers, J. Magn. Magn. Mater. **126**, 454 (1993).
[53] A. Brataas and G. E. W. Bauer, Europhys. Lett. **2**, 117 (1994).
[54] A. Brataas and G. E. W. Bauer, Phys. Rev. B **49**, 14684 (1994).
[55] R. Landauer, Z. Phys. B **68**, 217 (1987).
[56] G. W. Bauer, A. Brataas, C. M. Schep, and P. J. Kelly, J. Appl. Phys. **75**, 6704 (1994).
[57] K. M. Schep, P. J. Kelly, and G. E. W. Bauer, Phys. Rev. Lett. **74**, 586 (1995).
[58] K. M. Schep, P. J. Kelly, and G. E. W. Bauer, Mat. Res. Soc. Symp. Proc. Vol. (1995), *to be published.*
[59] J. A. C. Bland and B. Heinrich, eds., *Ultrathin Magnetic Structures I and II* (Springer, Berlin Heidelberg, 1994).
[60] M. Alper, K. Attenborough, V. Baryshev, R. Hart, D. S. Lashmore, and W. Schwarzacher, J. Appl. Phys. **75**, 6543 (1994).
[61] M. Alper, K. Attenborough, R. Hart, S. J. Lane, D. S. Lashmore, C. Younes, and W. Schwarzacher, Appl. Phys. Lett. **15**, 2144 (1993).
[62] S. Z. Hua, D. S. Lashmore, L. Salamanca-Riba, W. Schwarzacher, L. J. Swartzendruber, R. D. McMichael, L. H. Bennett, and R. Hart, J. Appl. Phys. **76**, 6519 (1994).
[63] C. A. Ross, Annu. Rev. Mater. Sci **24**, 159 (1994).
[64] M. A. M. Gijs, S. K. J. Lenczowski, and J. B. Giesbers, Phys. Rev. Lett. **70**, 3343 (1993).
[65] M. A. M. Gijs, J. B. Giesbers, S. K. J. Lenczowski, and H. H. J. M. Janssen, Appl. Phys. Lett. **63**, 111 (1993).
[66] L. H. Bennett, L. J. Swartzendruber, D. S. Lashmore, R. Oberle, U. Atzmony, M. P. Dariel, and R. E. Watson, Phys. Rev. B **40**, 4633 (1989).
[67] R. D. McMichael, U. Atzmony, C. Beauchamp, L. H. Bennett, L. J. Swartzendruber, D. S. Lashmore, and L. T. Romankiw, J. Magn. Magn. Mater. **113**, 149 (1992).
[68] M. Alper, P. S. Aplin, K. Attenborough, D. J. Dingley, R. Hart, S. J. Lane, D. S. Lashmore, and W. Schwarzacher, J. Magn. Magn. Mater. **126**, 8 (1993).
[69] D. M. Tench and J. T. White, Mater. Trans. **15A**, 2039 (1984).
[70] J. Yahalom and O. Zadok, J. Mater. Sci. **22**, 499 (1987).
[71] L. H. Bennett, D. S. Lashmore, M. P. Dariel, M. J. Kaufman, M. Rubinstein, P. Lubitz, O. Zadok, and J. Yahalom, J. Magn. Magn. Mater. **67**, 239 (1987).
[72] V. M. Fedosyuk, O. I. Kasyutich, and N. N. Kozich, J. Mater. Chem. **1**, 795 (1991).
[73] D. S. Lashmore, R. Oberle, M. P. Dariel, L. H. Bennett, and L. Swartzendruber, Mat. Res. Soc. Symp. Proc. Vol. **132**, 219 (1989).
[74] F. A. Lowenheim, ed., *Modern Electroplating* (Wiley, New York, 1974).
[75] T. R. McGuire and R. I. Potter, IEEE Trans. Magn. **MAG–11**, 1018 (1975).
[76] S. Chikazumi and S. H. Charap, *Physics of Magnetism*, reprint edition (Krieger,

Malabar, 1978).
[77] S. K. J. Lenczowski, M. A. M. Gijs, J. B. Giesbers, R. J. M. van de Veerdonk, and W. J. M. de Jonge, Phys. Rev. B **50**, 9982 (1994).
[78] E. A. M. van Alphen and W. J. M. de Jonge, Phys. Rev. B **51**, 8182 (1995).
[79] *Proceedings of the International Symposium on Magnetic Ultrathin Films, Multilayers and Surfaces*, 7-10 September 1992, Lyon [J. Magn. Magn. Mater. **121**(1-3) (1993)].
[80] *Magnetic Ultrathin Films: Multilayers and Surfaces, Interfaces and Characterization*, MRS Symposium Proceedings Volume 313 edited by B. T. Jonker *et al.* (Materials Research Society, Pittsburgh, 1993).
[81] *Proceedings of the MMM Conference*, 15-19 November 1993, Minneapolis [J. Appl. Phys. **75**(10-II) (1994)].
[82] B. Dieny, J. Phys. Condens. Matter **4**, 8009 (1992).
[83] B. Dieny, V. S. Speriosu, J. P. Nozières, B. A. Gurney, A. Vedyayev, and N. Ryzhanova, in *Magnetism and Structure in Systems of Reduced Dimension*, Vol. 309 of *NATO Advanced Study Institute, Series B: Physics* edited by R. F. C. Farrow *et al.* (Plenum, New York, 1993), p. 279.
[84] M. A. M. Gijs and M. Okada, Phys. Rev. B **46**, 2908 (1992).
[85] M. A. M. Gijs and M. Okada, J. Magn. Magn. Mater. **113**, 105 (1992).
[86] R. Coehoorn, A. De Veirman, and J. P. W. B. Duchateau, J. Magn. Magn. Mater. **121**, 266 (1993).
[87] R. Coehoorn and J. P. W. B. Duchateau, J. Magn. Magn. Mater. **126**, 390 (1993).
[88] R. Coehoorn, M. T. Johnson, W. Folkerts, S. T. Purcell, N. W. E. McGee, A. De Veirman, and P. J. H. Bloemen, in *Magnetism and Structure in Systems of Reduced Dimension*, Vol. 309 of *NATO Advanced Study Institute, Series B: Physics* edited by R. F. C. Farrow *et al.* (Plenum, New York, 1993), p. 295.
[89] D. H. Mosca, F. Petroff, A. Fert, P. A. Schroeder, W. P. Pratt, Jr., and R. Loloee, J. Magn. Magn. Mater. **94**, L1 (1991).
[90] M. T. Johnson, S. T. Purcell, N. W. E. McGee, R. Coehoorn, J. aan de Stegge, and W. Hoving, Phys. Rev. Lett. **68**, 2688 (1992).
[91] P. J. H. Bloemen, R. van Dalen, W. J. M. de Jonge, M. T. Johnson, and J. aan de Stegge, J. Appl. Phys. **73**, 5972 (1993).
[92] F. Giron, P. Boher, P. Houdy, P. Beauvillain, K. Le Dang, and P. Veillet, J. Magn. Magn. Mater. **121**, 318 (1993).
[93] E. E. Fullerton, D. M. Kelly, J. Guimpel, I. K. Schuller, and Y. Bruynseraede, Phys. Rev. Lett. **68**, 859 (1992).
[94] E. E. Fullerton, M. J. Conover, J. E. Mattson, C. H. Sowers, and S. D. Bader, Phys. Rev. B **48**, 15755 (1993).
[95] R. J. Highmore, J. E. Evetts, and R. E. Somekh, J. Magn. Magn. Mater. **123**, L13 (1993).
[96] G. Rupp and K. Schuster, J. Magn. Magn. Mater. **121**, 416 (1993).
[97] H. A. M. van den Berg and G. Rupp, IEEE Trans. Magn. **30**, 809 (1994).
[98] B. Dieny, J. P. Gavigan, and J. P. Rebouillat, J. Phys. Condens. Matter **2**, 159 (1990).
[99] B. Dieny and J. P. Gavigan, J. Phys. Condens. Matter **2**, 187 (1990).

[100] W. Folkerts, J. Magn. Magn. Mater. **94**, 302 (1991).
[101] R. Coehoorn (private communication).
[102] S. S. P. Parkin, R. Bhadra, and K. P. Roche, Phys. Rev. Lett. **66**, 2152 (1991).
[103] S. S. P. Parkin, Z. G. Li, and D. J. Smith, Appl. Phys. Lett. **58**, 2710 (1991).
[104] S. Zhang and P. M. Levy, Phys. Rev. B **47**, 6776 (1993).
[105] W. P. Pratt, Jr., S.-F. Lee, Q. Yang, P. Holody, R. Loloee, P. A. Schroeder, and J. Bass, J. Appl. Phys. **73**, 5326 (1993).
[106] S. S. P. Parkin, Phys. Rev. Lett. **71**, 1641 (1993).
[107] S. S. P. Parkin, Appl. Phys. Lett. **61**, 1358 (1992).
[108] V. S. Speriosu, J. P. Nozières, B. A. Gurney, B. Dieny, T. C. Huang, and H. Lefakis, Phys. Rev. B **47**, 11579 (1993).
[109] T. G. S. M. Rijks, R. L. H. Sour, D. G. Neerinck, A. E. M. De Veirman, R. Coehoorn, J. C. S. Kools, M. F. Gillies, and W. J. M. de Jonge, IEEE Trans. Magn. (1995), *to be published.*
[110] T. R. Werner, I. Banerjee, Q. S. Yang, C. M. Falco, and I. K. Schuller, Phys. Rev. B **26**, 2224 (1983).
[111] T. Y. Hsiang and J. Clarke, Phys. Rev. B **21**, 945 (1980).
[112] S. Zhang and P. M. Levy, J. Appl. Phys. **69**, 4786 (1991).
[113] S.-F. Lee, W. P. Pratt, Jr., R. Loloee, P. A. Schroeder, and J. Bass, Phys. Rev. B **46**, 548 (1992).
[114] W. Vavra, S. F. Cheng, A. Fink, J. J. Krebs, and G. A. Prinz, Appl. Phys. Lett. **66**, 2579 (1995).
[115] TOSCA *reference manual*, Internal Report VF-11-92-14, Vector Fields Ltd, 1992.
[116] G. Binasch, P. Grünberg, F. Saurenbach, and W. Zinn, Phys. Rev. B **39**, 4828 (1989).
[117] S. S. P. Parkin, N. More, and K. P. Roche, Phys. Rev. Lett. **64**, 2304 (1990).
[118] B. Dieny, V. S. Speriosu, S. S. P. Parkin, B. A. Gurney, D. R. Wilhoit, and D. Mauri, Phys. Rev. B **43**, 1297 (1991).
[119] M. A. M. Gijs, R. M. Wolf, T. van Rooy, A. M. Gerrits, M. E. Bijlsma, and A. Gilabert, Solid State Commun. **80**, 727 (1991).
[120] M. A. M. Gijs, J. B. Giesbers, M. T. Johnson, J. B. F. aan de Stegge, H. H. J. M. Janssen, S. K. J. Lenczowski, R. J. M. van de Veerdonk, and W. J. M. de Jonge, J. Appl. Phys. **75**, 6709 (1994).
[121] M. A. M. Gijs, S. K. J. Lenczowski, R. J. M. van de Veerdonk, J. B. Giesbers, M. T. Johnson, and J. B. F. aan de Stegge, Phys. Rev. B **50**, 16733 (1994).
[122] J. C. Slonczewski, Phys. Rev. B **39**, 6995 (1989).
[123] D. L. Mills, A. Fert, and I. A. Campbell, Phys. Rev. B **4**, 196 (1971).
[124] J. E. Mattson, M. E. Brubaker, C. H. Sowers, M. Conover, Z. Qiu, and S. D. Bader, Phys. Rev. B **44**, 9378 (1991).
[125] S. K. J. Lenczowski, R. J. M. van de Veerdonk, M. A. M. Gijs, J. B. Giesbers, and H. H. J. M. Janssen, J. Appl. Phys. **75**, 5154 (1994).
[126] M. A. M. Gijs, S. K. J. Lenczowski, and J. B. Giesbers, Mat. Res. Soc. Symp. Proc. Vol. **313**, 11 (1993).
[127] B. Loegel and F. Gautier, J. Phys. Chem. Sol. **32**, 2723 (1971).
[128] A. Fert, J. Phys. C: Solid State Phys. **2**, 1784 (1969).

[129] G. Shirane, V. J. Minkiewicz, and R. Nathans, J. Appl. Phys. **39**, 383 (1968).

Summary

This thesis reports on an experimental study of the giant magnetoresistance effect in magnetic multilayers. Magnetic multilayers consist, in their simplest form, of an alternate stacking of magnetic and nonmagnetic layers. Nowadays it is possible by various techniques to deposit layers with thicknesses of only a few atomic planes in a very controlled way. This has opened an immense new area for fundamental materials research as well as for more application driven studies. The giant magnetoresistance effect is one of the novel phenomena discovered in these artificial structures and the main subject of the present work.

After an introduction in chapter 1 and a survey of the most important fabrication and analysis techniques in chapter 2, a brief introduction to the theoretical background of the giant magnetoresistance effect is presented in chapter 3. The emphasis is laid on those models developed in literature, which have been used to describe or extract useful empirical parameters from the experimental data reported in this thesis. Differences between the current-in-plane (CIP) geometry where the measuring current is flowing parallel to the planes of the multilayer stacking, and the current-perpendicular- to-plane (CPP) geometry with the current perpendicular to the planes, thereby necessarily passing each interface between the various magnetic and nonmagnetic layers, are addressed.

Chapter 4 contains the results of CIP magnetoresistance experiments on high-vacuum sputtered Co/Cu and $Ni_{80}Fe_{20}$/Cu multilayers. The main goal of these experiments was to determine the spin-asymmetry parameters of the scattering processes within the bulk of the magnetic layers and at the interfaces between the magnetic and nonmagnetic layers. To quantify these spin-asymmetry parameters, we analyzed the CIP magnetoresistance data in terms of the magnetoresistance model of Levy, Zhang, and Fert. Growth quality and orientation, multilayer period, and texture were checked by means of X-ray diffraction measurements. Magnetization measurements were performed to determine the coupling strength and anisotropy constants, as well as to correct for incomplete antiparallel alignment around zero applied magnetic field. Within this framework, we have found strong evidence that for both Co/Cu and $Ni_{80}Fe_{20}$/Cu multilayers the spin dependence of the interface scattering is the main cause for the observed large magnetoresistance values; the spin dependence of the bulk scattering is relatively small, but not zero.

Another part of chapter 4 is devoted to an alternative, relatively simple and cheap method to deposit metallic multilayered structures, which is electrochemical deposition. It appeared possible to grow high-quality Co/Cu multilayers in a

single electrolyte containing both Co^{2+} and Cu^{2+} ions. Using X-ray fluorescence analysis, layer thicknesses were carefully calibrated. Up to now, no indications for antiferromagnetic coupling could be found for the appropriate Cu spacers below ≈ 30 Å. In this thickness regime mainly the anisotropic magnetoresistance effect was measured. In the uncoupled regime, however, for spacer layer thicknesses above ≈ 30 Å, giant magnetoresistance effects up to 14% at room temperature were achieved. It was demonstrated that the choice of the Cu^{2+} concentration is crucial for obtaining large magnetoresistance values and high-quality Co layers and Co/Cu interfaces. The addition of commonly used brighteners to the electrolyte was found to have a catastrophic effect on both the structural quality of the multilayers as well as on the magnitude of the magnetoresistance.

In chapter 5 the CPP magnetoresistance experiments are described. For this purpose small pillar-like structures of micron size were made in metallic magnetic multilayers using optical lithography and reactive ion etching techniques. A new contact geometry was proposed for an accurate measurement of the very small perpendicular resistance, which excludes any spurious contributions from the much larger resistance of the contact leads. Furthermore, a relatively simple Ohmic model was developed to calculate the current distribution in the pillars. These calculations appeared consistent with three-dimensional electrostatic simulations based on the finite element method, and were used to explain the area dependence of the perpendicular pillar resistance and to extract the real pillar resistivity. With these "tools" the CPP magnetoresistance of, in this case, Fe/Cr multilayers was measured for the first time from 4.2 K up to room temperature. Indeed the CPP magnetoresistance was larger than the corresponding CIP magnetoresistance. At Cr thicknesses corresponding to the first antiferromagnetic coupling peak for instance, we found a CPP magnetoresistance of 108% at 9.3 K, which is more than four times higher than for the CIP case. The temperature dependence of the CPP magnetoresistance was interpreted in terms of thermally excited magnons.

In a more elaborate study on the temperature dependence of the CPP magnetoresistance of Co/Cu multilayers, we analyzed the data using a resistance model originally proposed for magnetic alloys. Within this framework it was found that the temperature-dependent scattering rates in Co/Cu multilayers are strongly spin dependent, while the spin-mixing scattering rate remains small up to relatively high temperatures. These features give an explanation for the weak decrease with temperature of the magnetoresistance effect in Co/Cu multilayers as compared to Fe/Cr superlattices.

Samenvatting

In dit proefschrift worden de resultaten beschreven van een experimentele studie naar het zogenaamde reuze magnetoweerstandeffect in magnetische multilagen. In hun meest eenvoudige vorm bestaan magnetische multilagen uit een stapeling van afwisselend magnetische en niet-magnetische lagen. Met behulp van verschillende technieken kunnen tegenwoordig op gecontroleerde wijze zeer dunne lagen gegroeid worden met een dikte die overeenkomt met slechts enkele atoomvlakken. Dit heeft geleid tot de ontdekking van een aantal nieuwe fenomenen in deze artificiële structuren, die zowel vanuit fundamenteel fysisch oogpunt, als vanwege de toepassingsmogelijkheden in magnetische recording erg interessant zijn. Het reuze magnetoweerstandeffect is een van deze fenomenen en het belangrijkste onderwerp van dit werk.

Na een inleiding in hoofdstuk 1, volgen in hoofdstuk 2 een overzicht van de voor dit werk meest belangrijke groei- en analysetechnieken, alsmede een beschrijving van het microfabricageproces, dat gebruikt is om kleine pilaarstructuren in magnetische multilagen te maken. Hoofdstuk 3 bevat een korte introductie in de theoretische achtergronden van het reuze magnetoweerstandeffect. De nadruk ligt op díe in de literatuur ontwikkelde modellen, die gebruikt zijn om waardevolle empirische parameters te bepalen uit de experimenten waarover in dit proefschrift gerapporteerd wordt. De verschillen tussen de twee meetsituaties, waarbij enerzijds de stroom parallel aan het vlak van de lagen stroomt (de CIP-geometrie), en anderzijds loodrecht op het vlak van de lagen (de CPP-geometrie), worden belicht.

De CIP magnetoweerstandexperimenten worden beschreven in hoofdstuk 4. Het belangrijkste doel van deze experimenten aan hoog-vacuüm gesputterde Co/Cu en $Ni_{80}Fe_{20}$/Cu multilagen was het bepalen van spin-asymmetrie voor de verstrooiingsprocessen in de bulk van de magnetische lagen en aan de grensvlakken tussen de magnetische en niet-magnetische lagen. Hiertoe zijn de CIP magnetoweerstandmetingen geanalyseerd in termen van het magnetoweerstandmodel van Levy, Zhang en Fert. De groeikwaliteit, multilaagperiode en textuur zijn gecontroleerd met behulp van Röntgendiffractie experimenten. Magnetisatiemetingen zijn uitgevoerd ter bepaling van de sterkte van de magnetische tussenlaagkoppeling en de anisotropieconstanten. Tevens zijn de magnetisatiemetingen gebruikt om te kunnen corrigeren voor een onvolledige antiparallelle oriëntatie van de magnetisaties van de opeenvolgende magnetische lagen bij afwezigheid van een magnetisch veld. Binnen dit raamwerk hebben we sterke aanwijzingen gevonden, dat voor zowel Co/Cu als voor $Ni_{80}Fe_{20}$/Cu multilagen de

spinafhankelijkheid van de grensvlakverstrooiing de belangrijkste oorzaak voor de hoge magnetoweerstandwaarden is; de spinafhankelijkheid van de bulkverstrooiing is relatief klein, maar niet verwaarloosbaar.

Een ander gedeelte van hoofdstuk 4 is gewijd aan elektrochemische depositie van multilagen. Elektro-depositie is een alternatieve, relatief eenvoudige en goedkope methode om metallische multilagen te groeien, volgens welke het mogelijk is gebleken om Co/Cu *multi*lagen van hoge kwaliteit te laten neerslaan vanuit *een* elektrolyt, waarin zowel Co^{2+}- als Cu^{2+}-ionen zijn opgelost. Aan de hand van Röntgenfluorescentie analyse zijn de laagdiktes zorgvuldig gekalibreerd. Er zijn nog geen indicaties gevonden voor een antiferromagnetische (AF) koppeling bij Cu tussenlaagdiktes kleiner dan ongeveer 30 Å, waar men op grond van literatuurgegevens AF-koppeling moet verwachten. Magnetoweerstandmetingen aan multilagen met deze Cu tussenlaagdiktes geven voornamelijk het anisotrope magnetoweerstandeffect te zien. Voor grotere Cu tussenlaagdiktes echter (> 30 Å), in het zogenaamde niet-gekoppelde gebied, zijn magnetoweerstandeffecten van 14% bij kamertemperatuur gemeten. We hebben aangetoond dat een juiste Cu^{2+}-concentratie in het elektrolyt essentieel is voor het groeien van Co-lagen en Co/Cu-grensvlakken van voldoende kwaliteit om deze hoge magnetoweerstandwaarden te kunnen verkrijgen. Het is gebleken dat de toevoeging van veelal gebruikte glansmiddelen aan het elektrolyt een desastreus effect heeft op zowel de structurele kwaliteit van de multilagen, als op de grootte van de gemeten magnetoweerstandwaarden.

In hoofdstuk 5 worden de CPP magnetoweerstandexperimenten beschreven. Hiertoe zijn met behulp van optische lithografie en reactieve-ionen-etstechnieken kleine pilaarachtige structuren in metallische multilagen gefabriceerd ter grootte van enkele micrometers. Een nieuwe contactgeometrie is ontwikkeld om de zeer kleine loodrechte weerstand te kunnen meten zonder de storende invloed van de veel grotere weerstand van de contacten en de toevoerdraden. Daarnaast is er een relatief eenvoudig model opgesteld om de stroomdichtheidsverdeling in de pilaren te berekenen. Deze berekeningen zijn consistent met drie-dimensionale elektrostatische simulaties op basis van de eindige-elementen methode en kunnen gebruikt worden om de intrinsieke loodrechte resistiviteit van de pilaren te bepalen. Met behulp van deze pilaren kon voor het eerst de CPP magnetoweerstand van, in dit geval, Fe/Cr multilagen gemeten worden van 4.2 K tot kamertemperatuur. De CPP magnetoweerstand bleek inderdaad groter te zijn dan de corresponderende CIP magnetoweerstand. Voor Cr tussenlaagdiktes overeenkomend met de eerste antiferromagnetische koppelingspiek bijvoorbeeld, is een CPP magnetoweerstandeffect ter grootte van 108% bij 9.3 K gemeten, meer dan vier maal zo hoog als voor de CIP geometrie. De temperatuurafhankelijkheid van de CPP magnetoweerstand is geïnterpreteerd in termen van thermisch geactiveerde magnonen.

In een meer gedetailleerde studie naar de temperatuurafhankelijkheid van de CPP magnetoweerstand van Co/Cu multilagen, zijn de meetgegevens geana-

lyseerd aan de hand van een weerstandmodel van Fert en Campbell, dat oorspronkelijk ontwikkeld was voor magnetische legeringen. In dit kader hebben we geconcludeerd dat de door de temperatuur geïnduceerde verstrooiingsprocessen in Co/Cu multilagen in hoge mate spinafhankelijk zijn, terwijl de bijdrage van de spinmengingsweerstand klein blijft tot relatief hoge temperaturen. Deze bevindingen geven een verklaring voor matige temperatuurafhankelijkheid van de magnetoweerstand in Co/Cu multilagen vergeleken met Fe/Cr multilagen.

Bibliography of the Author

- **Giant magnetoresistance of electrodeposited Co/Cu multilayers**
  S. K. J. Lenczowski, C. Schönenberger, M. A. M. Gijs, and W. J. M. de Jonge,
  Journal of Magnetism and Magnetic Materials **148**, 455 (1995).

- **Perpendicular giant magnetoresistance of Co/Cu multilayers deposited under an angle on grooved substrates**
  M. A. M. Gijs, M. T. Johnson, A. Reinders, P. E. Huisman, R. J. M. van de Veerdonk, S. K. J. Lenczowski, and R. M. J. van Gansewinkel,
  Applied Physics Letters **66**, 1839 (1995).

- **Temperature dependence of the spin-dependent scattering in Co/Cu multilayers determined from perpendicular-giant-magnetoresistance experiments**
  M. A. M. Gijs, S. K. J. Lenczowski, R. J. M. van de Veerdonk, J. B. Giesbers, M. T. Johnson, and J. B. F. aan de Stegge,
  Physical Review B **50**, 16733 (1994).

- **Strong Mn-Mn distance dependence of the Mn interlayer coupling in $SmMn_2Ge_2$-related compounds and its role in magnetic phase transitions**
  J. H. V. J. Brabers, A. J. Nolten, F. Kayzel, S. K. J. Lenczowski, K. H. J. Buschow, and F. R. de Boer,
  Physical Review B **50**, 16410 (1994).

- **Interpretation of the giant magnetoresistance effect in Co/Cu(100) multilayers with the quantum model of giant magnetoresistance**
  S. K. J. Lenczowski, M. A. M. Gijs, J. B. Giesbers, R. J. M. van de Veerdonk, and W. J. M. de Jonge,
  Physical Review B **50**, 9982 (1994).

- **Current-distribution effects in microstructures for perpendicular magnetoresistance experiments**
  S. K. J. Lenczowski, R. J. M. van de Veerdonk, M. A. M. Gijs, J. B. Giesbers, and H. H. J. M. Janssen,
  Journal of Applied Physics **75**, 5154 (1994).

- **Giant magnetoresistance in polycrystalline $SmMn_2Ge_2$**
  J. H. V. J. Brabers, K. Bakker, H. Nakotte, F. R. de Boer, S. K. J. Lenczowski, and K. H. J. Buschow,
  Journal of Alloys and Compounds **199**, L1 (1993).

- **New contacting technique for thin film resistance measurements perpendicular to the film plane**
  M. A. M. Gijs, J. B. Giesbers, S. K. J. Lenczowski, and H. H. J. M. Janssen,
  Applied Physics Letters **63**, 111 (1993).

- **Perpendicular giant magnetoresistance of microstructured Fe/Cr magnetic multilayers from 4.2 to 300 K**
  M. A. M. Gijs, S. K. J. Lenczowski, and J. B. Giesbers,
  Physical Review Letters **70**, 3343 (1993).

- **Crystal growth and annealing experiments of the high T_c superconductor $Bi_2Sr_2CaCu_2O_{8+\delta}$**
  J. H. P. M. Emmen, S. K. J. Lenczowski, J. H. J. Dalderop, and V. A. M. Brabers,
  Journal of Crystal Growth **118**, 477 (1992).

Conference contributions

- **Giant magnetoresistance of Co/Cu multilayers grown by electrodeposition**: Second international symposium on Metallic Multilayers, Cambridge, September 11-14, 1995.
  S. K. J. Lenczowski, C. Schönenberger, M. A. M. Gijs, and W. J. M. de Jonge,
  Journal of Magnetism and Magnetic Materials, submitted for publication (1995).

- **NMR Study of the structural properties of electrodeposited Co/Cu multilayers**: Second international symposium on Metallic Multilayers, Cambridge, September 11-14, 1995.
  E. A. M. van Alphen, A. H. J. Colaris, S. K. J. Lenczowski, C. Schönenberger, and W. J. M. de Jonge,
  Journal of Magnetism and Magnetic Materials, submitted for publication (1995).

- **Determination of spin-dependent scattering parameters of NiFe/Cu and Co/Cu multilayers**: MRS symposium on Magnetic Ultrathin Films, Multilayers and Surfaces, San Francisco, April 17-21, 1995.
  S. K. J. Lenczowski, M. A. M. Gijs, R. J. M. van de Veerdonk, J. B. Giesbers, and W. J. M. de Jonge,
  Materials Research Society Symposium Proceedings, accepted for publication (1995).

- **Perpendicular giant magnetoresistance using microlithography and substrate patterning techniques (invited paper)**: International workshop on spin-polarized electron transport, Miami, February 19-22, 1995.
M. A. M. Gijs, S. K. J. Lenczowski, J. B. Giesbers, R. J. M. van de Veerdonk, M. T. Johnson, R. M. Jungblut, A. Reinders, and R. M. J. van Gansewinkel, Journal of Magnetism and Magnetic Materials, accepted for publication (1995).

- **Perpendicular giant magnetoresistance of microstructured pillars in Fe/Cr and Co/Cu magnetic multilayers (invited paper)**: 5^{th} NEC symposium on fundamental approaches to new material phases: spin-dependent phenomena in multilayer systems, Karuizawa, October 16-20, 1994.
M. A. M. Gijs, S. K. J. Lenczowski, J. B. Giesbers, R. J. M. van de Veerdonk, M. T. Johnson, and J. B. F. aan de Stegge,
Materials Science and Engineering B **31**, 85 (1995).

- **Giant magnetoresistance in Co/Cu(100) multilayers: interpretation with the quantum model of MR**: 14^{th} international colloquium on Magnetic Films and Surfaces and $\in$-MRS symposium on Magnetic Ultrathin Films, Multilayers and Surfaces, Düsseldorf, August 29-September 2, 1994.
S. K. J. Lenczowski, M. A. M. Gijs, R. J. M. van de Veerdonk, J. B. Giesbers, and W. J. M. de Jonge,
Colloquium Digest, p.21 (1994).

- **Perpendicular giant magnetoresistance of microstructured pillars in magnetic multilayers (invited paper)**: 14^{th} general conference of the European Physical Society, Condensed Matter Division, Madrid, March 28-31, 1994.
M. A. M. Gijs, S. K. J. Lenczowski, J. B. Giesbers, R. J. M. van de Veerdonk, M. T. Johnson, and J. B. F. aan de Stegge,
Physica Scripta **T55**, 189 (1994).

- **Perpendicular giant magnetoresistance of microstructured pillars in Fe/Cr and Co/Cu multilayers (invited paper)**: 38^{th} annual conference on Magnetism and Magnetic Materials, Minneapolis, November 15-18, 1993.
M. A. M. Gijs, J. B. Giesbers, M. T. Johnson, J. B. F. aan de Stegge, H. H. J. M. Janssen, S. K. J. Lenczowski, R. J. M. van de Veerdonk, and W. J. M. de Jonge,
Journal of Applied Physics **75**, 6709 (1994).

- **Perpendicular magnetoresistance of microstructured pillars in Fe/Cr magnetic multilayers (invited paper)**: MRS symposium on Magnetic Ultrathin Films, San Francisco, April 12-16, 1993.
M. A. M. Gijs, S. K. J. Lenczowski, and J. B. Giesbers,
Materials Research Society Symposium Proceedings Vol. **313**, p.11 (1993).

- **Magnetic and transport behavior of AF-coupled layers with a limited number of repetitions**: MRS symposium on Magnetic Ultrathin Films, San Francisco, April 12-16, 1993.
  M. M. H. Willekens, H. J. M. Swagten, A. M. Duif, P. J. H. Bloemen, R. J. T. van Kempen, S. K. J. Lenczowski, and W. J. M. de Jonge,
  Materials Research Society Symposium Proceedings Vol. **313**, p.129 (1993).

- **Perpendicular magnetoresistance of magnetic multilayers, theory and experiment**: First international symposium on Metallic Multilayers, Kyoto, March 1-5, 1993.
  G. E. W. Bauer, M. A. M. Gijs, S. K. J. Lenczowski, and J. B. Giesbers,
  Journal of Magnetism and Magnetic Materials **126**, 454 (1993).

- **Energy distribution of vortex dynamics in $Bi_2Sr_2CaCu_2O_{8+\delta}$ as probed by magnetic susceptibility**: International Conference on Magnetism, Edinburgh, September 2-6, 1991.
  J. H. P. M. Emmen, S. K. J. Lenczowski, V. A. M. Brabers, and W. J. M. de Jonge,
  Journal of Magnetism and Magnetic Materials **104-107**, 473 (1992).

- **Inter- and intragranular properties of $Bi_2CaSr_2Cu_2O_y$ superconductors**: International conference on Materials and Mechanisms of Superconductivity, *High Temperature Superconductors II*, Stanford, July 23-28, 1989.
  J. H. P. M. Emmen, V. A. M. Brabers, C. van der Steen, J. H. J. Dalderop, S. K. J. Lenczowski, and W. J. M. de Jonge,
  Physica C **162-164**, 1613 (1989).

Oral presentations

- **Determination of spin-dependent scattering parameters of NiFe/Cu and Co/Cu multilayers**
  MRS symposium on Magnetic Ultrathin Films, Multilayers and Surfaces, San Francisco, April 1995.

- **Giant magnetoresistance of electrodeposited Co/Cu multilayers**
  Report meeting of the EC science project SmMmS, Laboratoire Central de Recherches, Thomson-CSF, Orsay, February 1995.

- **Interpretation of the giant magnetoresistance (MR) effect in Co/Cu-(100) multilayers with the quantum model of giant MR**
  Midterm evaluation meeting of the EC science project SmMmS, Eindhoven University of Technology, Eindhoven, May 1994.

- **Current-distribution effects in microstructures for perpendicular magnetoresistance measurements**
  Report meeting of the EC science project SmMmS, Institut de Physique et Chimie des Matériaux Strasbourg, Strasbourg, October 1993.

- **Magnetoresistance measurements on Co/Cu multilayers**
  Report meeting of the EC science project SmMmS, Laboratoire de Physique des Solides, Université Paris-Sud, Orsay, July 1993.

About the Author

Staszek Lenczowski was born in Schiedam, The Netherlands, on October 1, 1964. After graduating from high school (Gymnasium β, Dr. Mollercollege, Waalwijk) in 1983, he started his physics study at the Eindhoven University of Technology. His master's thesis, which he finished in 1989, concerned the granular behavior of the high-T_c superconductor Bi-Sr-Ca-Cu-O.

From April 1990 until April 1992 he was attached to the group Cooperative Phenomena of prof. dr. ir. W. J. M. de Jonge by the Institute for Continuing Education of the Eindhoven University of Technology. During this period he did research on the growth of $Bi_2Sr_2CaCu_2O_{8+\delta}$ single crystals by means of a floating-zone technique and the influence of annealing on the superconducting properties. In June 1991 he attended the Thirty-Ninth Scottish Universities Summer School in Physics on high-temperature superconductivity in St.-Andrews, Scotland. Early 1992 he stayed for three months at the Philips Research Laboratories in Eindhoven, where he was introduced to the subject of giant magnetoresistance of magnetic multilayers in the group Experimental and Theoretical Physics of prof. dr. H. van Houten.

In May 1992 he finished his Continuing Education project and continued to work on the giant magnetoresistance effect in magnetic multilayers as a joined member of the scientific staff of the group of prof. dr. ir. W. J. M. de Jonge. This thesis is a result of this work, being part of a cooperative research program of Philips Research Laboratories and the Eindhoven University of Technology. In fact, most of the daily work has been performed in the group of prof. dr. H. van Houten at Philips under the guidance of dr. M. A. M. Gijs.

Acknowledgments

This thesis could not have been realized without the help of many people in many different ways; to all of them I am very grateful. I have greatly enjoyed the very stimulating collaboration between the Eindhoven University of Technology and Philips Research Laboratories, which was made possible by W. J. M. de Jonge and H. van Houten. I am indebted to *all* my colleagues, both at the Eindhoven University of Technology and at Philips Research Laboratories, for many fruitful discussions, help with the measurements, and creating a pleasant working atmosphere. In particular, however, I would like to express my gratitude to M. A. M. Gijs, J. B. Giesbers, R. J. M. van de Veerdonk, and C. Schönenberger, from whose contributions I benefited the most.

Stellingen

behorende bij het proefschrift

"GIANT MAGNETORESISTANCE OF MAGNETIC MULTILAYERS"

van S. K. J. Lenczowski.

1. De in de literatuur gangbare opinie dat multilagen gebaseerd op permalloy gelden als modelsysteem waarvoor de hoge magnetoweerstand wordt veroorzaakt door spinafhankelijke verstrooiing in de bulk van het magnetische materiaal, is twijfelachtig en strookt niet met verschillende experimentele resultaten.

   P. A. Schroeder et al., Mat. Res. Soc. Symp. Proc. Vol. **313**, *47 (1993); Q. Yang et al., Phys. Rev. B* **51**, *3226, (1995); dit proefschrift, paragraaf 4.3.*

2. Het is mogelijk om door middel van geschikte thermische nabehandelingen de supergeleidende overgangstemperatuur van $Bi_2Sr_2CaCu_2O_{8+\delta}$ éénkristallen te verhogen tot 94 K.

3. De magnetoweerstand van gesputterde magnetische multilagen met tussenlaagdiktes die corresponderen met de eerste antiferromagnetische koppelingspiek, kan in belangrijke mate worden beïnvloed door de dikte van de gebruikte bufferlaag.

4. De toevoeging van glansmiddelen aan het elektrolyt heeft een nadelige invloed op de grensvlakstructuur van elektrochemisch gedeponeerde multilagen.

   Dit proefschrift, paragraaf 4.1.

5. Aan het feit dat de aanwezigheid van een *bulk*-Co lijn in een NMR-spectrum van een Co/Cu multilaag met nominale Co laagdiktes die overeenkomen met een mono-atomaire laag impliceert dat het Co juist niet in mono-atomaire lagen maar in clusters aanwezig is, wordt volledig voorbijgegaan door Mushailov *et al.*.

   E. S. Mushailov et al., J. Magn. Magn. Mater. **138**, *207 (1994).*

6. In de door middel van microlithografie verkregen pilaarachtige structuren van Gijs *et al.*, waarmee de magnetoweerstand van metallische multilagen gemeten kan worden met de stroom loodrecht op het vlak van de lagen, dient men voor een correcte interpretatie van de resultaten rekening te houden met de stroomverdeling in deze "pilaren".

   Dit proefschrift, hoofdstuk 5; M. A. M. Gijs et al., Phys. Rev. Lett. **70**, *3343, (1993); Phys. Rev. B* **50**, *16733 (1994).*

7. Bij het mechanisme dat ten grondslag ligt aan het 'collossal' magnetoweerstandeffect in manganaten met een perovskiet kristalstructuur, kan een percolatie-effect voor de elektrische stroom door een mengsel van gebieden met een ferro- en antiferromagnetische fase een belangrijke rol spelen.

8. Voor het toetsen van experimentele magnetoweerstandswaarden aan theoretische berekeningen is het niet voldoende alleen de magnetoweerstand te meten.

9. De magnetoweerstand van een 'spin-valve'-structuur waarin in één van de magnetische lagen een dunne Ru-barrière met een hoge resistiviteit is aangebracht, varieert exponentieel als functie van de afstand van de Ru-barrière tot de niet-magnetische tussenlaag. De karakteristieke lengteschaal van deze exponentiële variatie is weliswaar direct gerelateerd aan de grootste van de vrije-weglengtes van spin-op en spin-neer elektronen, maar niet exact gelijk, zoals Parkin suggereert.

   S. S. P. Parkin, Colloquium Digest van het E-MRS symposium over magnetische, ultradunne films, multilagen en oppervlakken, Düsseldorf, 29 augustus-2 september, p. 27 (1994).

10. Aangezien de Informatie Beheer Groep in sommige gevallen uitgaat van het bruto- i.p.v. netto-inkomen ter bepaling van de hoogte van de studiebeurs, kan de (ex-)student geconfronteerd worden met een lastendruk groter dan 100% van het genoten inkomen.